

# UC Santa Barbara

## UC Santa Barbara Electronic Theses and Dissertations

### Title

Structure-Property Relationships of Organic Electrochemical Transistors Based on the Conjugated Polyelectrolyte PCPDTBTSO<sub>3</sub>- Na (CPE-Na)

### Permalink

<https://escholarship.org/uc/item/8kx6z9fc>

### Author

Lill, Alexander Thomas

### Publication Date

2021

Peer reviewed|Thesis/dissertation

UNIVERSITY OF CALIFORNIA

Santa Barbara

**Structure-Property Relationships of Organic Electrochemical  
Transistors Based on the Conjugated Polyelectrolyte PCPDTBT-  
SO<sub>3</sub>-Na (CPE-Na)**

A Dissertation submitted in partial satisfaction of the requirement for the degree Doctor of  
Philosophy in Chemistry

By

Alexander Thomas Lill

Committee in charge:

Professor Thuc-Quyen Nguyen, Chair

Professor Rachel Segalman

Professor Steve Buratto

Professor Guillermo C. Bazan

September 2021

The dissertation of Alexander Thomas Lill is approved.

---

Guillermo C. Bazan

---

Steven Buratto

---

Rachel Segalman

---

Thuc-Quyen Nguyen, Committee Chair

June 2021

Structure-Property Relationships of Organic Electrochemical Transistors Based on the  
Conjugated Polyelectrolyte PCPDTBT-SO<sub>3</sub>-Na (CPE-Na)

Copyright 2021

by

Alexander Thomas Lill

## ACKNOWLEDGEMENTS

The work outlined in this thesis would not have been possible without the help of a huge number of individuals.

First, I would also like to thank my thesis advisor, Professor Thuc-Quyen Nguyen for her guidance, support and lab resources throughout my PhD. It has been thrilling to work with a research lab that is known internationally for its achievements in organic electronics. I was supported financially by multiple research projects for most of my PhD, and I had access to world class research facilities. I also very much appreciated the opportunity to present my research at the Emerging Material Technologies Summit (EMTS) in Hanoi, Vietnam in front of many of the leaders in the field of organic electronics. Without the guidance from Quyen and the resources she kindly provided, my work would not have been possible.

I would like to thank the sources that funded me throughout my PhD. In the earlier half of graduate school, I was supported by the Mitsubishi Chemical Corporation under the IRP9 project for my work on organic field-effect transistors. I was also supported by the NSF project DMR-1922042 under which I performed all my work on organic electrochemical transistors.

I would also like to thank my committee members, Professor Guillermo Bazan, Professor Steven Buratto and Professor Rachel Segalman. They provided invaluable feedback before and after my candidacy exam, my research and on my publications.

I would also like to thank all the undergraduate student, graduate students, post-doctoral researchers and visiting professors of the Nguyen group. I truly think that the

Nguyen group has the best group of coworkers you could ask for. Discussing our research during lunch was a critical part of solving issues we were having with our research.

I would like to thank my girlfriend, Emily Hardison, who has made my time here in Santa Barbara infinitely better than it could otherwise have possibly been. Our daily walks at the end of the day together with our dog, Mowgli, were great for decompressing and chatting about our day.

Finally, I would like to thank my family for their support throughout my PhD. They are a big reason why I decided to pursue higher education. They made many sacrifices for me to have the opportunity, and for that I am eternally grateful.

# VITA OF ALEXANDER T. LILL

June 2021

## **Education**

---

**University of California, Santa Barbara** **2015-2021**  
PhD Candidate, Department of Chemistry and Biochemistry  
Graduate Advisor: Dr. Thuc-Quyen Nguyen

**University of California, Santa Cruz** **2010-2014**  
BS in Biochemistry and Molecular Biology

## **Research Experience**

---

**University of California, Santa Barbara - Graduate Student Researcher** **August 2015-June 2021**

*Department of Chemistry and Biochemistry, University of California, Santa Barbara*  
*Center for Polymers and Organic Solids (CPOS)*

*Mitsubishi Chemical - Center for Advanced Materials (MC-CAM) (February 2016- April 2018)*

Researcher in the lab of Professor Thuc-Quyen Nguyen. Characterization of mixed ionic-electronic conductors and device physics of organic electrochemical transistors. Data-driven discovery of conjugated polyelectrolytes for neuromorphic computing. Development of high-mobility organic field-effect transistors in collaboration with Mitsubishi Chemical.

**Lam Research Corporation - Process Engineer Intern** **February-July 2015**

*Corporate Technology Development - Fremont, CA*

Deposition and characterization of thin-film metal oxides in a cleanroom environment

**University of California, Santa Cruz - Undergraduate Research Assistant** **April 2013-June 2014**

*Department of Chemistry and Biochemistry, University of California, Santa Cruz*

Undergraduate researcher in the lab of Professor Bakthan Singaram. Organometallic synthesis and methodology

**University of California, Berkeley - Undergraduate Researcher Assistant** **June-September 2013**

*Department of Chemistry, University of California, Berkeley*

Undergraduate researcher in the lab of Professor David Graves. Low-temperature plasma medicine

## **Academic Honors/ Fellowships/ Awards**

---

**Outstanding Service to the Department Award** **2018**

Department of Chemistry and Biochemistry, University of California, Santa Barbara

**Honorable Mention for National Science Foundation Graduate Research Fellowship** **2017**

**Lam Research Corporation Core Values Scholarship** **2015**

**UCSB Summer Research Fellowship** **2015**

Department of Chemistry and Biochemistry, University of California, Santa Barbara

**Teaching/ Student Mentorship**

---

**Teaching Assistant** **2015-2020**  
*Organic Chemistry Lab* (CHEM 6AL, 6BL). University of California, Santa Barbara.

**Mentor to Two Undergraduate Researchers** **2015-2018**

### **Selected Presentations**

---

“Organic Electrochemical Transistors Based on the Conjugated Polyelectrolyte PCPDTBT-SO<sub>3</sub>K (CPE-K)”, Center for Polymers and Organic Solids Annual Presentation, March 26<sup>th</sup>, 2019.

“High-k Fluoropolymer Gate Dielectric in Electrically Stable Organic Field-Effect Transistors”, Emerging Materials and Technologies Summit, Hanoi, Vietnam, November 4<sup>th</sup>, 2018.

“Studies of Ferroelectric Organic Field-Effect Transistors”, Center for Polymers and Organic Solids Annual Presentation”, April 17, 2018.

“Polymer Dielectric Studies for Stable OFET Operation”, MC-CAM Annual Review, April 21, 2017.

“Reactions of Diisopropylaminoborane with Grignard Reagents: A Facile Synthesis of Boronic and Borinic Acids”, 26th Annual Northern California Undergraduate Research Symposium, San Francisco, CA, United States, May 3, 2014.

### **Publications**

---

Luana Llanes, **Alexander T. Lill**, Yangyang Wang, Sangmin Chae, Ahra Yi, Hyo Jung Kim, Lior Sepunaru, Gang Lu, Thuc-Quyen Nguyen, Guillermo C. Bazan. “Side-chain Engineering of Self-doped Conjugated Polyelectrolytes for OECT Fabrication”. *Journal of the American Chemical Society*, Pending Work.

Angelique M. Scheuermann, Hiba Wakidi, **Alexander T. Lill**, Saejin Oh, Luana C. Llanes, Colton A. D’Ambra, Ségolène Antoine, Ming Wang, Michael L. Chabinye, Thuc-Quyen Nguyen, Javier Read de Alaniz, Christopher M. Bates. “Multi-Wavelength Photodetectors Based on an Azobenzene Polymeric Ionic Liquid”. *ACS Applied Materials and Interfaces*, Under Review June 2021.

**Alexander T. Lill**, David X. Cao, Max Schrock, Joachim Vollbrecht, Jianfei Huang, Tung Nguyen-Dang, Viktor V. Brus, Brett Yurash, Dirk Leifert, Guillermo C. Bazan, Thuc-Quyen Nguyen. “Organic Electrochemical Transistors Based on the Conjugated Polyelectrolyte PCPDTBT-SO<sub>3</sub>K (CPE-K)”. *Advanced Materials*, Published July 2020.

**Alexander T. Lill**, Ala’a F. Eftaiha, Jianfei Huang, Hao Yang, Martin Seifrid, Ming Wang, Guillermo C. Bazan, Thuc-Quyen Nguyen. “High-k Fluoropolymer Gate Dielectric in Electrically Stable Organic Field-Effect Transistors”. *ACS Applied Materials and Interfaces*, Published April 2019.

Jianfei Huang, Akchheta Karki, Viktor V. Brus, Yuanyuan Hu, **Alexander T. Lill**, Ming Wang, Guillermo C. Bazan, Thuc-Quyen Nguyen. “Solution-Processed Ion-Free Organic Ratchets with Asymmetric Contacts”. *Advanced Materials*, Published November 2018.

Yuanyuan Hu, David Z. Cao, **Alexander T. Lill**, Lang Jiang, Chong-An Di, Xike Gao, Henning Sirringhaus, Thuc-Quyen Nguyen, “Effect of Alkyl-Chain Length on Charge Transport Properties of Organic Semiconductors and Organic Field-Effect Transistors”. *Advanced Electronic Materials*, Published August 2018.

Yuanyuan Hu, Zachary D. Rengert, Caitlin McDowell, Michael J. Ford, Ming Wang, Akchheta Karki, **Alexander T. Lill**, Guillermo C. Bazan, Thuc-Quyen Nguyen. “Doping Polymer Semiconductors by Organic Salts: Towards High-Performance Solution-Processed Organic Field-Effect Transistors”. *ACS Nano*, Published April 2018.

Hung Phan, Michael J. Ford, **Alexander T. Lill**, Ming Wang, Guillermo C. Bazan, Thuc-Quyen Nguyen. “Electrical Double-Slope Nonideality in Organic Field-Effect Transistors”. *Advanced Functional Materials*, Published February 2018.

Hung Phan, Michael J. Ford, **Alexander T. Lill**, Ming Wang, Guillermo C. Bazan, Thuc-Quyen Nguyen. “Improving Electrical Stability and Ideality in Organic Field-Effect Transistors by the Addition of Fullerenes: Understanding the Working Mechanism”. *Advanced Functional Materials*, Published August 2017.

Ming Wang, Michael J. Ford, **Alexander T. Lill**, Hung Phan, Thuc-Quyen Nguyen, Guillermo C. Bazan. “Hole Mobility and Electron Injection Properties of D-A Conjugated Copolymers with Fluorinated Phenylene Acceptor Units”. *Advanced Materials*, Published January 2017.

Christopher L. Bailey, Jacob W. Clary, Chittreya Tansakul, Lucas Klabunde, Christopher L. Anderson, Alexander Y. Joh, **Alexander T. Lill**, Rebecca Braslau, Bakthan Singaram. “Reduction of Weinreb Amides to Aldehydes under Ambient Conditions with Magnesium Borohydride Reagents”. *Tetrahedron Letters*, Published January 2015.

## ABSTRACT

### Structure-Property Relationships of Organic Electrochemical Transistors Based on the Conjugated Polyelectrolyte PCPDTBT-SO<sub>3</sub>-Na (CPE-Na)

by

Alexander Thomas Lill

This dissertation is concerned with the fabrication and characterization of organic electrochemical transistors (OECTs) made from polyelectrolytes based on the material PCPDTBT-SO<sub>3</sub>-Na (CPE-Na). OECTs are electrolyte-gated transistors that allow the electrolyte to permeate into the bulk of the film and directly changes the doping state of the bulk of the semiconducting layer. The relationship between the molecular structure of the polyelectrolytes and the material properties are explored in the lens of optimizing device characteristics in OECTs. The first chapter of this thesis focuses on the development of OECTs made using PCPDTBT-SO<sub>3</sub>-K (CPE-K) as the active layer. While the large majority of OECT research still utilizes poly(3,4-ethylenedioxythiophene) polystyrene sulfonate (PEDOT:PSS) as the active layer, a few new OECT materials have been recently reported. CPE-K has been used in the past for applications such as DNA-detection, thermoelectric devices and as interlayers in organic photovoltaic devices. Conjugated polyelectrolytes (CPEs) represent a promising and unique class of materials which are characterized by their conjugated carbon backbone and pendant ionic chains. Their water solubility in addition to their electronic and ionic conductivity makes them an ideal candidate for OECT applications. Using various spectroscopic and electric characterization techniques, CPE-K was fully characterized so that

it could be accurately compared to other OECT materials reported in the literature. In fact, CPE-K is among the short list of high-performance OECT materials. The techniques used in this work was used to shed light on the operational mechanism of CPE-based OECTs. In addition, the effective use of interdigitated contacts was used to increase the transconductance of OECT devices.

The second portion of this thesis expands on the work of CPE OECTs, by exploring their structure-property-relationship. A series of CPE-Na polymers with varying sidechain lengths were synthesized by collaborator Luana Llanes from the lab of Professor Guillermo Bazan. A series of CPE-Na with increasing alkyl chain distances (2-5 methylene units) were synthesized. The purpose of synthesizing these materials was to explore the effect of varying the distance of the pendant charged sulfonate on the side-chain. CPE-Na is a self-doped polymer, due to the negative charge on the sulfonate stabilizing the positively charged polaron. It was hypothesized that reducing the side-chain length would result in easier doping of the CPE due to the proximity of the sulfonate. To our surprise, the opposite trend was observed. By using a wide range of characterization techniques, the structure-property-relationship between the sidechain length and ease of doping of the CPE backbone was explored.

The next chapter of the thesis switches topics to organic field-effect transistors (OFETs). Due to convenience and low leakage current, many OFETs use silicon dioxide as the gate dielectric material. As demonstrated by Dr. Hung Phan, trap sites at the dielectric-semiconductor interface result charge trapping. This charge trapping results in unwanted artifacts such as hysteresis, double-slope nonideality characteristics, and reduction in current when the device is continuously biased. The fluoropolymer P(VDF-HFP) was used as a dielectric material. We found that the device transfer characteristics are heavily dependent on

the processing conditions and choosing the proper grade of P(VDF-HFP). We presented the correct choice of processing conditions and material grade results in ideal transfer characteristics such as high on-off ratio, low threshold voltage, low hysteresis and high current stability.

The final section of the thesis discusses a project to explore the structure-property relationship of a group of 12 different n-type non-fullerene acceptor small molecules. Non-fullerene acceptors (NFAs) have recently become an area of interest to researchers aiming to develop high performance organic solar cells due to their promising electronic properties and greater tunability relative to fullerene-based acceptors. Despite the success of NFAs in organic solar cells, there have only been a few studies looking at the electron mobility of these materials. A collection of 12 NFAs with a variety of core groups and sidechain configurations were tested as the active layer in an organic field-effect transistor (OFET) to measure the mobility of horizontal charge transport.

## Table of Contents

<b>Chapter 1. Introduction.....</b>	<b>1</b>
1.1 Organic Semiconductors.....	1
1.2 Conjugated Polyelectrolytes.....	2
1.3 Organic Field-Effect Transistors.....	3
1.4 Organic Electrochemical Transistors.....	5
1.5 References.....	9
<b>Chapter 2. Experimental Techniques.....</b>	<b>18</b>
2.1 Overview.....	18
2.2 Preparation of Solutions and Thin Films.....	19
2.3 Contact Angle Measurements.....	22
2.4 UV-Vis Spectroscopy.....	24
2.5 Ultraviolet and X-ray Photoelectron Spectroscopies (UPS & XPS).....	25
2.6 Atomic Force Microscopy.....	25
2.7 Grazing Incidence Wide-Angle X-Ray Spectroscopy.....	26
2.8 Organic Field-Effect Transistors and Organic Electrochemical Transistor Fabrication.....	28
2.9 Impedance Spectroscopy.....	30
2.10 Organic Transistor Electrical Characterization.....	32
2.11 References.....	33
<b>Chapter 3. Organic Electrochemical Transistors Based on the Conjugated Polyelectrolyte PCPDTBT-SO<sub>3</sub>K (CPE-K).....</b>	<b>35</b>
3.1 Introduction.....	35
3.2 Operational Mechanism of Organic Electrochemical Transistors.....	36
3.3 Conjugated Polyelectrolytes, Their Applications, and the Research Motivation..	37
3.4 Stabilization of CPE-K Films with (3-glycidyloxypropyl)trimethoxysilane (GOPS).....	38
3.5 Transfer Characteristics and Transient Behavior of CPE-K OEECTs.....	43
3.6 Volumetric Capacitance Measurements and Transconductance vs Film Thickness.....	48
3.7 Operational Mechanism of CPE-K OEECTs.....	54
1.7.1 Effect on Salt Concentration and Type on Transfer Characteristics.....	54
1.7.2 Spectroelectrochemical Measurements.....	55
3.8 Conclusions.....	58
3.9 Experimental Methods.....	59
3.10 References.....	61
<b>Chapter 4. Side-chain Engineering of Self-doped Conjugated Polyelectrolytes for OEECT Fabrication.....</b>	<b>66</b>
4.1 Introduction and Motivation.....	66

4.2 Organic Electrochemical Transistor (OECT) Characterization.....	66
4.3 Electrochemical Impedance Spectroscopy Measurements.....	74
4.3.1 Volumetric Capacitance.....	74
4.3.2 Ion Conductivity.....	74
4.4 Exploring Polaron Formation.....	75
4.4.1 Ultraviolet-visible-near-infrared spectroscopy (UV-Vis-NIR).....	75
4.4.2 Ultraviolet-photoelectron spectroscopy (UPS).....	76
4.5 Grazing Incidence Wide Angle X-Ray Spectroscopy of CPE's.....	78
4.6 Experimental Methods.....	81
4.7 Conclusions.....	84
4.8 References.....	85
<b>Chapter 5. High-k Fluoropolymer Gate Dielectric in Electrically Stable Organic Field-Effect Transistors.....</b>	<b>91</b>
5.1 Introduction and Motivation.....	91
5.2 P(VDF-HFP) As a Passivation Layer for Organic Field-Effect Transistors.....	94
5.3 Conditions That Dictate Performance in P(VDF-HFP) OFETs.....	97
5.4 Exploring the Effect of HFP Monomer Content on Charge Transport.....	106
5.5 Conclusions.....	113
5.6 Experimental Methods.....	115
5.7 References.....	117
<b>Chapter 6. Charge Transport Studies of Non-Fullerene Acceptors and High-mobility Semi-conducting Polymers in Organic Field-Effect Transistors.....</b>	<b>123</b>
6.1 Introduction and Motivation.....	123
6.2 Non-Fullerene Acceptor N-Type Organic Field-Effect Transistors.....	123
6.3 Temperature Dependent Charge Transport in Polymer Organic Field-Effect Transistors.....	128
6.4 References.....	134
<b>Chapter 7. Summary and Outlook.....</b>	<b>136</b>

# Chapter 1:

## Introduction

### 1.1 Organic Semiconductors

Organic semiconductors are carbon-based molecules and polymers that are unified by their high levels of conjugation. Overlapping  $sp^2$  orbitals form  $\pi$ -bonds that, when conjugated, form delocalized electronic states that provide semiconducting properties. Ever since their discovery, synthetic chemists have attempted to change the electrical and physical properties of organic semiconductors. Organic semiconductors are inherently planar and rigid, making them difficult to dissolve. However, by introducing solubilizing sidechains to the conjugated “backbone”, organic semiconductors can be solution processed. Solution processing has opened up the possibility of printing electronic circuits and coating entire surfaces under ambient, room temperature conditions.

Organic semiconductors exhibit many of the electronic properties of traditional inorganic semiconductors, however their solution processability open up the possibility for low cost printing processes. Due to the weak Van der Waals between neighboring molecules, organic electronic materials are much more flexible than their inorganic counterparts. This has been utilized by research teams to fabricate highly conformable devices for bioelectronic applications. Organic semiconductors have also been used to fabricate solar cells<sup>1</sup>, photodetectors<sup>2</sup>, light emitting diodes (LEDs)<sup>3</sup> and transistors<sup>4</sup>. The ability to change the chemical structure of organic semiconductors, and thus the electrical performance, is another advantage of organic semiconductors. For each application, the chemical structure of organic

semiconducting materials has been tuned to maximize their performance. The possibilities of chemical structures to explore are virtually limitless, and scientists are continuously making improvements on past molecules and learning more about the relationship between structure and their properties. In this thesis, I will focus primarily on materials that have been optimized over many years for applications in transistors. However, before I am able to move on to this topic I will discuss conjugated polyelectrolytes, a special class of organic materials.

## **1.2 Conjugated Polyelectrolytes**

Conjugated polyelectrolytes (CPE's) contain the conjugated "backbone" of organic semiconductors and pendant ionic sidechains that make them soluble in polar solvents. CPEs have been used in sensing of small ions as well as large biomolecules, proteins, and DNA.<sup>5-33</sup> CPEs have also been used as hole and electron interlayers in organic light emitting diodes (OLEDs), organic photovoltaics (OPVs), and in organic field-effect transistors (OFETs) to assist in charge injection from the electrodes into the active layer.<sup>34-49</sup> CPEs have also been used as the active layer itself in OLEDs, light emitting electrochemical cells (PLEECs) and dye sensitized solar cells (DSSCs).<sup>50-70</sup> In this thesis, I will discuss the use of organic semiconducting polymer in organic field-effect transistors and conjugated polyelectrolytes in organic electrochemical transistors.

### 1.3 Organic Field-Effect Transistors

Organic Field-Effect Transistors (OFETs) are one of the fundamental organic semiconductor devices, whose purpose is to regulate and amplify electronic current. **Figure 1.1** shows the basic device architecture of an OFET. The device consists of three metal terminals: a source, a drain and a gate. The source and drain electrodes are separated by a thin organic semiconducting layer. Between the organic semiconducting layer and the gate electrode there is an electrically insulating dielectric layer. Electric charges are injected from the source electrode, however, little to no current flows to the drain electrode until a voltage is applied between the gate and drain electrodes. In the case of hole transporting organic semiconductors, a negative gate voltage induces the injection of holes to the interface between the semiconductor and the dielectric layer.

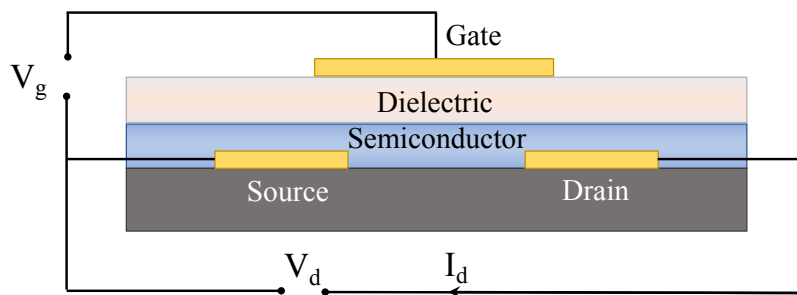


**Figure 1.1:** Device architecture of an organic field-effect transistor

The main figure of merit of organic semiconductors in OFETs is mobility ( $\text{cm}^2 \text{V}^{-1} \text{s}^{-1}$ ), which quantifies how easily an electronic charge is able to transport through the material under an applied voltage. Mobility can be determined by plotting the current between the source and drain contacts while sweeping the gate voltage under a constant source-drain bias.

This type of measurement is called a transfer curve, and is shown in **Figure 1.2** (blue trace). The square root of the current is directly proportional to the gate voltage (red trace). By taking device geometries in to account, mobility can be calculated using the following equation:

$$I_{ds,sat} = \frac{W}{2L} \mu C_i (V_g - V_{th})^2 \quad \text{Equation 2.1}$$

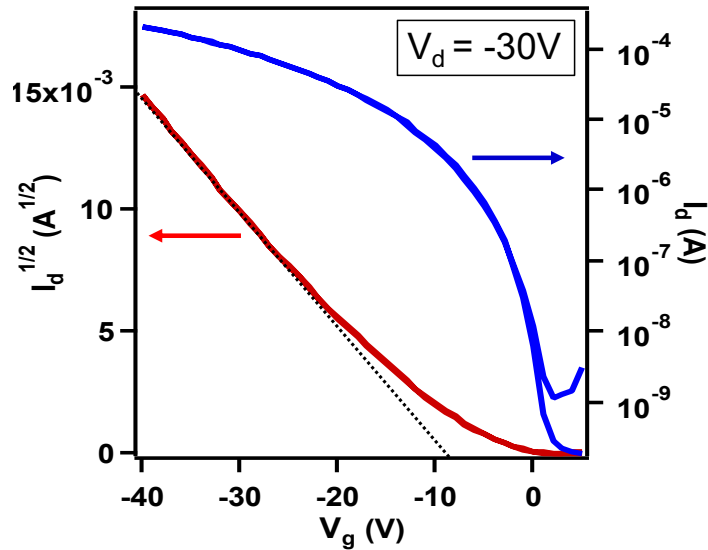


**Figure 1.2:** Example of a transfer curve of an organic field-effect transistor. The gate voltage is swept from 5V to -40V while a constant bias of -30V is held between the source and drain electrodes (blue trace). The red trace shows the square root of the current versus gate voltage. By finding the slope of this curve, mobility can be calculated.

By extrapolating the line of the slope of the square root of the current versus the gate voltage to the x-axis, we are able to calculate the threshold voltage. The voltage is swept in both directions to measure the hysteresis, where ideal transistors show no difference between the forward and backward scan.

## 1.4 Organic Electrochemical Transistors

Only a few nanometers of semiconductor are doped at the interface between the dielectric and semiconductor during operation. In the case of organic electrochemical transistors, the entire bulk of the channel becomes doped and conductive. Organic electrochemical transistors (OECTs) are transducers of biochemical signals into electronic signals, and have obtained a growing amount of interest in recent years.<sup>71-73</sup> OECTs have significant potential applications for human health, such as miniaturized biosensors for cancer diagnosis, pH-sensing, and in vivo neural recording and modulation.<sup>74-77</sup> Organic electronic materials are inherently well suited for such bioelectronic applications due to their structure. Organic electronic small molecules and polymers consist of molecular building blocks which are held together with weak van der Waals interactions. This leads to soft mechanical properties that allow for the fabrication of flexible and even conformable electronic devices that are desirable in health applications. Another advantage of the weak van der Waals interactions between organic molecules is the efficient transport of ions within the solid material. Ion transport is a critical component of high performance bioelectronic devices, yet is not efficient in crystalline covalent networks such as silicon. **Figure 1.3** shows the structure of a typical OECT, which contains two metal contacts separated by a channel of an organic electronic material. An electrolyte solution is placed on top of the channel and an Ag/AgCl electrode is immersed in the solution to serve as an electrochemical gate. In an OECT device, electrochemical potentials can drive ions into or out of the organic semiconducting layer, leading to a change in the doping state of the organic material. The change in the doping state of the organic electronic material results in a change in conductivity which can be recorded. In

practical applications, the cellular or bodily fluid represents the electrolyte, where changes in ion flux from physiochemical processes alter the gate potential, and thereby the measured current. The most common organic material used in OECTs is a highly doped conjugated polymer named PEDOT:PSS (**Figure 1.4a**). When OECTs are operating, a positive gate bias ( $V_g$ ) drives positive ions in the electrolyte to penetrate into the PEDOT:PSS layer to compensate the  $\text{SO}_3^-$  groups of PSS, hence reduce hole density in PEDOT (saturation-mode). In contrast, semiconducting organic materials such as CPE-K, operate by increasing their conductivity as a gate voltage is applied and ions penetrate into the film (depletion-mode) (**Figure 1.4b**).

OECTs are extraordinarily sensitive because ions penetrate directly into the conduction layer. Organic field effect transistors, an area of research interest to the Nguyen group<sup>78-84</sup>, modulate current by accumulating charges at either side of a gate dielectric in a 2-D sheet and is described by parallel plate capacitance.<sup>85</sup> In comparison, OECTs current-voltage relationship is described by volumetric capacitance, which can be orders of magnitude larger (**Figure 1.5**).<sup>2</sup> This results in transistors that operate in truly low voltage ranges within hundreds of millivolts, which allows them to be highly sensitive to small signals. A key parameter used to benchmark the performance of OECTs is called the transconductance ( $g_m$ ), which is defined as the rate of the change in measured current versus the change in applied voltage. Since  $g_m$  depends on physical dimensions of the device, it can be expressed as

$$g_m = \frac{W}{L} \mu C^* (V_{th} - V_g)$$

where  $W$  and  $L$  are the width and length of the channel, respectively,  $\mu$  is electronic carrier mobility,  $C^*$  is capacitance per unit area,  $V_{th}$  is threshold voltage and  $V_g$  is gate voltage. **Figure 1.4** shows plots of measured current versus gate voltage of OECTs fabricated using PEDOT:PSS and CPE-K (red trace, solid circles). The transconductance of the device was calculated using the slope of the current trace (blue trace, open circles). OECTs require both high ionic conduction for ions to diffuse in and out of the material when doping and de-doping the active layer, and high transconductance in the doped state to quantitatively measure differences in current in both the “on” and “off” state of the device.<sup>78</sup> There are a few reports on OECTs using CPEs as an active layer however, the transconductance is much lower than that of PEDOT:PSS.<sup>87–89</sup> We have demonstrated that with proper control of electronic conduction, it is possible to achieve high transconductance in OECTs using CPEs as an active layer. In short, for those devices that require both ionic and electronic transport, progress towards making these devices a commercial reality is currently slow due to a lack of fundamental understanding of the underlying chemical structures that govern ionic and electronic transport. Materials used in OECTs need to be carefully designed to control parameters such as charge mobility, ion mobility, capacitance, flexibility, biocompatibility, and stability.<sup>90–94</sup>

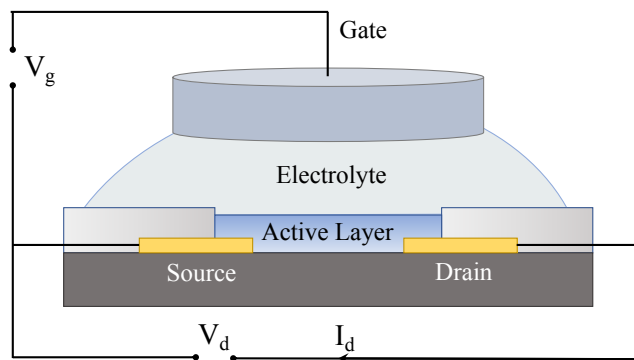


**Figure 1.3:** Device architecture of an organic electrochemical transistor

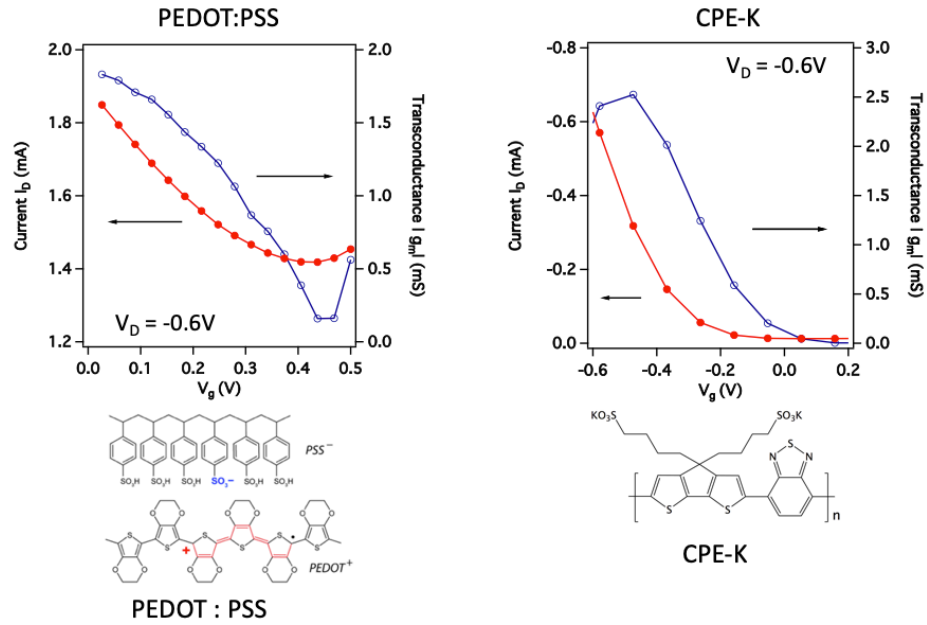


**Figure 1.4:** (a) Structure of PEDOT:PSS and transfer curve showing current versus gate voltage and transconductance versus gate voltage. (b) Structure of CPE-K and transfer curve showing current versus gate voltage and transconductance versus gate voltage.

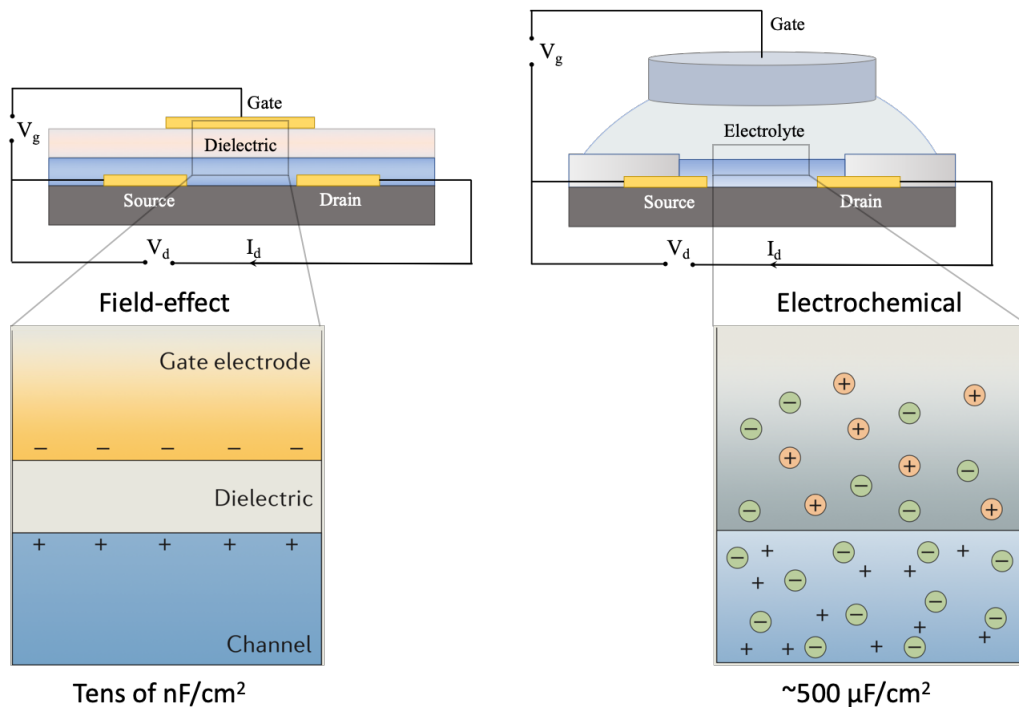


**Figure 1.5:** Difference in operation between organic field-effect transistors and organic electrochemical transistors.

## 1.5 References

1. Zhou, H.; Zhang, Y.; Mai, C.-K.; Collins, S. D.; Bazan, G. C.; Nguyen, T.-Q.; Heeger, A. J. Polymer Homo-Tandem Solar Cells with Best Efficiency of 11.3%. *Advanced Materials* **2015**, *27* (10), 1767–1773.
2. Huang, J.; Lee, J.; Schrock, M.; Dixon, A. L.; Lill, A. T.; Cho, K.; Bazan, G. C.; Nguyen, T.-Q. Large-Gain Low-Voltage and Wideband Organic Photodetectors via Unbalanced Charge Transport. *Mater. Horiz.* **2020**.
3. Tanase, C.; Meijer, E. J.; Blom, P. W. M.; de Leeuw, D. M. Unification of the Hole Transport in Polymeric Field-Effect Transistors and Light-Emitting Diodes. *Phys. Rev. Lett.* **2003**, *91* (21), 216601.
4. Lill, A. T.; Eftaiha, A. F.; Huang, J.; Yang, H.; Seifrid, M.; Wang, M.; Bazan, G.C.; Nguyen, T.-Q. High-k Fluoropolymer Gate Dielectric in Electrically Stable Organic Field-Effect Transistors. *ACS Appl. Mater. Interfaces* **2019**.
5. Lee, K., Povlich, L. K. & Kim, J. Label-free and self-signal amplifying molecular DNA sensors based on bioconjugated polyelectrolytes. *Adv. Funct. Mater.* **17**, 2580–2587 (2007).
6. Kushon, S. A. *et al.* Detection of single nucleotide mismatches via fluorescent polymer superquenching. *Langmuir* **19**, 6456–6464 (2003).
7. Rininsland, F. *et al.* Metal ion-mediated polymer superquenching for highly sensitive detection of kinase and phosphatase activities. *Proc. Natl. Acad. Sci. U. S. A.* **101**, 15295–15300 (2004).
8. Fan, H., Zhang, T., Lv, S. & Jin, Q. Fluorescence turn-on assay for glutathione reductase activity based on a conjugated polyelectrolyte with multiple carboxylate groups. *J. Mater. Chem.* **20**, 10901–10907 (2010).
9. An, L., Liu, L. & Wang, S. Label-free, homogeneous, and fluorescence ‘turn-on’ detection of protease using conjugated polyelectrolytes. *Biomacromolecules* **10**, 454–457 (2009).
10. Liu, Y. & Schanze, K. S. ANYL 12-A conjugated polyelectrolyte based real-time fluorescence assay for alkaline phosphatase with pyrophosphate as substrate. *Abstr. Pap. Am. Chem. Soc.* **236**, 8605–8612 (2008).

11. Pinto, M. R. & Schanze, K. S. Amplified fluorescence sensing of protease activity with conjugated polyelectrolytes. *Proc. Natl. Acad. Sci. U. S. A.* **101**, 7505–10 (2004).
12. Liu, Y., Ogawa, K. & Schanze, K. S. Conjugated polyelectrolytes as fluorescent sensors. *J. Photochem. Photobiol. C Photochem. Rev.* **10**, 173–190 (2009).
13. Li, K. & Liu, B. Water-soluble conjugated polymers as the platform for protein sensors. *Polym. Chem.* **1**, 252–259 (2010).
14. Feng, F., Liu, L., Yang, Q. & Wang, S. Water-soluble conjugated polymers for fluorescent-enzyme assays. *Macromol. Rapid Commun.* **31**, 1405–1421 (2010).
15. Jiang, H., Zhao, X. & Schanze, K. S. Effects of polymer aggregation and quencher size on amplified fluorescence quenching of conjugated polyelectrolytes. *Langmuir* **23**, 9481–9486 (2007).
16. DiCesare, N., Pinto, M. R., Schanze, K. S. & Lakowicz, J. R. Saccharide detection based on the amplified fluorescence quenching of a water-soluble poly(phenylene ethynylene) by a boronic acid functionalized benzyl viologen derivative. *Langmuir* **18**, 7785–7787 (2002).
17. Yang, C. J., Pinto, M., Schanze, K. & Tan, W. Direct synthesis of an oligonucleotide-poly-(phenylene ethynylene) conjugate with a precise one-to-one molecular ratio. *Angew. Chemie - Int. Ed.* **44**, 2572–2576 (2005).
18. Zhao, X., Liu, Y. & Schanze, K. S. A conjugated polyelectrolyte-based fluorescence sensor for pyrophosphate. *Chem. Commun.* **1**, 2914–2916 (2007).
19. Tang, Y. *et al.* Radical Scavenging Mediating Reversible Fluorescence Quenching of an Anionic Conjugated Polymer : Highly Sensitive Probe for Antioxidants. *Chem. Mater.* **18**, 3605–3610 (2006).
20. He, F. *et al.* Fluorescence-amplifying detection of hydrogen peroxide with cationic conjugated polymers, and its application to glucose sensing. *Adv. Funct. Mater.* **16**, 91–94 (2006).
21. Li, C., Numata, M., Takeuchi, M. & Shinkai, S. A sensitive colorimetric and fluorescent probe based on a polythiophene derivative for the detection of ATP. *Angew. Chemie - Int. Ed.* **44**, 6371–6374 (2005).

22. Saikia, G. & Iyer, P. K. A remarkable superquenching and superdequenching sensor for the selective and noninvasive detection of inorganic phosphates in saliva. *Macromolecules* **44**, 3753–3758 (2011).
23. Li, H., Yang, R. & Bazan, G. C. Fluorescence energy transfer to dye-labeled DNA from a conjugated polyelectrolyte prequenched with a water-soluble C60derivative. *Macromolecules* **41**, 1531–1536 (2008).
24. Kim, I. B., Dunkhorst, A., Gilbert, J. & Bunz, U. H. F. Sensing of lead ions by a carboxylate-substituted PPE: Multivalency effects. *Macromolecules* **38**, 4560–4562 (2005).
25. Harrison, B. S., Ramey, M. B., Reynolds, J. R. & Schanze, K. S. Amplified fluorescence quenching in a poly(p-phenylene)-based cationic polyelectrolyte [2]. *J. Am. Chem. Soc.* **122**, 8561–8562 (2000).
26. Chen, L. *et al.* Highly sensitive biological and chemical sensors based on reversible fluorescence quenching in a conjugated polymer. *Proc. Natl. Acad. Sci. U. S. A.* **96**, 12287–12292 (1999).
27. Li, B., Qin, C., Li, T., Wang, L. & Dong, S. Fluorescent switch constructed based on hemin-sensitive anionic conjugated polymer and its applications in DNA-related sensors. *Anal. Chem.* **81**, 3544–3550 (2009).
28. Kushon, S. A. *et al.* Detection of DNA hybridization via fluorescent polymer superquenching. *Langmuir* **18**, 7245–7249 (2002).
29. Liu, Y., Ogawa, K. & Schanze, K. S. Conjugated polyelectrolyte based real-time fluorescence assay for phospholipase C. *Anal. Chem.* **80**, 150–158 (2008).
30. Liu, Y. & Schanze, K. S. Conjugated Polyelectrolyte Based Real-Time Fluorescence Assay for Adenylate Kinase. *Anal. Chem.* **81**, 231–239 (2009).
31. Wang, Y., Zhang, Y. & Liu, B. Conjugated Polyelectrolyte Based Fluorescence Turn-On Assay for Real-Time Monitoring of Protease Activity. *Anal. Chem.* **82**, 8604–8610 (2010).
32. Chemburu, S. *et al.* Conjugated polyelectrolyte supported bead based assays for phospholipase A2 activity. *J. Phys. Chem. B* **112**, 14492–14499 (2008).

33. Kumaraswamy, S. *et al.* Fluorescent-conjugated polymer superquenching facilitates highly sensitive detection of proteases. *Proc. Natl. Acad. Sci. U. S. A.* **101**, 7511–5 (2004).
34. Jin, Y., Bazan, G. C., Heeger, A. J., Kim, J. Y. & Lee, K. Improved electron injection in polymer light-emitting diodes using anionic conjugated polyelectrolyte. *Appl. Phys. Lett.* **93**, 8–11 (2008).
35. Jo, G. *et al.* Tuning of a graphene-electrode work function to enhance the efficiency of organic bulk heterojunction photovoltaic cells with an inverted structure. *Appl. Phys. Lett.* **97**, (2010).
36. Huang, F. *et al.* Synthesis, photophysics, and electroluminescence of high-efficiency saturated red light-emitting polyfluorene-based polyelectrolytes and their neutral precursors. *J. Mater. Chem.* **15**, 2499–2507 (2005).
37. Matsumura, S. *et al.* Ionomers for proton exchange membrane fuel cells with sulfonic acid groups on the end-groups: Novel branched poly(ether-ketone)s. *Am. Chem. Soc. Polym. Prepr. Div. Polym. Chem.* **49**, 511–512 (2008).
38. Wang, H. *et al.* A water-soluble pi-conjugated polymer with up to 100 mg.mL(-1) solubility. *Macromol. Rapid Commun.* **28**, 1645–1650 (2007).
39. Ma, W. *et al.* Water/methanol-soluble conjugated copolymer as an electron-transport layer in polymer light-emitting diodes. *Adv. Mater.* **17**, 274–277 (2005).
40. Luo, J. *et al.* Enhanced open-circuit voltage in polymer solar cells. *Appl. Phys. Lett.* **95**, 0–3 (2009).
41. Seo, J. H. *et al.* Improved injection in n-type organic transistors with conjugated polyelectrolytes. *J. Am. Chem. Soc.* **131**, 18220–18221 (2009).
42. Na, S. I. *et al.* Enhanced performance of inverted polymer solar cells with cathode interfacial tuning via water-soluble polyfluorenes. *Appl. Phys. Lett.* **97**, 2008–2011 (2010).
43. Choi, H. *et al.* Combination of titanium oxide and a conjugated polyelectrolyte for high-performance inverted-type organic optoelectronic devices. *Adv. Mater.* **23**, 2759–2763 (2011).
44. Seo, J. H. *et al.* Improved high-efficiency organic solar cells via incorporation of a conjugated polyelectrolyte interlayer. *J. Am. Chem. Soc.* **133**, 8416–8419 (2011).

45. Po, R., Carbonera, C., Bernardi, A. & Camaioni, N. The role of buffer layers in polymer solar cells. *Energy Environ. Sci.* **4**, 285–310 (2011).
46. Chen, L.-M., Xu, Z., Hong, Z. & Yang, Y. Interface investigation and engineering – achieving high performance polymer photovoltaic devices. *J. Mater. Chem.* **20**, 2575 (2010).
47. Xu, Y. *et al.* Solvent effects on the architecture and performance of polymer white-light-emitting diodes with conjugated oligoelectrolyte electron-transport layers. *Adv. Mater.* **21**, 584–588 (2009).
48. Garcia, A. *et al.* Controlling ion motion in polymer light-emitting diodes containing conjugated polyelectrolyte electron injection layers. *J. Am. Chem. Soc.* **133**, 2492–2498 (2011).
49. Hoven, C. *et al.* Ion motion in conjugated polyelectrolyte electron transporting layers. *J. Am. Chem. Soc.* **129**, 10976–10977 (2007).
50. Zhang, W., Fang, Z., Su, M., Saeys, M. & Liu, B. A triphenylamine-based conjugated polymer with donor-acceptor architecture as organic sensitizer for dye-sensitized solar cells. *Macromol. Rapid Commun.* **30**, 1533–1537 (2009).
51. Liu, X., Zhu, R., Zhang, Y., Liu, B. & Ramakrishna, S. Anionic benzothiadiazole containing polyfluorene and oligofluorene as organic sensitizers for dye-sensitized solar cells. *Chem. Commun.* 3789–3791 (2008).
52. Edman, L. *et al.* Single-component light-emitting electrochemical cell with improved stability. *Appl. Phys. Lett.* **82**, 3961–3963 (2003).
53. Wu, H. *et al.* Efficient electron injection from a bilayer cathode consisting of aluminum and alcohol-/water-soluble conjugated polymers. *Adv. Mater.* **16**, 1826–1830 (2004).
54. Zhang, Y. *et al.* Phosphorescent chelating polyelectrolytes and their neutral precursors: Synthesis, characterizations, photoluminescence and electroluminescence. *Polymer (Guildf)*. **48**, 3468–3476 (2007).
55. Shi, W. *et al.* Triphenylamine and fluorene based cationic conjugated poly electrolytes: Synthesis and characterization. *Macromol. Chem. Phys.* **210**, 150–160 (2009).

56. Zhang, Y. *et al.* Synthesis and optoelectronic characterization of conjugated phosphorescent polyelectrolytes with a neutral Ir complex incorporated into the polymer backbone and their neutral precursors. *J. Mater. Chem.* **17**, 992–1001 (2007).
57. Hou, L. *et al.* Polymer light-emitting diodes with novel environment-friendly alcohol-soluble conjugated copolymer. *Thin Solid Films* **515**, 2632–2634 (2006).
58. Huang, F., Wu, H., Wang, D., Yang, W. & Cao, Y. Novel Electroluminescent Conjugated Polyelectrolytes Based on Polyfluorene. *Chem. Mater.* **16**, 708–716 (2004).
59. Thünemann, A. F. & Ruppelt, D. Electroluminescent polyelectrolyte-surfactant complexes. *Langmuir* **17**, 5098–5102 (2001).
60. Liu, B., Yu, W. L., Lai, Y. H. & Huang, W. Synthesis of a novel cationic water-soluble efficient blue photoluminescent conjugated polymer. *Chem. Commun.* 551–552 (2000).
61. Ramakrishna, G. & Ghosh, H. N. Efficient electron injection from twisted intramolecular charge transfer (TICT) state of 7-diethyl amino coumarin 3-carboxylic acid (D-1421) dye to TiO<sub>2</sub>nanoparticle. *J. Phys. Chem. A* **106**, 2545–2553 (2002).
62. Cimrová, V. *et al.* Efficient blue light emitting devices based on rigid-rod polyelectrolytes. *Adv. Mater.* **8**, 585–588 (1996).
63. Taranekar, P. *et al.* Hyperbranched conjugated polyelectrolyte bilayers for solar-cell applications. *J. Am. Chem. Soc.* **129**, 8958–8959 (2007).
64. Mwaura, J. K., Zhao, X., Jiang, H., Schanze, K. S. & Reynolds, J. R. Spectral broadening in nanocrystalline TiO<sub>2</sub>solar cells based on poly(p-phenylene ethynylene) and polythiophene sensitizers. *Chem. Mater.* **18**, 6109–6111 (2006).
65. Hoven, C. V. *et al.* Chemically fixed p-n heterojunctions for polymer electronics by means of covalent B-F bondformation. *Nat. Mater.* **9**, 249–252 (2010).
66. Gao, J., Li, Y., Yu, G. & Heeger, A. J. Polymer light-emitting electrochemical cells with frozen junctions. *J. Appl. Phys.* **86**, 4594–4599 (1999).
67. Gao, J., Yu, G. & Heeger, A. J. Polymer light-emitting electrochemical cells with frozen p-i-n junction. *Appl. Phys. Lett.* **71**, 1293–1295 (1997).

68. Gu, Z., Bao, Y. J., Zhang, Y., Wang, M. & Shen, Q. D. Anionic water-soluble poly(phenylenevinylene) alternating copolymer: High-efficiency photoluminescence and dual electroluminescence. *Macromolecules* **39**, 3125–3131 (2006).
69. Edman, L. *et al.* Single-component light-emitting electrochemical cell fabricated from cationic polyfluorene: Effect of film morphology on device performance. *J. Appl. Phys.* **98**, (2005).
70. Thünemann, A. F. Nanostructured dihexadecyldimethyl-ammonium-poly(1,4-phenylene-ethynylene-carboxylate): An ionic complex with blue electroluminescence. *Adv. Mater.* **11**, 127–130 (1999).
71. Berggren, M.; Richter-Dahlfors, A. Organic Bioelectronics. *Advanced Materials* **2007**, *19* (20), 3201–3213.
72. Rivnay, J.; Owens, R. M.; Malliaras, G. G. The Rise of Organic Bioelectronics. *Chem. Mater.* **2014**, *26* (1), 679–685. <https://doi.org/10.1021/cm4022003>.
73. Rivnay, J.; Inal, S.; Salleo, A.; Owens, R. M.; Berggren, M.; Malliaras, G. G. Organic Electrochemical Transistors. *Nature Reviews Materials* **2018**, *3* (2), 17086.
74. Braendlein, M.; Pappa, A.-M.; Ferro, M.; Lopresti, A.; Acquaviva, C.; Mamessier, E.; Malliaras, G. G.; Owens, R. M. Lactate Detection in Tumor Cell Cultures Using Organic Transistor Circuits. *Advanced Materials* **2017**, *29* (13), 1605744.
75. Scheiblin, G.; Coppard, R.; Owens, R. M.; Mailley, P.; Malliaras, G. G. Referenceless PH Sensor Using Organic Electrochemical Transistors. *Advanced Materials Technologies* **2017**, *2* (2), 1600141.
76. Khodagholy, D.; Doublet, T.; Quilichini, P.; Gurfinkel, M.; Leleux, P.; Ghestem, A.; Ismailova, E.; Hervé, T.; Sanaur, S.; Bernard, C.; Malliaras, G. G. *In Vivo* Recordings of Brain Activity Using Organic Transistors. *Nature Communications* **2013**, *4*, 1575.
77. A. Bernards, D.; J. Macaya, D.; Nikolou, M.; A. DeFranco, J.; Takamatsu, S.; G. Malliaras, G. Enzymatic Sensing with Organic Electrochemical Transistors. *Journal of Materials Chemistry* **2008**, *18* (1), 116–120.
78. Tseng, H.-R.; Phan, H.; Luo, C.; Wang, M.; Perez, L. A.; Patel, S. N.; Ying, L.; Kramer, E. J.; Nguyen, T.-Q.; Bazan, G. C.; Heeger, A. J. High-Mobility Field-Effect Transistors Fabricated with Macroscopic Aligned Semiconducting Polymers. *Adv. Mater.* **2014**, *26* (19), 2993–2998.

79. Phan, H.; Wang, M.; Bazan, G. C.; Nguyen, T.-Q. Electrical Instability Induced by Electron Trapping in Low-Bandgap Donor–Acceptor Polymer Field-Effect Transistors. *Adv. Mater.* **2015**, *27* (43), 7004–7009.
80. Ford, M. J.; Wang, M.; Phan, H.; Nguyen, T.-Q.; Bazan, G. C. Fullerene Additives Convert Ambipolar Transport to P-Type Transport While Improving the Operational Stability of Organic Thin Film Transistors. *Adv. Funct. Mater.* **2016**, *26* (25), 4472–4480.
81. Wang, M.; Ford, M. J.; Lill, A. T.; Phan, H.; Nguyen, T.-Q.; Bazan, G. C. Hole Mobility and Electron Injection Properties of D-A Conjugated Copolymers with Fluorinated Phenylene Acceptor Units. *Adv. Mater.* **2016**, n/a-n/a.
82. Wang, M.; Ford, M. J.; Zhou, C.; Seifrid, M.; Nguyen, T.-Q.; Bazan, G. C. Linear Conjugated Polymer Backbones Improve Alignment in Nanogroove-Assisted Organic Field-Effect Transistors. *J. Am. Chem. Soc.* **2017**, *139* (48), 17624–17631.
83. Hu, Y.; Rengert, Z. D.; McDowell, C.; Ford, M. J.; Wang, M.; Karki, A.; Lill, A. T.; Bazan, G. C.; Nguyen, T.-Q. Doping Polymer Semiconductors by Organic Salts: Toward High-Performance Solution-Processed Organic Field-Effect Transistors. *ACS Nano* **2018**.
84. Phan, H.; Ford, M. J.; Lill, A. T.; Wang, M.; Bazan, G. C.; Nguyen, T.-Q. Electrical Double-Slope Nonideality in Organic Field-Effect Transistors. *Advanced Functional Materials* **2018**, *28* (17), 1707221.
85. Sirringhaus, H. 25th Anniversary Article: Organic Field-Effect Transistors: The Path Beyond Amorphous Silicon. *Adv. Mater.* **2014**, *26* (9), 1319–1335.
86. Khodagholy, D.; Rivnay, J.; Sessolo, M.; Gurfinkel, M.; Leleux, P.; Jimison, L. H.; Stavrinidou, E.; Herve, T.; Saur, S.; Owens, R. M.; Malliaras, G. G. High Transconductance Organic Electrochemical Transistors. *Nature Communications* **2013**, *4*, ncomms3133.
87. Inal, S.; Rivnay, J.; Leleux, P.; Ferro, M.; Ramuz, M.; Brendel, J. C.; Schmidt, M. M.; Thelakkat, M.; Malliaras, G. G. A High Transconductance Accumulation Mode Electrochemical Transistor. *Advanced Materials* **2014**, *26* (44), 7450–7455.
88. Inal, S.; Rivnay, J.; Sui, A.-O.; Malliaras, G. G.; McCulloch, I. Conjugated Polymers in Bioelectronics. *Acc. Chem. Res.* **2018**, *51* (6), 1368–1376.

89. Inal, S.; Malliaras, G. G.; Rivnay, J. Benchmarking Organic Mixed Conductors for Transistors. *Nature Communications* **2017**, *8* (1), 1767.
90. High-performance transistors for bioelectronics through tuning of channel thickness | Science Advances <http://advances.sciencemag.org/content/1/4/e1400251>
91. Zhang, S.; Hubis, E.; Tomasello, G.; Soliveri, G.; Kumar, P.; Cicoira, F. Patterning of Stretchable Organic Electrochemical Transistors. *Chem. Mater.* **2017**, *29* (7), 3126–3132.
92. Friedlein, J. T.; Donahue, M. J.; Shaheen, S. E.; Malliaras, G. G.; McLeod, R. R. Microsecond Response in Organic Electrochemical Transistors: Exceeding the Ionic Speed Limit. *Advanced Materials* **2016**, *28* (38), 8398–8404.
93. Jimison Leslie H; Tria Scherrine A.; Khodagholy Dion; Gurfinkel Moshe; Lanzarini Erica; Hama Adel; Malliaras George G.; Owens Róisín M. Measurement of Barrier Tissue Integrity with an Organic Electrochemical Transistor. *Advanced Materials* **2012**, *24* (44), 5919–5923.
94. Zhang, S.; Hubis, E.; Girard, C.; Kumar, P.; DeFranco, J.; Cicoira, F. Water Stability and Orthogonal Patterning of Flexible Micro-Electrochemical Transistors on Plastic. *Journal of Materials Chemistry C* **2016**, *4* (7), 1382–1385.

## **Chapter 2:**

### **Experimental Techniques**

#### **2.1 Overview**

This chapter gives a general description of the experimental procedures used in this dissertation. The development of high-performance organic semiconducting materials would not be possible without full material characterization. A wide range of characterization techniques are used to help predict, measure and understand the performance of organic semiconductors.

I will begin by describing how organic semiconducting solutions and films are prepared for devices and characterization in Section 2.2. Before films are prepared on a substrate by a spin coating process, the surface energy can be measured using contact angle measurements (Section 2.3). This is especially useful in cases where a new substrate is being used, where we want to predict if our organic semiconductor will wet the surface effectively. UV-Vis spectroscopy shows us where the material of interest absorbs light, and can be used to look for the presence of a polaron species (Section 2.4). Section 2.5 discusses Ultraviolet and X-ray Photoelectron Spectroscopies (UPS & XPS), a technique which was used to calculate the ionization potential of conjugated polyelectrolytes.

Besides measuring the electronic states and transitions of our material of interest, we must also probe the morphology. Organic semiconducting materials range from completely amorphous, to semi-crystalline and crystalline. The packing of the molecules plays a key role in the ability for charges (whether electronic or ionic) through the material. Atomic force

microscopy (AFM) provides high resolution information on the morphology of the surface of our films (Section 2.6). Grazing incidence wide-angle x-ray spectroscopy (GIWAXS) is able to probe the bulk of the film to provide information on the packing distances in crystalline regions on the film (Section 2.7).

Ultimately, we want to use the organic semiconductors to fabricate devices such as transistors. This process is outlined in Section 2.8. Upon fabrication of the organic transistor device, the electrical characteristics can be probed. Impedance spectroscopy is a powerful tool that can be used to calculate the electrical properties in the bulk and at interfaces to the material. In Section 2.9, I discuss how the technique is used to measure the dielectric constant, electronic conductivity and ionic conductivity of our materials of interest. 3-point probe measurements are performed with a Keithley semiconductor analyzer to determine mobility, electrical stability and switching speed of organic transistors (Section 2.10).

## 2.2 Preparation of Solutions and Thin Films

All materials used to perform my thesis work was synthesized by members of the lab of Professor Guillermo Bazan. PCPDTBT-SO<sub>3</sub>K (CPE-K) was used to prepare the organic electrochemical transistors (OECTs) outlined in chapter 3 and 4. CPE-K is an anionic narrow-band-gap conjugated polyelectrolyte with a  $\pi$ -conjugated cyclopenta-[2,1-b;3,4-b]-dithiophene-alt-4,7-(2,1,3-benzothiazole) (CPDT-alt-BT) backbone. The material was synthesized via Suzuki-Miyaura polymerization reactions outlined in the literature.<sup>5</sup> PhF2,6 is a high mobility p-type D-A semiconducting polymer that was used to fabricate organic field effect transistors described in chapter 5. PhF2,6 is based on 4,4-dihexadecyl-4H-

cyclopenta[1,2-b:5,4-b']dithiophene (CDT) and 2,6-difluorophenylene (2,6-DFPh) and was synthesized following the procedure previously reported.<sup>29</sup>

Solutions of CPE-K were prepared by dissolving CPE-K in a 1:1 mixture of Milli-Q water and methanol to make a 10 mg/mL solution. CPE-K is exclusively soluble in water and methanol was included to speed up evaporation during spin-coating and drop-casting. CPE-K solutions were prepared with (3-glycidyloxypropyl)trimethoxysilane (GOPS), a small molecule that allows for cross-linking of CPE-K through the nucleophilic attack of the sulfonate sidechain of CPE-K on the oxirane of GOPS. The optimal performance in terms of film stability and conductivity was observed at about 8 % GOPS by weight. GOPS solutions seem to lose their efficacy over time, so new solutions were prepared every month, or whenever a new series of experiments was started. Due to the limited shelf life of GOPS solutions, CPE and GOPS solutions were kept separate and mixed right before casting the film. Generally, solutions were drop-casted into the PDMS well. It is also possible to spin cast CPE solutions, however the fact that they are dissolved in water makes it difficult to prepare a thick film due to the slow evaporation rate of water. In this case, 1% by volume of 4-dodecylbenzenesulfonic acid (DBSA) was added to increase the viscosity to promote the formation of thicker CPE films. Spin coating was performed at a speed of 1500 rpm. When drop-casting, the solution was allowed to dry by heating on a hot plate at 80°C. It is important to avoid heating the solution above boiling, because bubbling will result in poor film uniformity. Once dry, films were allowed to cross-link by annealing the film at 110°C for an hour. Preparation of solutions and thin films were prepared under an ambient atmosphere.

PhF2,6 solutions were prepared by dissolving the semiconductor in chlorobenzene at 5 mg/mL. Films for all organic field-effect transistors were prepared by spin-coating at 2000

rpm and then annealing at 200°C for 8 minutes. It is critical for spin-coating to occur in a moisture-free nitrogen environment.

Substrates were cleaned by sonicating in acetone followed by isopropyl alcohol for 10 minutes each. The substrates are then dried with a nitrogen air gun and placed in an oven at 80°C to dry for 15 minutes. The final stage of cleaning the substrates was de-scumming for 15 minutes in a UV-ozone chamber. In the case of substrates used for OECT fabrication, at this point PDMS wells would be fused to the surface of the substrates by exposing both surfaces to an oxygen plasma for 1 minute and placing the PDMS well around the conductive channel. PDMS was prepared from Sylgard<sup>®</sup> 184 from Dow-Corning using a mixing ratio of 10:1 between the base and the curing agent with a curing time of 4 hours at 80 °C. Wells were cut from a sheet of PDMS and fused to the patterned glass substrates using an oxygen plasma for 1 minute.

Indium tin oxide (ITO) films on glass were used as conductive substrate for spectroelectrochemical measurements of CPE-K. CPE-K is able to transduce ionic to electronic signals by changing the redox state of the conjugated backbone when hydrated ions penetrate the bulk of the film. Spectroelectrochemistry monitors the oxidation and reduction of the bulk of the CPE-K film by tracking the evolution of the absorption profile with the CPE-K film biased at various voltages. The ITO is both optically transmissive and conductive, making it an ideal counter electrode for spectroscopic experiments. In order to apply a voltage to the ITO substrate and the CPE film, a copper wire was soldered to the ITO substrate. The connection between the wire and the ITO was then covered in epoxy to limit the leakage current through from the wire to the NaCl solution.

### 2.3 Contact Angle Measurements to Determine the Surface Energy of Thin Films

Contact angle measurements can be used to estimate the surface free energy of a substrate, which can help predict how well a solvent will wet the surface of a substrate when casting a film. **Figure 2.1** shows an image of a drop of water which is used to determine the contact angle.

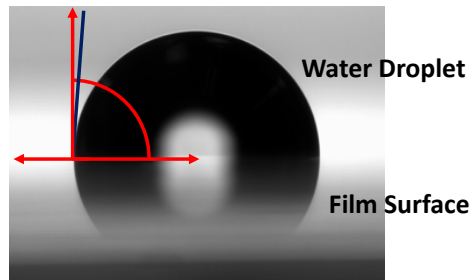


**Figure 2.1:** Contact angle of water on a film surface. The blue line shows the angle that the droplet makes with the surface.

The surface free energy ( $\gamma$ ) is a quantity of the intermolecular interactions that must be disrupted to form a flat surface and can also be viewed as the work required to cut a bulk material in half, creating two surfaces. The contact angle is determined by taking an image of a drop of solvent deposited on the substrate of interest and measuring the angle between the surface and the edge of the drop. The contact angle is described by the Young's equation:

(1)

$$\gamma_{lv} \cos \theta = \gamma_{sv} - \gamma_{sl}$$

Where  $\theta$  is the contact angle,  $\gamma_{sl}$  is the solid/liquid interfacial free energy,  $\gamma_{lv}$  is the liquid/vapor interfacial free energy and  $\gamma_{sv}$  is the solid/vapor interfacial free energy. While the surface free energy of the liquid ( $\gamma_l$ ) of most solvents can be found in tables in the literature,

the surface free energy of the solid ( $\gamma_s$ ) of the substrate of interest must at times be experimentally determined. In order to determine  $\gamma_s$ , we use a technique developed by Owens, Wendt, Rabel and Kaelble (OWRK) that requires contact angle measurements.<sup>1,2</sup> In the OWRK method,  $\gamma_s$  is divided into a polar (permanent dipole-dipole interactions) and a dispersive component (London forces). The technique involves the determination of the contact angle of two solvents, water and diiodomethane, where the former is assumed to be dominated by polar forces, and the latter by dispersion forces. The dispersion forces component can be calculated using the measured contact angle of diiodomethane and the following equation:

(2)

$$1 + \cos\theta = 2 * \sqrt{\gamma_s^d} \left( \frac{\sqrt{\gamma_l^d}}{\gamma_{lv}} \right)$$

Where  $\gamma_s^d$  and  $\gamma_l^d$  is the dispersion component of  $\gamma_s$  and  $\gamma_l$ , respectively, and  $\gamma_l^d$  is known from the literature. The polar component is determined with the contact angle of water and by plugging in the dispersion component determined from diiodomethane into the following equation:

(3)

$$1 + \cos\theta = 2 * \sqrt{\gamma_s^d} \left( \frac{\sqrt{\gamma_l^d}}{\gamma_{lv}} \right) + 2 * \sqrt{\gamma_s^p} \left( \frac{\sqrt{\gamma_l^p}}{\gamma_{lv}} \right)$$

Where  $\gamma_s^p$  and  $\gamma_l^p$  is the polar component of  $\gamma_s$  and  $\gamma_l$ , respectively, and  $\gamma_l^p$  is known from the literature. Once the contact angle of both solvents on the substrate of interest have been

measured, the polar and dispersion contributions can be combined to calculate  $\gamma_s$  of the substrate of interest. By combining  $\gamma_s^d$  and  $\gamma_s^p$ , we obtain  $\gamma_s$ , the surface free energy of the solid of the substrate of interest.  $\gamma_s$  can be used to predict how well a solvent will wet a substrate. The ability to wet a surface is quantified by the spreading parameter ( $S$ ) and is described by the following equation:

(4)

$$S = \gamma_s - \gamma_l - \gamma_{sl}$$

Where  $S$  is the spreading parameter. As a rule, high energy surfaces are more easily wet than low energy surfaces, and a solvent will more completely wet a surface when the liquid has a much lower surface energy than the surface.<sup>3</sup>

## 2.4 UV-Vis Spectroscopy

UV-Vis spectroscopy is a technique that is used to measure the wavelengths of light where a material absorbs. The material can either be in solution in a cuvette, or deposited as a film on a substrate that is transmissive to the wavelengths of interest. All UV-vis-nIR spectra were obtained using a Perkin-Elmer Lambda 750 UV-vis-nIR spectrometer using a tungsten lamp for the visible to near-IR region and a deuterium lamp for the UV region. A 100% transmission blank was obtained using a clean indium tin oxide/glass substrate for all spectra. In spectroelectrochemistry experiments, CPE-K films were prepared on a cleaned ITO-coated glass substrate. A wire was soldered to the edge of the ITO substrate and the contact point was covered with epoxy to limit leakage current. The CPE-K film and a Ag/AgCl electrode were

placed in a cuvette filled with a 0.1 M NaCl solution. A constant bias was applied using a DC power source.

## **2.5 Ultraviolet and X-ray Photoelectron Spectroscopies (UPS & XPS)**

Ultraviolet photoelectron spectroscopy can be used to measure the HOMO and LUMO levels of organic semiconductors. UPS was carried out with a Kratos Axis Ultra X-ray Photoelectron Spectroscopy (XPS) system on drop casted films prepared from 30  $\mu\text{L}$  of a solution of 10 mg/mL CPE materials on top of ITO coated glass substrates. A clean piece of silver was argon etched to get the exact zero position of the system for an accurate calibration of the energy scale. The ionization potential of each CPE material was determined by subtracting the width of the high-binding cutoff and the highest occupied state (HOS) from the 21.22 eV of the incident photon. The data was processed using CasaXPS<sup>©</sup> software.

## **2.6 Atomic Force Microscopy**

Atomic force microscopy (AFM) is a technique that can be used to probe the surface morphology of materials. A sample is mounted on top of a stage and a reflective cantilever with a sharp tip is lowered to the surface of the sample. Feedback of the proximity of the tip to the surface of the sample is provided by a laser that is reflected off of the cantilever. The reflected laser is adjusted to strike a photodiode and slight deflections of the cantilever result in a change in the signal received from the photodiode.

In contact mode AFM, the tip is pulled along the surface at a defined force. As the height of the surface increases, the increased force on the cantilever causes a deflection of the laser that provides the feedback to raise the tip with a piezoelectric to return the cantilever to the initial amount of force. A large downside of contact mode AFM is that tips get quickly worn down as it is dragged across the surface. Tapping mode AFM is an improved way to scan the surface morphology of a surface. A piezo is used to oscillate the cantilever at its resonant frequency that gives a sinusoidal photodiode signal. As the tip gets closer to the surface, the oscillation of the cantilever is dampened and the height of the photodiode sinusoidal signal is reduced. This dampening effect causes the z-height piezo to raise the cantilever, which provides the feedback loop to scan the surface. Just like in contact mode, the tip is rastered across the surface of the sample to stitch together an image of the surface morphology. Tapping mode is especially suitable for soft surfaces such as organic semiconductors, where contact mode would potentially scratch into the surface.

All topographic images were obtained using an Asylum MFP-3D mounted atop an Olympus inverted optical microscope under and inert atmosphere. Silicon tips with a resonant frequency of 300 kHz and a force constant of 40 N/m were used (Budget Sensors). First order image flattening was performed on the morphology images on Asylum Research AFM software version 14, programmed using IGOR Pro.

## **2.7 Grazing Incidence Wide-Angle X-Ray Spectroscopy**

Grazing incidence wide-angle x-ray spectroscopy is a technique that can give information on the packing of crystalline regions of organic small molecules and polymers.

The technique requires a synchrotron source of x-rays that are shined at a low angle at the organic thin film of interest. The x-ray is shined at a low angle in order to maximize the distance that the beam travels through the film in order to maximize the signal. The x-ray beams shine through the bulk of the sample until they are reflected by the substrate, which is generally made of silicon or silicon dioxide. The scattered x-ray light is collected by a detector and is then plotted in inverse distance in the x-y and z direction. In order to observe a peak in either the  $q_{xy}$  or  $q_z$  direction, the x-ray must be scattered by a repeating pattern, meaning that GIWAXS only provides information on crystalline regions of the film. In general, the scattering in the  $q_{xy}$  and  $q_z$  directions are generally attributed to edge-on and face-on stacking, respectively. **Figure 2.2** summarizes the working principle of GIWAXS to probe organic semiconductor morphology. Shorter  $\pi$ - $\pi$  stacking distances have been attributed to higher mobility values, due to the shorter hopping distance between neighboring organic small molecules or polymers.

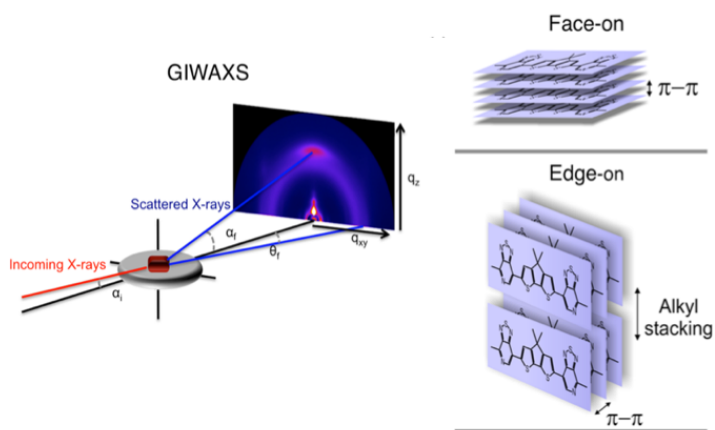


**Figure 2.2:** Probing the film morphology with GIWAXS. The scattering in the  $q_{xy}$  and  $q_z$  directions are generally attributed to edge-on and face-on stacking, respectively. Figure is adapted from *Perez et al.*<sup>4</sup>

## 2.8 Organic Field-Effect Transistor and Organic Electrochemical Transistor

### Fabrication

This dissertation contains research on two types of transistor devices: organic field-effect transistors (OFETs) and organic electrochemical transistors (OECTs). Their fabrication was performed using the equipment available in the Nguyen research lab and the nanofabrication facility at UC Santa Barbara.

Both OFET and OECT fabrication begins the same way: a silicon wafer is cleaned and brought to the UCSB nanofabrication facility for lithography to define the metal contacts. The wafer is covered by a positive photoresist by spin coating the solution. The photoresist is cross-linked by annealing on a hotplate and a lithography mask is placed on the wafer to define where the metal for the contacts will be deposited. The lithography mask is made of a solid piece of quartz that is covered in chromium on one side, except for the areas that define the contacts. In these areas, UV light is able to shine through the mask on to the photoresist on the wafer. Photoresist that has been exposed to UV light is no longer cross-linked and may now be selectively washed away with solvents. A combination of solvents is used to wash away the photoresist to expose the underlying wafer in the desired pattern.

Now that we have defined the area where we will deposit the metal contacts, we may now evaporate the desired metal via thermal or e-beam evaporation. In thermal evaporation, a tungsten wire or boat is resistively heated to the point that the desired metal is evaporated. E-beam evaporation is a similar process, except that the desired metal is heated by an electron beam. Both processes are under vacuum ( $\sim 10^{-7}$  Torr). The evaporated metal travels from the metal source to the surface of the wafer, but only reaches the wafer where the photoresist has

been removed by lithography. The photoresist is removed in a process called “lift-off” where is removed by a solvent which exposes the patterned wafer. The wafer can now be cut into individual devices with a dicing saw. **Figure 2.1** shows the general procedure for lithography.

The individual patterned substrates may now be used to fabricate OFETs and OECTs by spin coating or drop casting the polymer solution on to the substrate. In the case of OECTs, a PDMS well is prepared first. PDMS wells help retain the electrolyte solution over the channel of the OECT and away from the gold contacts to reduce leakage current. Often organic semiconductors are annealed to give the film enough energy to relax to a conformational state that allows for more efficient charge transport. Now that we have fabricated the transistor, we can begin electrical characterization.

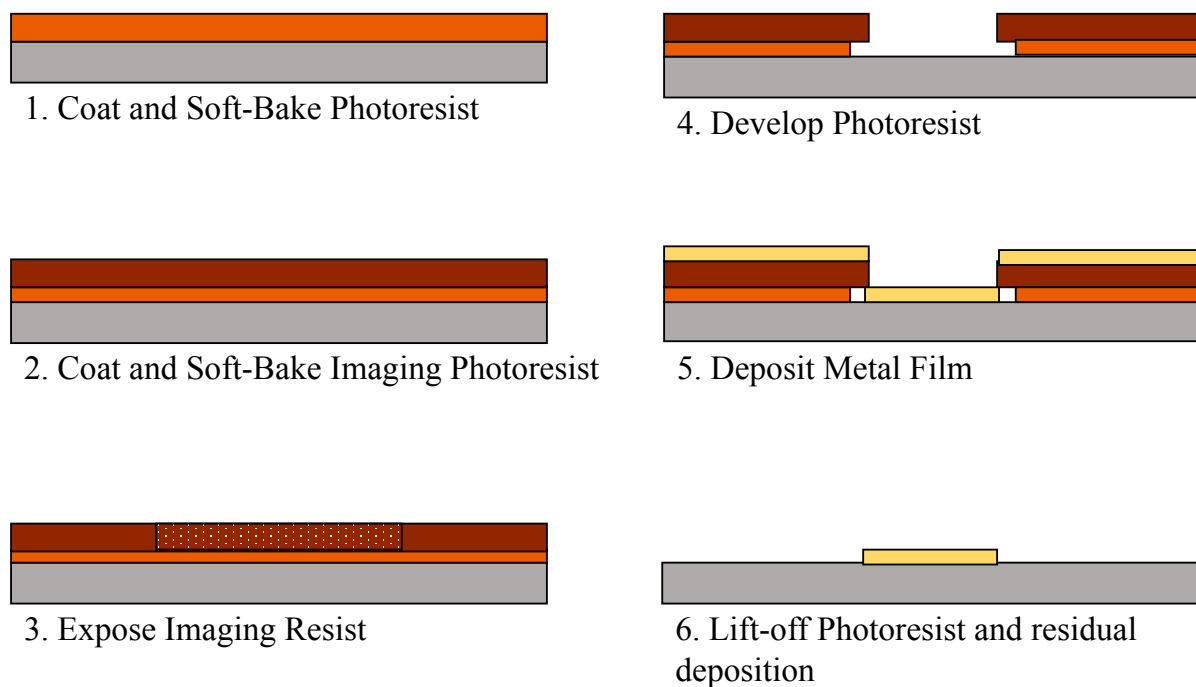


**Figure 2.3:** General procedure for lithography to define the metal contacts for an organic transistor device.

## 2.9 Impedance Spectroscopy

Impedance spectroscopy is a powerful technique that can be used to characterize multiple electrical properties of materials in their bulk and at their interfaces. For example, impedance spectroscopy can be used to probe the dynamic motion of bound and mobile charges in solid or liquid materials. This includes materials that are ionic, semiconducting, mixed ionic-electronic conductors, and dielectrics.

The impedance of a system is defined as the electric resistance of that system to AC. The electrical circuit of a system can be split apart into its components parts which usually consists of resistive, inductive and capacitive components. A voltage is applied at a specific frequency to the system and follows the equation  $V = V_0 \sin(\omega t)$ , where  $\omega$  stands for the angular frequency  $2\pi f$ . The resulting current response through the system follows the equation  $I = I_0 \sin(\omega t + \phi)$ , where  $\phi$  is the phase difference between the applied voltage and the resultant current flow. This phase difference is dependent of the frequency that is applied to the system. The impedance of the system can be defined as a complex number, which can be expressed by real,  $Z'$ , and imaginary,  $Z''$ , components as  $Z^* = Z' + iZ''$  and is plotted in what is known as a Nyquist plot.

Impedance spectroscopy can be used to measure the ionic and electronic conductivity of mixed ionic-electronic conductors and the capacitance of dielectric layers used in organic field-effect transistors and organic electrochemical transistors.<sup>5-7</sup> A Solartron SI 1260A impedance analyzer was used for all impedance measurements described below.

Electrochemical impedance spectroscopy (EIS) can be used to measure the ionic and electronic motion in mixed conductors. In this thesis, I describe how EIS was used to measure the ionic conductivity of a series of conjugated polyelectrolytes (Chapter 4.3). CPE-Na with

varying sidechain lengths was used to explore the effect of sidechain length of ionic conductivity. CPE-X-Na films were deposited on top of interdigitated gold electrodes to increase the signal-to-noise ratio and an AC voltage of 20mV was applied at a frequency from 10 Hz to 10 MHz between each electrode. The Nyquist plot data were fitted in **Figure 2.4** using the circuit shown in **Figure 2.5**.

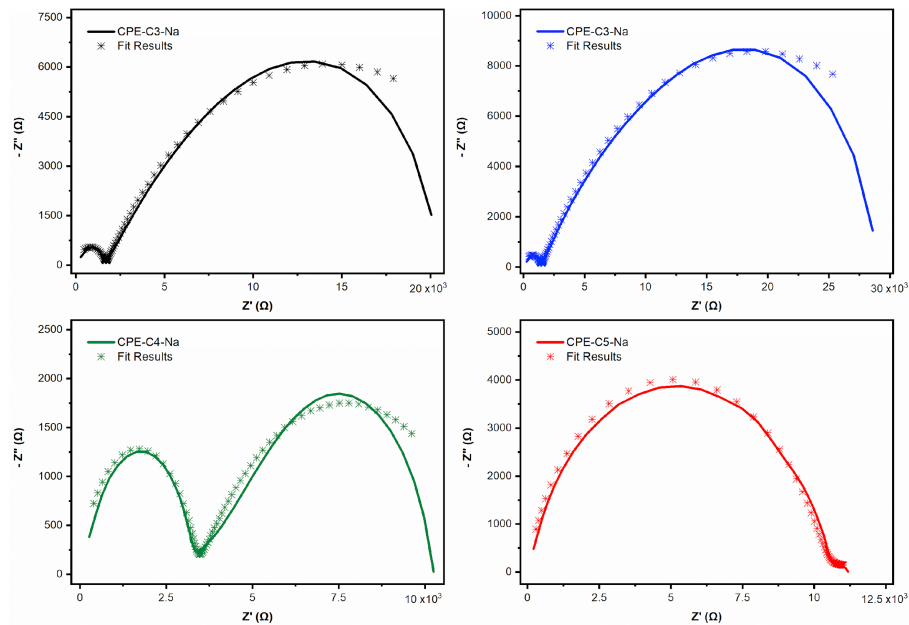


**Figure 2.4.** Nyquist plots of each CPE material generated by electrochemical impedance spectroscopy (EIS) measurements for each CPE.

The ionic conduction is represented by a constant phase element (CPE-dl) in series with an ion resistance (R-ion). These are presented in series due to the ion blocking nature of gold contacts. Since gold contacts are not hole blocking, we expect to see hole conduction presented by a constant phase element (CPE-bulk) parallel to hole resistance (R-e). Since CPE's are mixed conductors, we expect to see ionic and electronic carriers transporting simultaneously.

As a result, both ion and hole circuit elements are shown parallel to each other. The Nyquist plot data was fit to the circuit using the ZView impedance spectroscopy software.

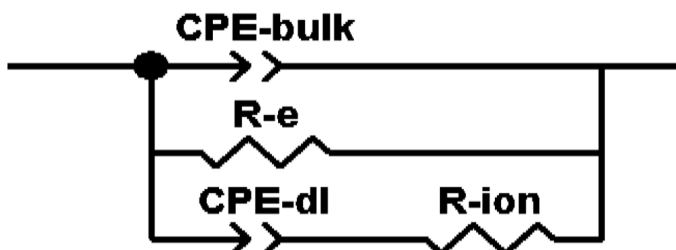


**Figure 2.5** Circuit diagram used to fit Nyquist plots to determine ion conductivity of each CPE derivative.

## 2.10 Organic Transistor Electrical Characterization

The main instrument that was used to characterize the organic transistors described in this dissertation is a Keithley semiconductor parametric analyzer (model 4200-SCS) and a probe station kept under a nitrogen atmosphere in a glove box. Please refer to Chapter 1.2 for more information on the electrical characterization of organic transistors.

Organic field-effect transistors were tested using a probe station under a nitrogen atmosphere in a glovebox. Organic electrochemical transistors were tested at a probe station under ambient atmosphere. Three needle probes are used to make contact to the source, drain and gate electrodes and the Keithley semiconductor analyzer is able to apply voltages and measure precise current levels. This capability was used to measure output and transfer curves

of OFETs and OECTs to determine figures of merit such as mobility, hysteresis, threshold voltage and on-off ratio.

The electrical stability of various dielectric layers were tested by applying a constant gate and source-drain voltage and monitoring the source-drain current over time. These measurements were performed over multiple hours to determine the rate of current decay and charge trapping occurring at the interface between the semiconducting and dielectric layers. This work is outlined in Chapter 5 of this dissertation. We were able to measure the activation energy of charge hopping in an organic semiconducting polymer with a probe station that has a stage that is able to be cooled with liquid nitrogen. The chamber is under vacuum and the stage temperature can be precisely controlled with a heating element and liquid nitrogen. By plotting the mobility versus temperature, we are able to calculate the activation energy of charge hopping with the Arrhenius equation. This project is outlined in Chapter 6.3.

## 2.11 References

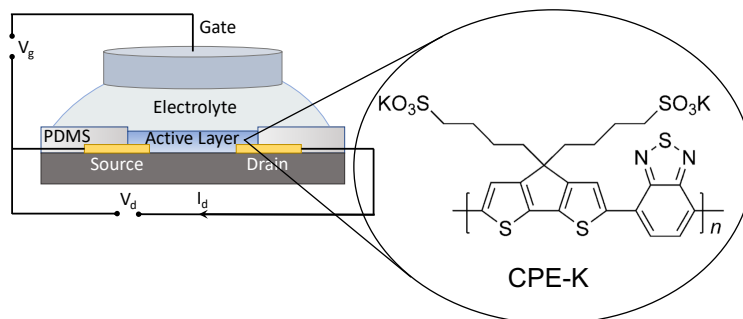
1. Owens, D. K.; Wendt, R. C. Estimation of the Surface Free Energy of Polymers. *J. Appl. Polym. Sci.* **1969**, *13* (8), 1741–1747.  
<https://doi.org/10.1002/app.1969.070130815>.
2. Kaelble, D. H. Dispersion-Polar Surface Tension Properties of Organic Solids. *The Journal of Adhesion* **1970**, *2* (2), 66–81.
3. Janssen, D.; De Palma, R.; Verlaak, S.; Heremans, P.; Dehaen, W. Static Solvent Contact Angle Measurements, Surface Free Energy and Wettability Determination of Various Self-Assembled Monolayers on Silicon Dioxide. *Thin Solid Films* **2006**, *515* (4), 1433–1438.
4. Perez, L. A.; Zalar, P.; Ying, L.; Schmidt, K.; Toney, M. F.; Nguyen, T.-Q.; Bazan, G. C.; Kramer, E. J. Effect of Backbone Regioregularity on the Structure and Orientation

- of a Donor–Acceptor Semiconducting Copolymer. *Macromolecules* **2014**, *47* (4), 1403–1410.
5. Dong, B. X.; Nowak, C.; Onorato, J. W.; Strzalka, J.; Escobedo, F. A.; Luscombe, C. K.; Nealey, P. F.; Patel, S. N. Influence of Side-Chain Chemistry on Structure and Ionic Conduction Characteristics of Polythiophene Derivatives: A Computational and Experimental Study. *Chem. Mater.* **2019**, *31* (4), 1418–1429.
  6. Dong, B. X.; Liu, Z.; Misra, M.; Strzalka, J.; Niklas, J.; Poluektov, O. G.; Escobedo, F. A.; Ober, C. K.; Nealey, P. F.; Patel, S. N. Structure Control of a  $\pi$ -Conjugated Oligothiophene-Based Liquid Crystal for Enhanced Mixed Ion/Electron Transport Characteristics. *ACS Nano* **2019**, *13* (7), 7665–7675.
  7. Dong, B. X.; Bennington, P.; Kambe, Y.; Sharon, D.; Dolejsi, M.; Strzalka, J.; Burnett, V. F.; Nealey, P. F.; Patel, S. N. Nanoscale Film Conductivity Measurements Reveal Interfacial Influence on Ion Transport in Polymer Electrolytes. *Mol. Syst. Des. Eng.* **2019**, *4* (3), 597–608.

## Chapter 3:

### Organic Electrochemical Transistors Based on the Conjugated Polyelectrolyte

#### PCPDTBT-SO<sub>3</sub>K (CPE-K)



### 3.1 Introduction

PCPDTBT-SO<sub>3</sub>K (CPE-K), a conjugated polyelectrolyte, is presented as a mixed conductor material which can be used to fabricate high transconductance accumulation mode organic electrochemical transistors (OECTs). OECTs have been utilized in a wide range of applications such as analyte detection, neural interfacing, impedance sensing and neuromorphic computing. We demonstrate the use of interdigitated contacts to enable high transconductance in a relatively small device area in comparison to standard contacts. Such characteristics are highly desired in applications such as neural activity sensing, where device area must be minimized to reduce invasiveness. The physical and electrical properties of CPE-K have been fully characterized to allow a direct comparison to other top performing OECT materials. CPE-K demonstrates an electrical performance that is among the best that have been reported in the literature for OECT materials. In addition, CPE-K OECTs operate in the

accumulation mode, which allows for much lower energy consumption in comparison to commonly used depletion-mode devices.

### 3.2 Operational Mechanism of Organic Electrochemical Transistors

Organic electrochemical transistors (OECTs) have been actively researched for bioelectronic applications owing to their low operational voltage and compatibility with aqueous environments.<sup>[1,2]</sup> OECTs have been demonstrated in a variety of life science applications, such as miniaturized biosensors for analyte detection<sup>[3–11]</sup>, pH-sensing<sup>[12,13]</sup>, and *in vivo* neural recording and modulation.<sup>[14–17]</sup> OECTs modulate the bulk conductivity of the organic (semi-)conductor channel by changing the doping state of the conjugated backbone through injection of hydrated ions under an applied voltage.<sup>[18,19]</sup> In a device, electrochemical potentials (i.e. Ag/AgCl gate electrode, nerve impulse) can drive ions into or out of the charge conducting layer, thereby transducing ionic signals into electronic signals. The most common organic conducting material used in OECTs is poly(3,4-ethylenedioxythiophene) polystyrene sulfonate (PEDOT:PSS); however, its complex macromolecular structure makes it unable to act as a model material for studying chemical structure - device performance relationships.<sup>[20]</sup> Other materials should be explored to improve the performance of OECTs. These challenges have increased the need to develop alternative materials as the active layer in OECTs. While the large majority of OECT research still utilizes poly(3,4-ethylenedioxythiophene) polystyrene sulfonate (PEDOT:PSS) as the active layer, a few new OECT materials have been recently reported.<sup>[21–35]</sup>

### 3.3 Conjugated Polyelectrolytes, Their Applications and the Research Motivation

Conjugated polyelectrolytes (CPEs) represent a promising and unique class of materials which are characterized by their conjugated carbon backbone and pendant ionic chains. CPEs have been used in DNA-detection, thermoelectric devices, dye-sensitized solar cells, and as interlayers in organic light-emitting diodes (OLEDs), organic field-effect transistors (OFETs), and organic photovoltaics (OPVs).<sup>[36–42]</sup> Their water solubility in addition to their electronic and ionic conductivity makes them an ideal candidate for OECT applications. Accumulation mode OECTs using a CPE active layer have been fabricated in the past; however, their chemical structures have been limited to thiophene-based backbones.<sup>[21,43]</sup> Synthetic chemists designing OECT materials should consider the lessons learned by the OFET community such as the dramatic improvement in electronic mobility that has been observed in donor-acceptor (D-A) copolymers in comparison to homopolymers.<sup>[44–46]</sup> New OECT materials must be synthesized and characterized to establish a better understanding of the design principles required for desirable OECT performance. In this contribution, we present the use of the conjugated polyelectrolyte poly[2,6-(4,4-bis-potassium butanysulfonate-4H-cyclopenta-[2,1-b;3,4-b']-dithiophene)-alt-4,7-(2,1,3-benzothiadiazole)] (PCPDTBT-SO<sub>3</sub>K or CPE-K) as an active layer in OECTs. CPE-K contains cyclopentadithiophene (CPDT) and benzothiadiazole (BT) alternating D-A units and has been previously reported as a pH neutral (pH = 7.56) interlayer in OPVs and as an active layer in thermoelectric devices.<sup>[47,37,48]</sup> CPE-K is highly conductive because it is self-doped by the

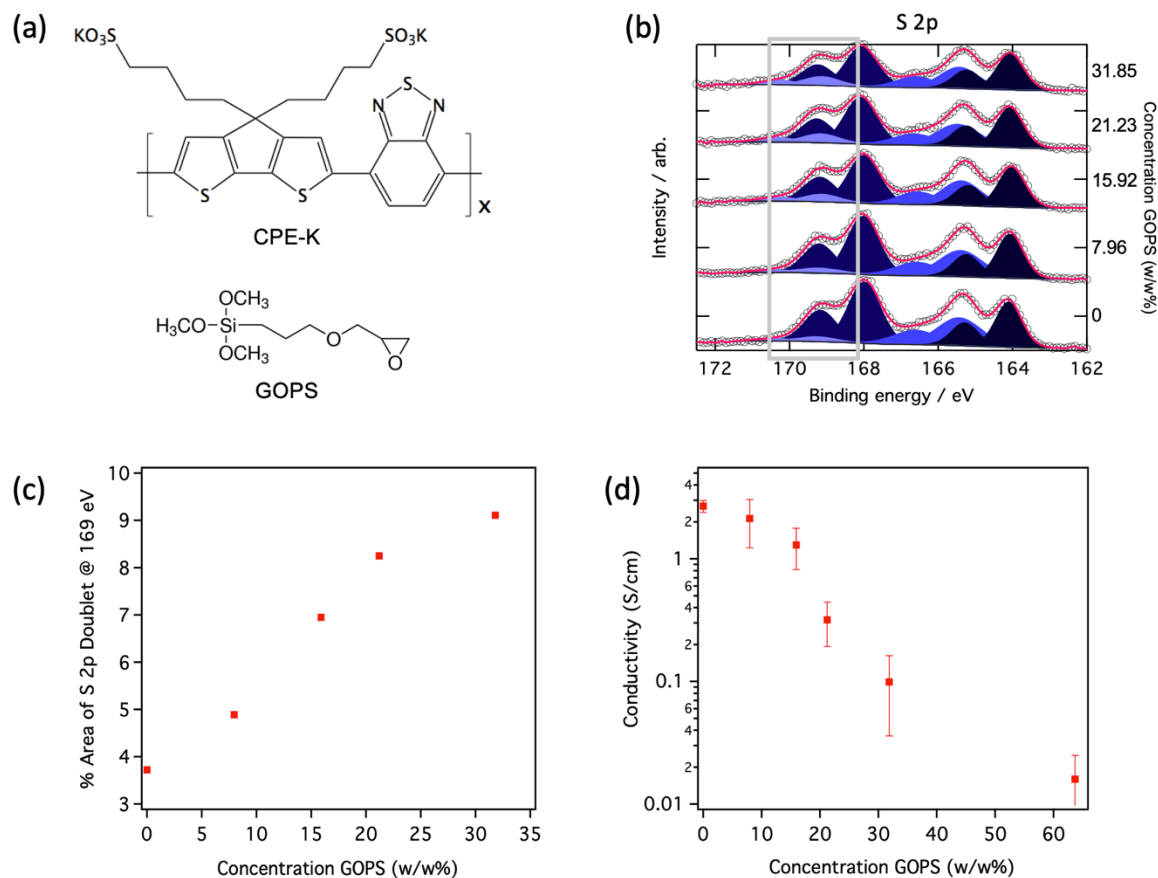
stabilization of polarons on the conjugated backbone by the sulfonate sidechains.<sup>[49]</sup> We demonstrate that CPE-K is among the highest performing OECT materials reported in the literature by clearly defining device geometries and operating voltages for ease of comparison. In addition, we discuss the advantages of using interdigitated contacts to increase transconductance and explore the mechanism behind the stabilization of CPE-K with a cross-linking agent. Impedance spectroscopy, transient measurements and spectroelectrochemical measurements are utilized to shed light on the operational mechanism of accumulation mode OECTs made from CPE-K. This work is the first step in developing D-A copolymer CPE materials for next-generation high performance OECTs.

#### **3.4 Stabilization of CPE-K films with (3-glycidyloxypropyl)trimethoxysilane (GOPS)**

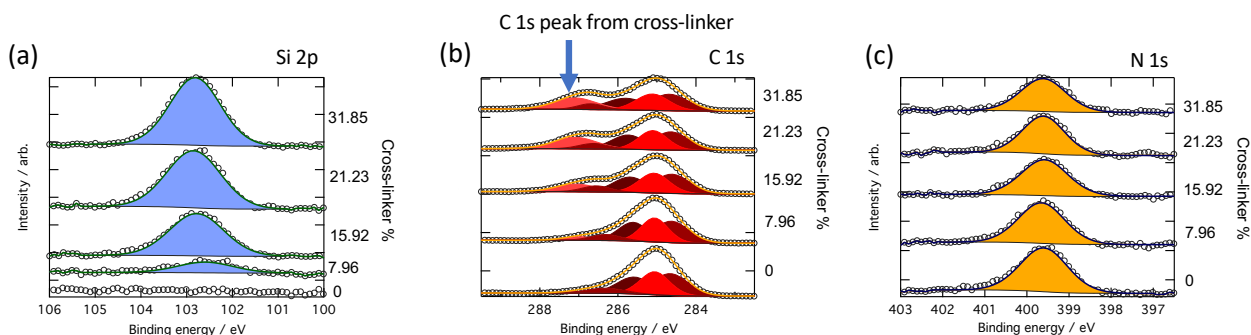
CPE-K consists of a conjugated backbone for electronic conductivity and pendant alkyl sulfonate groups that render the material processable in aqueous solution. CPE-K films must first be stabilized with a cross-linker before it can be utilized as the active layer of an OECT. OECTs generally operate with an electrolytic solution over the device channel, and CPE-K dissolves in a matter of seconds if the film is not previously stabilized. CPE-K solutions were prepared with (3-glycidyloxypropyl)trimethoxysilane (GOPS), a molecule which has been used to stabilize PEDOT:PSS films in OECTs and immobilize DNA on metal oxide surfaces.<sup>[20,50]</sup> **Figure 3.1a** contains the chemical structure of CPE-K and GOPS. X-ray photoelectron spectroscopy was used to explore the mechanism of how CPE-K is successfully stabilized with GOPS. One possible mechanism involves the direct reaction of GOPS with the sulfonate moiety on the sidechain of CPE-K. This mechanism would be analogous to the cross-linking mechanism observed between GOPS and PEDOT:PSS, where the reactive epoxide of

GOPS is opened by the sulfonate of PEDOT:PSS.<sup>[51]</sup> An alternative process could be the formation of a cross-linked network of GOPS with itself within the CPE-K film, thereby stabilizing the film. XPS was performed on films containing increasing percentages of cross-linker ranging from 0 % to 32 % (w/w) GOPS. The region of the XPS spectra of the S 2p core level region corresponding to the sulfur atom of the sulfonate side chain was monitored to determine if there was a change in the signal corresponding to the sulfonate reacting upon the addition of cross-linker. **Figure 3.1b** shows the photoelectron spectra from 162 to 172 eV that contains the signals of the S 2p core level region. There are three unique sulfur atoms in the chemical structure of CPE-K and their signals appear as doublets split by 1.18 eV. The signals at 164.0 and 165.4 eV correspond to the thiophene and benzothiadiazole sulfur atoms, respectively. The signal at 168.1 eV corresponds to the sulfur atom of the sulfonate functional group.<sup>[52-54]</sup> A new peak around 169 eV is observed as GOPS is added, which corresponds to the reaction of the sulfur of the sulfonate functional group of the CPE-K forming a covalent bond with GOPS. These results suggest that the sulfonate of CPE-K is a strong enough nucleophile to react with the electrophilic carbon center at the epoxide ring of GOPS. The percent area of the S 2p doublet at 169 eV increases from about 4 % to 9 %, corresponding well to the increased amount of cross-linked sulfonate groups on CPE-K (**Figure 3.1c**). As the amount of GOPS is increased from 0 % to 32 % (w/w), a Si 2p peak around 103 eV and a C1s peak around 287 eV appear in the XPS spectra (**Figure 3.2**). These peaks are unique to the cross-linker and are expected to appear as cross-linker is added. We did not observe any change in the N 1s signal around 399-400 eV, suggesting that there was no reaction with the nitrogen on CPE-K as cross-linker was added. According to the XPS data, GOPS reacts with the sulfonate functional group on CPE-K, thereby making it insoluble in water. **Figure 3.3**

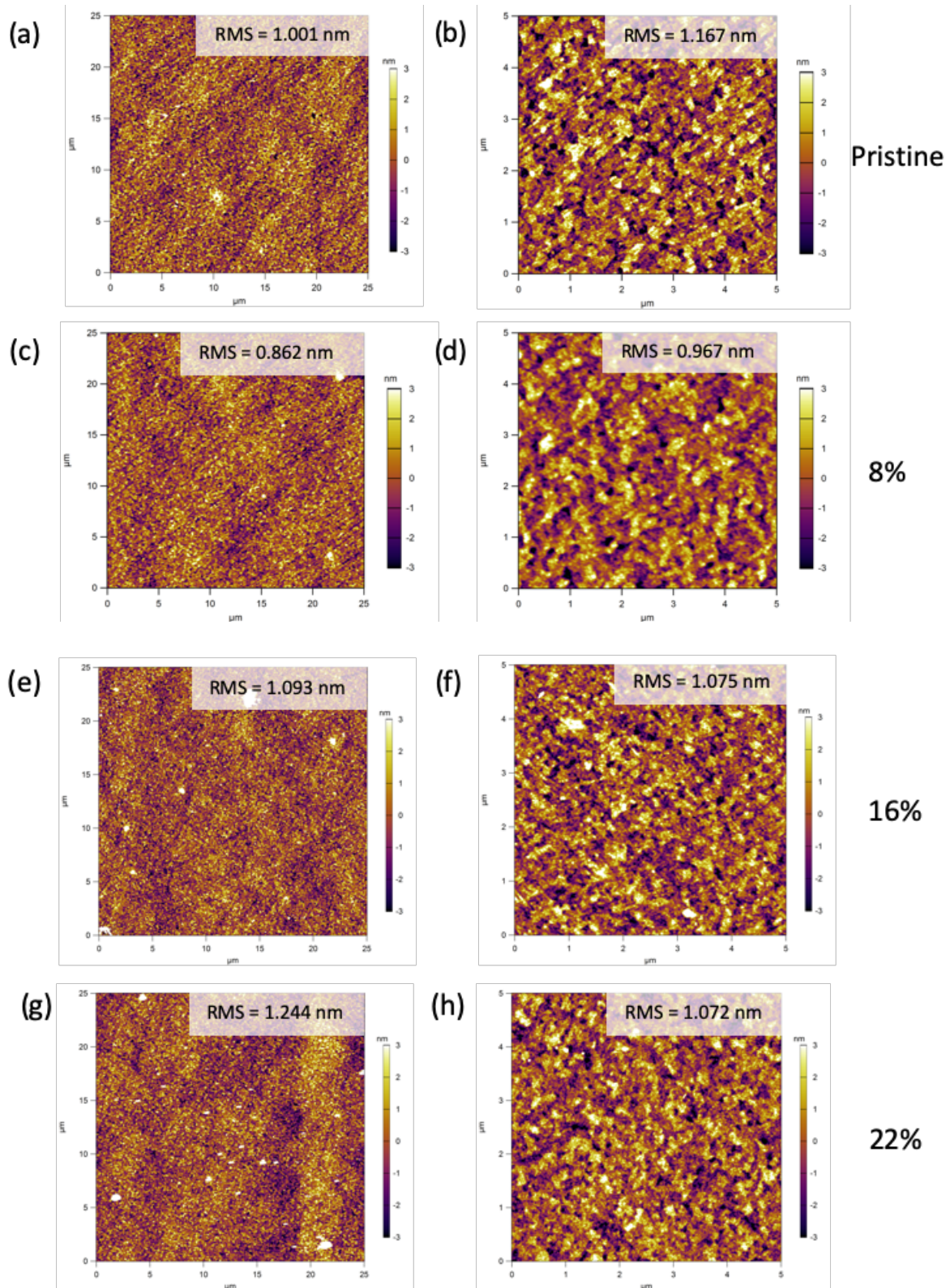
contains height images measured by atomic force microscopy (AFM) of CPE-K thin films made using increasing amounts of GOPS cross-linker. The surface morphology of pristine CPE-K is uniform and smooth (root mean square roughness = 1.00-1.17 nm). As the percentage of cross-linker present in the CPE-K film is increased from 8 % to 64 % (w/w) an increasing amount of aggregates appear on the film surface; however, the surface roughness remains below 1.5 nm. No dramatic change in the surface morphology was observed by AFM as a function of GOPS added to the CPE-K film. A simultaneous reduction in conductivity when increasing the amount of cross-linker added to the CPE-K solution (**Figure 3.1d**) can be observed. A maximum conductivity of 2.7 S/cm is reached in the pristine CPE-K film. Conductivity is reduced down to  $1.2 \times 10^{-2}$  S/cm as the amount of crosslinker is increased to 64 % (w/w). The sulfonate group on CPE-K stabilizes the polaron on the backbone, so naturally a reduction in conductivity is observed as the sulfonate group reacts with the GOPS cross-linker. As a result, a balance between film stability and conductivity must be found. The optimal performance in terms of film stability and conductivity was observed at about 8 % (w/w) crosslinker with a conductivity of 2.1 S/cm. Below this concentration, CPE-K films were not reliably stable in DIW.



**Figure 3.1:** (a) Chemical structures of CPE-K and GOPS (b) XPS of sulfur orbital signals of CPE-K films with increasing percentages of GOPS. The grey box highlights the region corresponding to the sulfur in the sulfonate group. (c) Percent area of S 2p doublet at 169 eV as a function of percent GOPS cross-linker shows an increase in area as cross-linker percentage is increased. (d) Conductivity of CPE-K films versus concentration (%w/w) of GOPS crosslinker.



**Figure 3.2:** XPS spectra regions corresponding to the binding energy of (a) silicon 2p (b) carbon 1s and (c) nitrogen 1s orbitals.



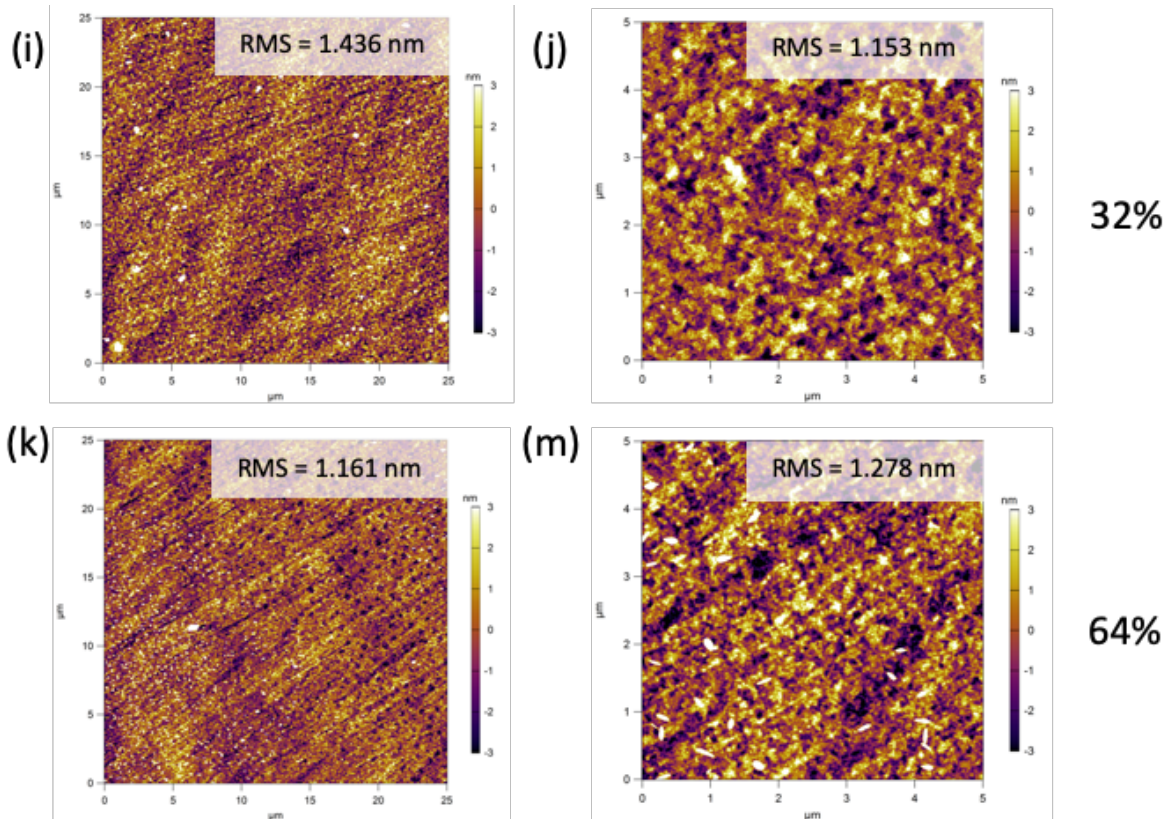


**Figure 3.3:** Morphology measured by AFM of CPE-K films prepared from solution with various amounts of GOPS cross-linker (w/w%).

### 3.5 Transfer Characteristics and Transient Behavior of CPE-K OECTs

OECTs were fabricated using the conjugated polyelectrolyte CPE-K. An OECT consists of an organic (semi-)conducting film deposited on top of metal source and drain electrodes that define the channel of the OECT. Electrical current flows from the source to the drain under an applied bias. The conductivity of the channel is modulated by a gate electrode that is immersed in an electrolyte deposited on top of the channel. Ions are driven into the film under an applied bias and alter the doping state and hence the conductivity of the channel. Polydimethylsiloxane (PDMS) wells were bonded to cleaned glass substrates by exposing both surfaces to an oxygen plasma before placing the well. The purpose of incorporating the PDMS

well was to keep the electrolyte contained above the channel area and to reduce the leakage current between the source and drain contacts and the gate electrode. The glass substrates contained thermally evaporated gold contacts patterned by clean-room lithography techniques and CPE-K films were deposited by drop-casting into the PDMS well. The OEECTs fabricated for this study utilize a 0.1 M solution of NaCl as the gate electrolyte and a Ag/AgCl pellet as the gate electrode. **Figure 3.4a** contains the general device architecture of OEECTs fabricated for this study. The transfer characteristics of CPE-K-based OEECTs were evaluated by monitoring the current between the source and drain contacts ( $I_D$ ) while applying a constant drain voltage ( $V_D$ ) under a series of gate voltages ( $V_G$ ) (**Figure 3.4b**). The OEECT operates in the p-type accumulation mode, meaning that the current is lowest when there is no voltage applied to the gate, and the current gradually increases as negative voltage is applied to the gate. Accumulation mode OEECTs consume relatively low power in comparison to depletion mode OEECTs, because they are generally in the OFF state. Depletion mode devices, such as OEECTs made from PEDOT:PSS, are generally in the ON state, and a voltage must be applied to reduce the current between the source and drain electrodes. The slope of the transfer curve was used to calculate the transconductance ( $g_m = \frac{\delta I_D}{\delta V_G}$ ) at each  $V_g$ . A larger magnitude in transconductance corresponds to a more sensitive OEECT. A peak transconductance of about 4 mS was observed at -0.55V with channel width, length, and thickness of 1000  $\mu\text{m}$ , 40  $\mu\text{m}$  and 0.6  $\mu\text{m}$ , respectively. Interdigitated contacts can be used to dramatically increase the transconductance of the OEECTs by increasing the channel width. A peak transconductance of 68.1 mS was measured at -0.43V for CPE-K-based OEECTs with interdigitated contacts (**Figure 3.4c**). The channel width, length, and thickness of the active layer of the interdigitated OEECT are 27  $\mu\text{m}$ , 8  $\mu\text{m}$  and 3  $\mu\text{m}$ , respectively. Interdigitated contacts allow for an increase in

transconductance within the same device area as compared to OECTs prepared using standard contacts. In applications where rapid switching speed is required, interdigitated contacts allow for the film thickness to be reduced while keeping transconductance sufficiently large.<sup>[55]</sup> This is particularly important in bioelectronics applications such as neuron recording, where the device area must be minimized to reduce invasiveness and ensure signals that correspond to single neurons or bundles of neurons.<sup>[14,55]</sup> **Figures 3.5a and 3.5b** show the typical output characteristics of OECTs made with standard and interdigitated contacts, respectively. The switching time of OECTs based on the polymer CPE-K was measured by recording  $I_D$  while applying a square wave function to  $V_G$  at a frequency of 100 Hz (**Figure 3.4d**). The data was fit with an exponential decay according to the Bernardis and Malliaras model and yielded a time constant ( $\tau$ ) of 137  $\mu\text{s}$ .<sup>[56]</sup> The switching time of an OECT is limited by either the transport of holes in the channel, or the transport of ions into the film. The spike-and-recovery shape of the current response measured by the CPE-K-based OECT is indicative of a transient current that is dominated by hole extraction from the film.<sup>[56,57]</sup> The rapid response of the OECT is comparable to the times observed by PEDOT:PSS and demonstrates faster switching times than other accumulation mode materials in the literature.<sup>[58,24]</sup> CPE-K-based OECTs were tested at temperatures ranging from 10 °C to 80 °C in 5 °C increments to test their stability at these temperatures. To minimize the amount of drift observed due to evaporation of the gate electrolyte, devices were tested at maximum humidity in an environmental testing chamber. **Figure 3.6** shows stable transfer characteristics from 10 °C to 50 °C. A slight increase in current is observed due to phonon assisted hopping transport in CPE-K. Device performance steadily declines from 55 °C to 80 °C, at which point the CPE-K film completely dissolves

from the substrate. CPE-K OEETs are stable in temperature ranges relevant to biological systems, such as the human body (36.5-37.5 °C).<sup>[59]</sup>

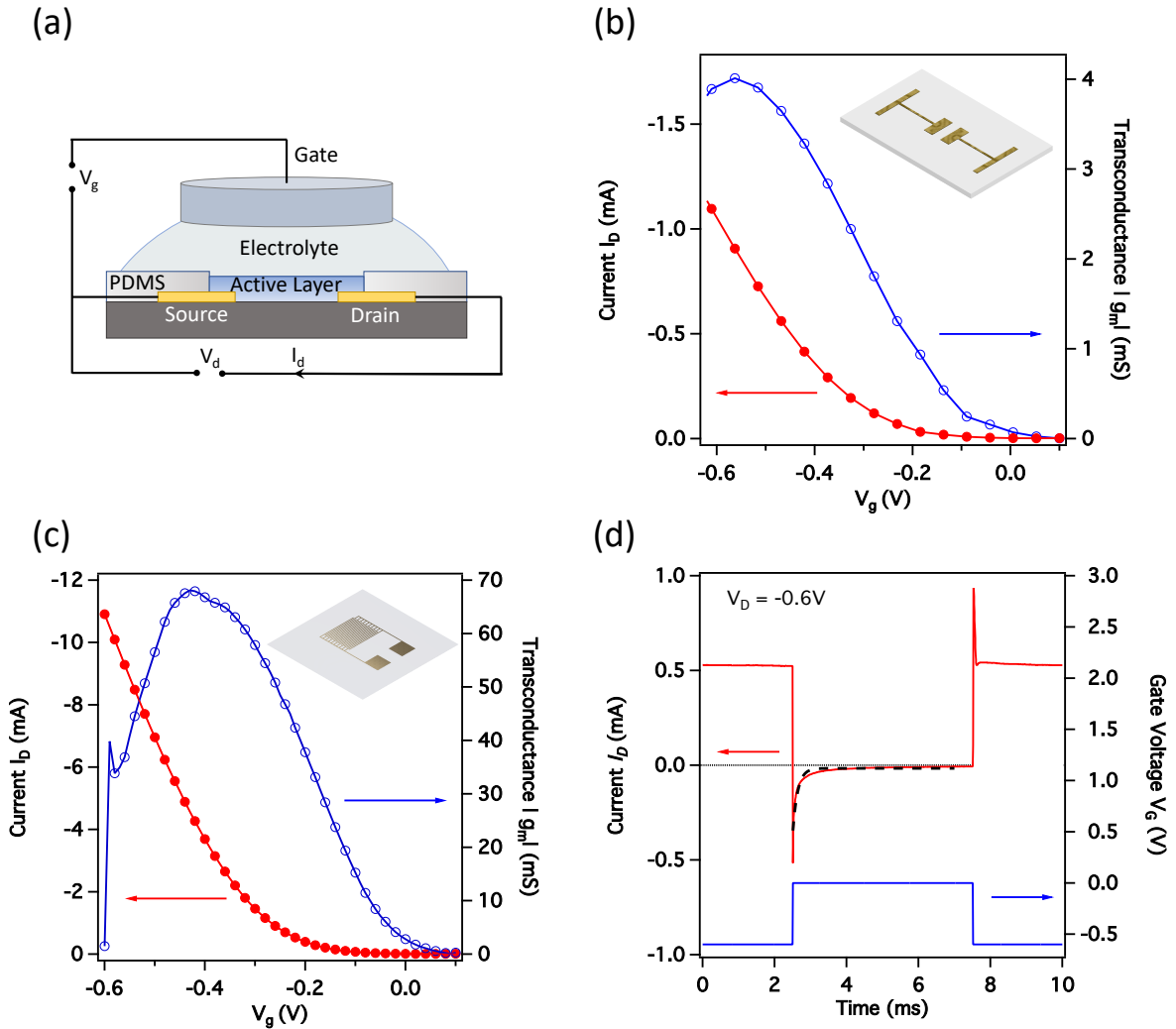


**Figure 3.4:** (a) Device architecture of CPE-K-based OEETs. Transfer characteristics and corresponding transconductance values at  $V_D = -0.6\text{V}$  of OEETs made using (b) regular contacts ( $W = 1000 \mu\text{m}$ ,  $L = 40 \mu\text{m}$ ,  $d = 0.6 \mu\text{m}$ ) and (c) interdigitated contacts ( $W = 27 \mu\text{m}$ ,  $L = 8 \mu\text{m}$ ,  $d = 3 \mu\text{m}$ ) (contact shape in figure insets). (d) Response time of a CPE-K-based OEET measured at 100 Hz and  $V_D = -0.6\text{V}$  ( $W = 1000 \mu\text{m}$ ,  $L = 40 \mu\text{m}$ ,  $d = 0.4 \mu\text{m}$ ). The black dotted line traces the exponential fit of the transistor switching to the OFF state and resulted in a  $\tau$  of 137  $\mu\text{s}$ .

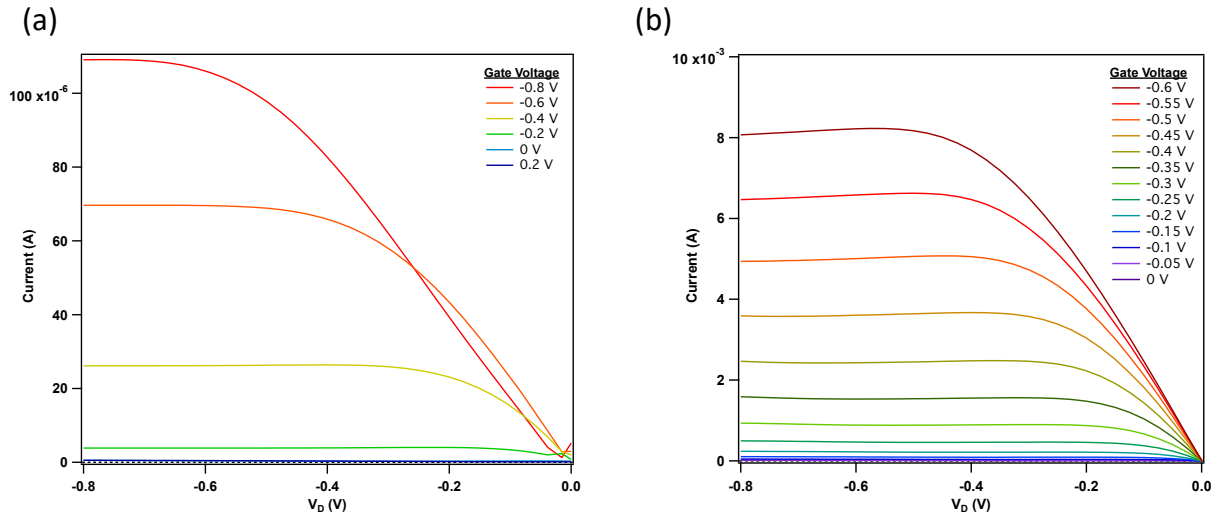


**Figure 3.5:** (a) Output characteristics of a CPE-K OECT made using standard (non-interdigitated) contacts. (b) Output characteristics of a CPE-K OECT made with interdigitated contacts.

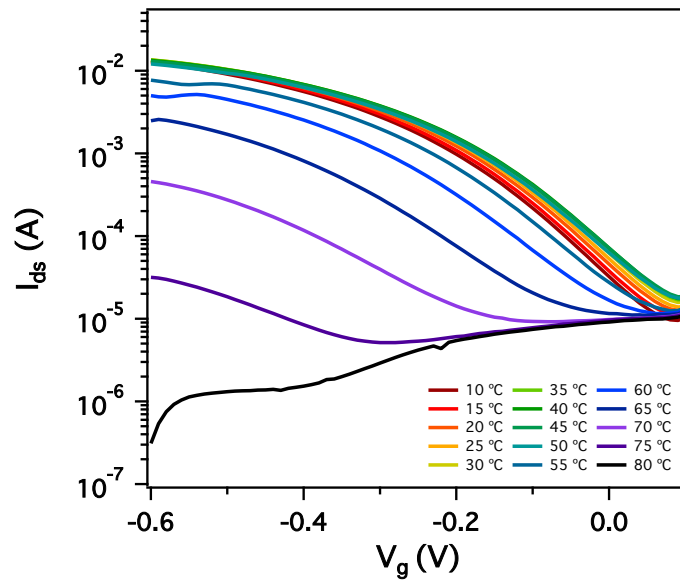


**Figure 3.6:** Transfer characteristics of a CPE-K OECT with interdigitated contacts measured from 10 °C to 80 °C in 5 °C intervals. Device performance remains stable up until 55°C, beyond which there is a rapid deterioration in the device performance.

### 3.6 Volumetric Capacitance Measurements and Transconductance Versus Film Thickness

One key difference between OEECTs and electrolyte-gate field-effect transistors (EGOFETs) is their capacitive behavior. In EGOFETs, doping occurs at the interface between the electrolyte and the active layer. In OEECTs, ions are injected into the bulk of the film, allowing for doping to occur throughout the entire film. Capacitive values can be orders of magnitude larger than EGOFETs of the same device dimensions, and result in the low-voltage operation that is characteristic of OEECTs.<sup>[60]</sup> The transconductance ( $g_m$ ) of an OEECT operated in the saturation regime is given by:

$$g_m = \left( W \cdot \frac{d}{L} \right) \cdot \mu \cdot C^* \cdot (V_T - V_G) \quad (3.1)$$

where  $W$  is the channel width,  $d$  is the film thickness of the active layer,  $L$  is the channel length,  $\mu$  is the hole mobility in the CPE-K channel,  $C^*$  is the volumetric capacitance of the CPE-K channel,  $V_T$  is a geometry-independent threshold voltage and  $V_G$  is the applied gate voltage. The equation is identical to the equation used to describe OFET transconductance, except that capacitance in OEECTs scales with film thickness. **Equation 3.1** shows that increasing  $C^*$  increases the transconductance of the OEECT. CPE-K is expected to exhibit volumetric capacitance due to its water-solubility. Sulfonate moieties of the side-chains of CPE-K allow for water and ions to penetrate and drift within the bulk of the film, allowing for bulk doping and de-doping of the film. Using impedance spectroscopy and gate transient measurement techniques, we can measure and compare the capacitance of CPE-K-based OEECTs to other OEECT materials reported in the literature. To perform these measurements, the source and drain contacts of OEECTs are shorted, making the CPE-K active layer the working electrode.

The capacitance of the OECT device is measured to be  $3.2 \times 10^{-6} \pm 9.7 \times 10^{-7}$  F, which is equal to  $1.34 \times 10^2$  F cm<sup>-3</sup> when adjusted for the volume of the active layer. This value fits well within the range observed for other mixed conductors reported in the literature.<sup>[28]</sup> The effect of doping or de-doping on the capacitance of the CPE-K active layer can be measured by applying a DC bias while collecting the impedance spectra (**Figure 3.7a**). The results correspond well with the transfer characteristics of CPE-K OECTs. Higher values measured for the capacitance correspond to the ionic-electronic coupling observed at low voltages when the film is in its doped state. When applying a positive bias (0.2 V), the film is in the non-conductive, reduced state. In this case, ions are unable to inject into the bulk of the film, and a relatively low capacitance value of  $6.2 \times 10^{-5}$  F/cm<sup>2</sup> related to the double-layer capacitance is measured. This value is close to the range of capacitance values from 1-10  $\mu$ F/cm<sup>2</sup> observed in OFETs gated with an electrolyte.<sup>[19]</sup> When a negative DC bias is applied during the impedance measurements, an increase of almost three orders of magnitude in the capacitance is observed. Under negative bias (-0.6 V), the film becomes oxidized and conductive. Ions are now in the bulk of the CPE-K active layer, and a corresponding capacitance of  $2.4 \times 10^{-2}$  F/cm<sup>2</sup> is measured. Such high capacitance per unit area is indicative of thickness dependent, volumetric capacitance, where charges are injected and drift through the bulk of the active layer. When measuring the capacitance of CPE-K films of varying thicknesses, higher capacitance is measured for thicker films under negative DC bias (**Figure 3.8**). A negligible difference in capacitance at various thicknesses is measured when applying a positive DC bias. This difference in behavior corresponds to thickness dependent, volumetric capacitance at negative bias and thickness independent, double-layer capacitance at positive bias. **Figure 3.7b** shows the gate transients of an OECT at various gate voltages. As with the impedance

spectroscopy measurements, the source and drain are shorted for this measurement as seen in the figure inset. The gate transient is measured by applying a gate bias of -0.6 V and recording the decay of the gate current ( $I_g$ ) as  $V_g$  is switched to 0 V. The ionic charge injected into the CPE-K film from the gate electrolyte is calculated by integration of the current decay curve. The ionic charge ( $Q$ ) injected into the film was calculated for 0.1 V increments from -0.8 V to -0.3 V applied gate bias. The slope of the linear fit of the  $Q$ - $V_g$ -plot gives a value of  $3.1 \times 10^2$  F/cm<sup>3</sup>; this value is close to the results calculated by impedance spectroscopy ( $1.3 \times 10^2$  F/cm<sup>3</sup>). **Figure 3.7c** demonstrates the effect of film thickness on the transfer characteristics of CPE-K-based OECTs which were fabricated using interdigitated contacts. The blue and red curves represent devices that contained active layers with a film thickness of approximately 300 nm and 2500 nm, respectively. As expected based on **Equation 3.1**, thicker films will result in a larger current due to the increase in capacitance of the OECT. **Figure 3.7d** shows the respective transconductance at each measured voltage for the thin and thick OECT devices. A peak transconductance of  $24.72 \pm 6.9$  mS and  $62.25 \pm 6.2$  mS was measured for the thin and thick active layers, respectively. From the results shown in this section, it is clear that CPE-K demonstrates volumetric capacitance. **Figure 3.9** is a plot of the peak transconductance of CPE-K based OECTs as a function of their device geometry and operating voltage. Plotting the data in such a manner allows CPE-K-based devices to be compared to other materials in the literature.<sup>[28,57,61]</sup> **Figure 3.9a** plots the transconductance versus the channel width-to-length ratio ( $WdL^{-1}$ ) of OECTs made from regular and interdigitated contacts. In comparison to OECTs made with regular contacts, the transconductance of OECTs made with interdigitated contacts do not increase as rapidly with an increase in the channel width-to-length ratio. This behavior is explained in of Liang *et al*, which suggests that this difference in

slope is due to the dominating influence of the source-drain series resistance ( $R_{sd}$ ) in short channel interdigitated electrodes.<sup>[55]</sup> **Figure 3.9b** compares CPE-K-based OECTs to other materials reported in the literature. We recommend the excellent communication by Inal *et al* which explains how to account for device geometry and operating conditions when comparing mixed organic conductors.<sup>[28]</sup> Without properly reporting device geometry and operating conditions, it is not possible to compare the transconductance of two materials used in OECTs in a meaningful way. CPE-K-based OECTs are comparable to OECTs fabricated from the CPE poly(6-(thiophene-3-yl)hexane-1-sulfonate) (PTHS).<sup>[21]</sup> CPE-K and PTHS represent the highest performing conjugated polyelectrolytes in the literature and rank among the best on the short list of OECT materials.<sup>[28,57]</sup>

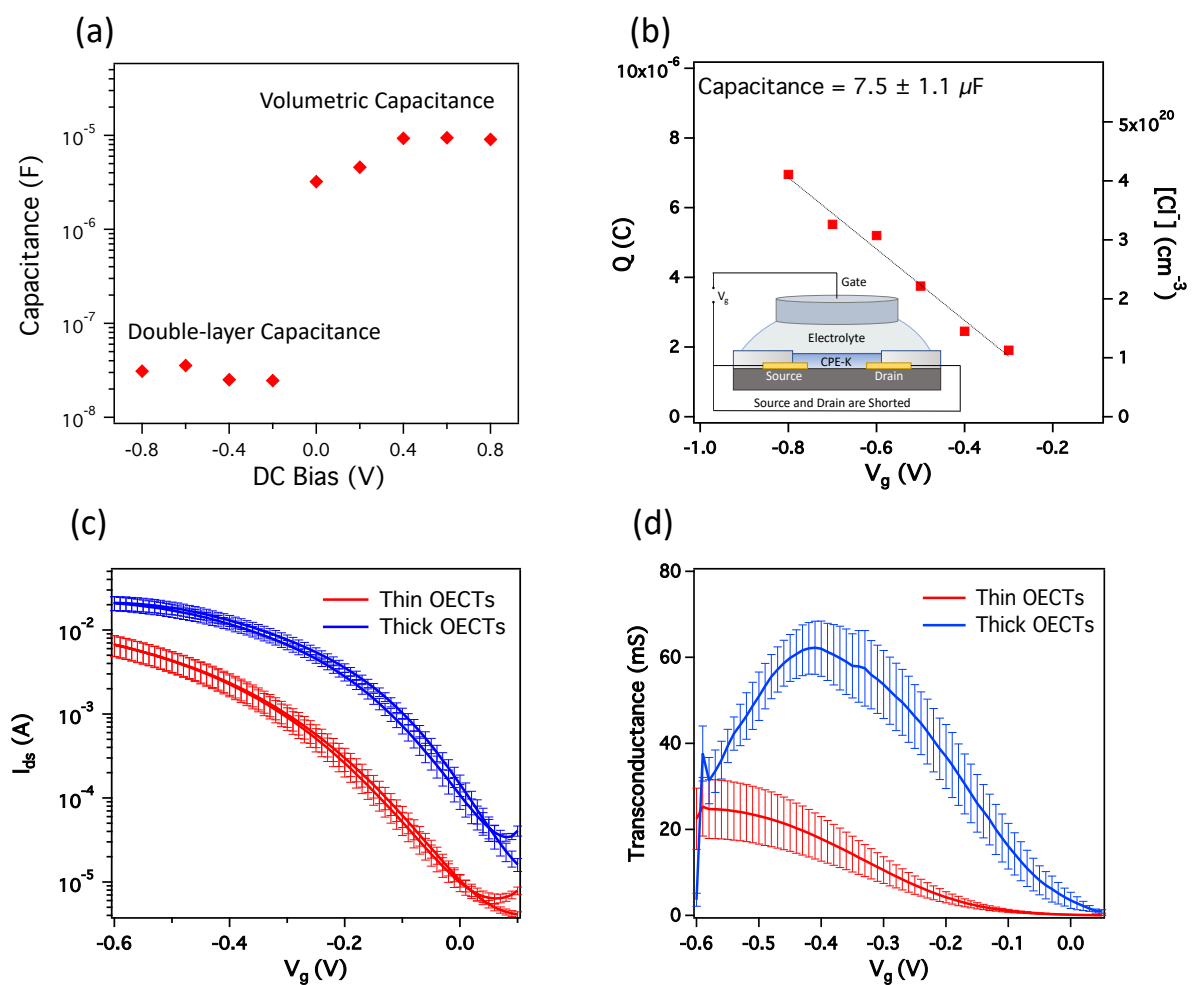


**Figure 3.7:** (a) Capacitance as a function of DC bias applied to the working electrode (CPE-K film) measured via impedance spectroscopy. (b) Capacitance of the same device measured via the gate transient method. (c) Transfer curves of OECTs made from thick (2500 nm) and thin (300 nm) CPE-K films and (d) their respective transconductance versus applied gate voltage.

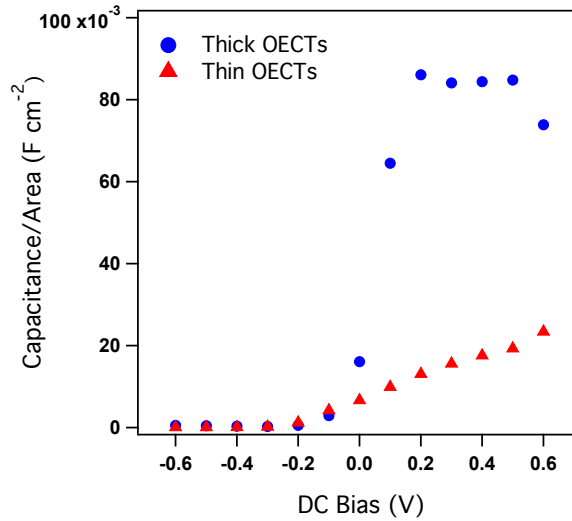


**Figure 3.8:** Capacitance per unit area as a function of DC bias measured by impedance spectroscopy of thick (blue circles) and thin (red triangles) OEETs.

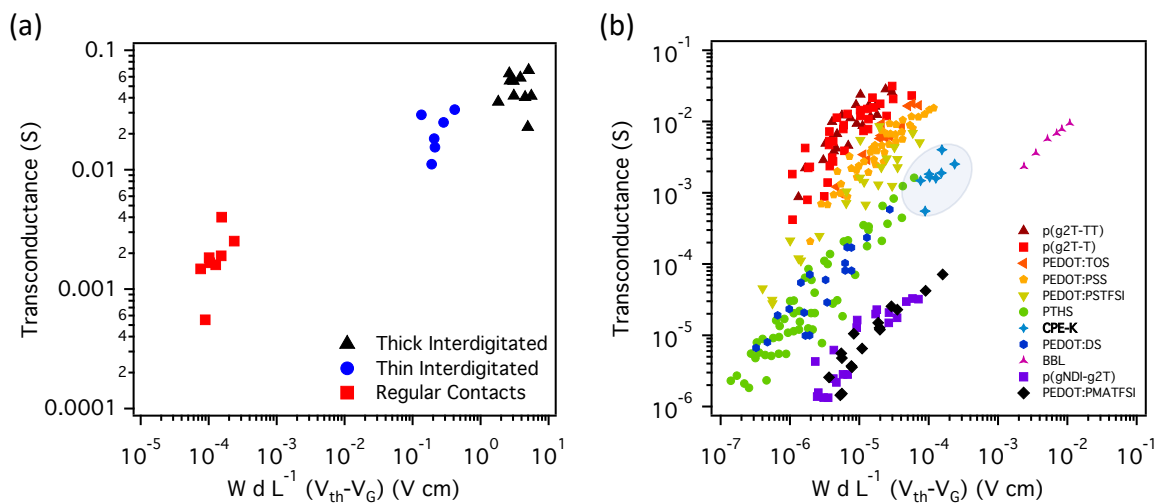


**Figure 3.9:** (a) Transconductance as a function of device geometry and voltage. Black triangles and blue circles represent CPE-K-based devices with interdigitated contacts. Red squares represent devices made with regular contacts. (b) Transconductance as a function of device geometry and voltage of OEET materials reported in the literature.<sup>[28,57,61]</sup>

### 3.7 Operational Mechanism of CPE-K OECTs

CPE-K is a self-doped conjugated polymer, in other words, the sulfonate moiety attached to the side-chain stabilizes the polaron on the conjugated backbone. As a result, a film of CPE-K conducts holes when a voltage is applied across the source and drain electrodes ( $V_{ds}$ ). An immediate drop in current is observed when a 0.1 M NaCl solution is deposited on the CPE-K channel of a two-terminal conductor (**Figure 3.10**). To test the hypothesis that the introduction of an electrolyte is responsible for reducing the conductivity of the CPE-K film, transfer curves of an OECT were measured with various concentrations of NaCl solutions on the channel (**Figure 3.11a**). When initially measuring the transfer curve with Milli-Q water on the channel, the device has a low on/off ratio of 31.4, and the device remains relatively conductive over all voltages. The on/off ratio gradually increases to a maximum of  $6.76 \times 10^3$  as the concentration of the NaCl solution is increased to 6 M. These results suggest that the salt is responsible for de-doping the film while operating the OECT. **Figure 3.12** presents the change in transconductance and on/off ratio at each salt concentration. There are two possible mechanisms for the increase in current and simultaneous formation of a polaron peak upon applying a negative gate voltage. Potassium ions may be extracted from the bulk of the CPE-K film in response to the application of a negative bias to the gate electrode. Following extraction of cations, uncompensated sulfonate groups are stabilized by polarons injected from the source electrode, resulting in an increase in current and formation of a polaron peak. An alternative mechanism involves injection of anions into the CPE-K film, which stabilize polarons on the CPE-K backbone. It is possible that the device operation involves a synergetic contribution of both proposed mechanisms. Further insight into the operational mechanism of

CPE-K-based OECTs was obtained through spectroelectrochemical measurements. The change in optical absorption as a function of applied bias was monitored to determine the electroactivity of CPE-K in the presence of an electrolyte.<sup>[62]</sup> OECT materials are able to transduce ionic to electronic signals by changing the redox state of the conjugated backbone when hydrated ions penetrate the bulk of the film. Spectroelectrochemistry monitors the oxidation and reduction of the bulk of the CPE-K film by tracking the evolution of the absorption profile with the CPE-K film biased at various voltages. A voltage ranging from 0.2 V to -0.6 V was applied between a CPE-K film on an ITO substrate and a Ag/AgCl electrode in a 0.1 M NaCl solution (**Figure 3.11b**). A gradual decrease in the absorption between 500 nm and 850 nm was observed as an increasingly negative potential is applied to the CPE-K film (**Figure 3.11c**). This absorption peak is attributed to the  $\pi$ - $\pi^*$  transition of the conjugated backbone. A simultaneous increase in the absorption between 850 nm and extending beyond 1200 nm is observed, indicating the formation of a polaron in the CPE-K film.<sup>[49]</sup> The isosbestic point around 850 nm is indicative of a conversion of the CPE-K backbone from a neutral to an oxidized species. A blue-shift from 700 nm to 650 nm of the absorption of the neutral species is observed as a negative voltage is applied to the CPE-K film. This could be due to the swelling of the film as water solvated ions enter the film and  $\pi$ - $\pi$  interactions are interrupted.<sup>[63,64]</sup> **Figure 3.11d** shows the change in the absorption at each wavelength of the UV-vis spectra relative to the absorption at 0 V. The isosbestic point and conversion from neutral to oxidized CPE-K film is clearly observed around 850 nm. The observed changes in the spectra support the results from impedance spectroscopy and gate transient measurements that doping occurs in the bulk of the film. If doping were to occur only at the interface of the electrolyte, only small changes to the spectrum would occur when

applying a bias.<sup>[24]</sup> The spectroelectrochemical experiment confirms that the redox state in the CPE-K OECT is controlled by the voltage applied to a gate electrode in the electrolyte. This behavior is consistent with the increase in current observed when applying a negative gate voltage to the OECT while measuring a transfer curve.

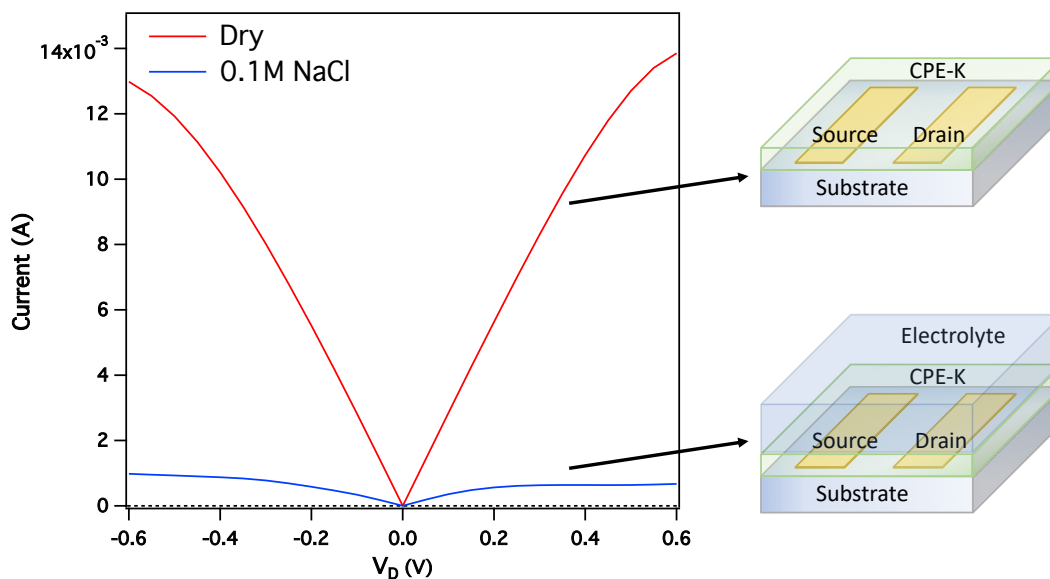


**Figure 3.10:** Current voltage plot of a CPE-K film two-terminal conductor before (red trace) and after (blue trace) depositing a 0.1M NaCl solution on the film. A reduction in current is observed when a 0.1 M NaCl solution is placed on CPE-K.

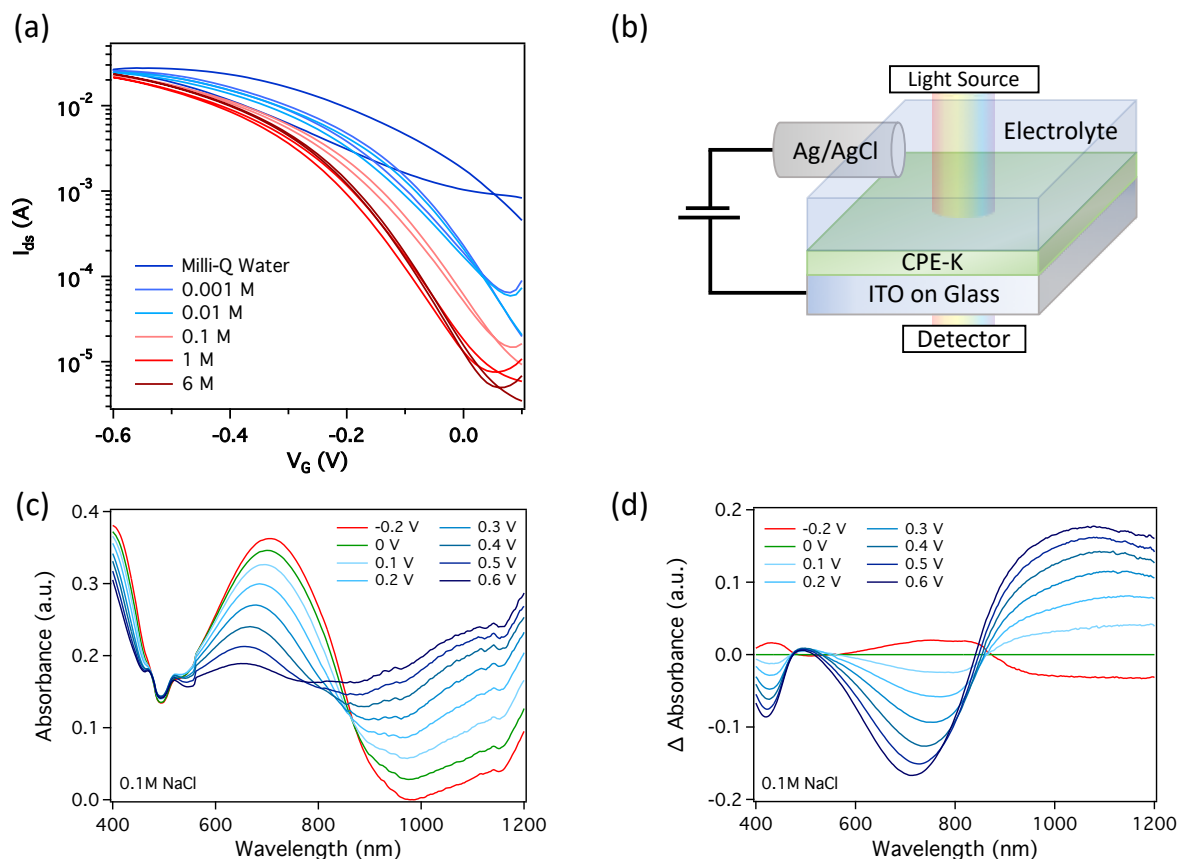


**Figure 3.11:** (a) Transfer curves as a function of NaCl concentration. A decrease in the “off current” at 0 V gate voltage is observed. (b) Experimental set-up of photoelectrochemical measurements. Substrate is placed in a quartz cuvette filled with a 0.1 M NaCl solution and the spectra is collected in a UV-Vis spectrophotometer. (c) UV-Vis spectra at various gate voltages applied to the film. (d) The change in the absorption at each wavelength of the UV-vis spectra relative to the absorption at 0 V.

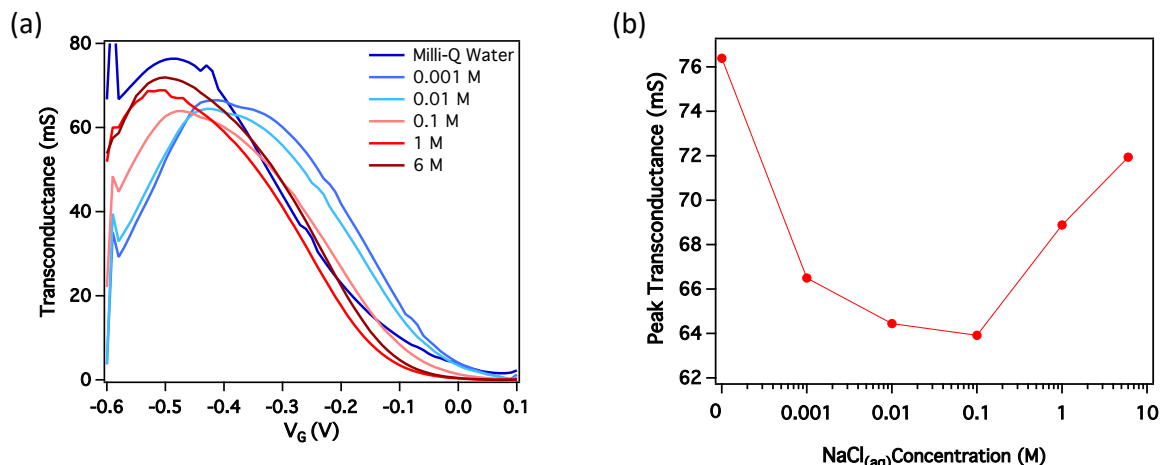


**Figure 3.12:** (a) Transconductance versus applied gate voltage at various salt concentrations. (b) Peak transconductance at various salt concentrations.

### 3.8 Conclusions

In conclusion, a self-doped CPE material was utilized to fabricate high transconductance accumulation mode OECTs. The direct cross-linking of GOPS to the sulfonate functional group on CPE-K was demonstrated by XPS. OECT devices fabricated with CPE-K exhibited accumulation mode operation which allows for low power consumption as the device is usually in the OFF state. The transconductance of OECTs made from CPE-K was compared to other OECT materials reported in the literature by considering device channel volume and operational voltage. In addition, CPE-K-based OECTs show rapid switching times and stability over the range of temperatures relevant for biological applications. A large increase in transconductance in a relatively small device area was observed when using interdigitated contacts due to the increase in channel width, making them good candidates for applications such as neural interfacing. The volumetric capacitance of CPE-K was demonstrated using impedance spectroscopy on films of varying thicknesses and the calculated

capacitance per square unit of CPE-K was confirmed with gate transient measurements. CPE-K demonstrates volumetric capacitance under an applied negative DC bias, which is consistent with the movement of ions made possible by their compensation from polarons in CPE-K. Spectroelectrochemistry was used to further explore the doping and de-doping of CPE-K films in an electrolyte solution under an applied bias. The appearance of a polaron peak is measured under an applied bias, which can be used to explain the increase in current measured in the corresponding transfer curves. The results highlight the potential of conjugated polyelectrolytes in OECTs and point towards future designs of CPEs for use in OECTs. A wide range of high mobility D-A conjugated backbones have been discovered by the OFET community, and can be adapted for use in OECTs by utilizing water soluble sidechains such as sulfonate functional groups. Water soluble sidechains are critical for allowing bulk doping of the film and allowing the device to operate as an OECT. CPE-K ranks among the highest performing materials for accumulation mode OECTs and represents a shift away from PEDOT:PSS towards a more widespread use of novel materials in organic electrochemical transistors.

### **3.9 Experimental Methods**

*CPE-K Preparation:* PCPDTBT-SO<sub>3</sub>K (CPE-K) is an anionic narrow-band-gap conjugated polyelectrolyte with a  $\pi$ -conjugated cyclopenta[2,1-b;3,4-b]-dithiophene-alt-4,7-(2,1,3-benzothiazodiazole) (CPDT-alt-BT) backbone. The material was synthesized via Suzuki-Miyaura polymerization reactions outlined in the literature.<sup>[65]</sup>

*OECT Fabrication:* Gold electrodes were patterned on glass wafers using standard clean-room lithography protocols. PDMS wells were used to contain the electrolyte and insulate the gold

contacts from the electrolyte. PDMS was prepared from Sylgard® 184 from Dow-Corning using a mixing ratio of 10:1 between the base and the curing agent with a curing time of 4 hours at 80 °C. Wells were cut from a sheet of PDMS and fused to the patterned glass substrates using an oxygen plasma.

*Electrical Characterization:* Electrical measurements were made using a Keithley semiconductor parametric analyzer (model 4200-SCS) and the switching speed was measured using a Teledyne Lecroy Waveace 2034 oscilloscope and a function generator.

*AFM Characterization:* All topographic images were obtained using an Asylum MFP-3D mounted atop an Olympus inverted optical microscope under and inert atmosphere. Silicon tips with a resonant frequency of 300 kHz and a force constant of 40 N/m were used (Budget Sensors). First order image flattening was performed on the morphology images on Asylum Research AFM software version 14, programmed using IGOR Pro.

*Dielectric Characterization:* The capacitance of CPE-K films was measured using a Solartron SI 1260A impedance analyzer. Gate transient measurements were performed using a Teledyne Lecroy Waveace 2034 oscilloscope and a function generator.

*X-ray Photoelectron Spectroscopy (XPS):* All x-ray photoelectron spectroscopy measurements were obtained on a Kratos Axis Ultra DLD XPS under vacuum ( $10^{-8}$  Torr) using monochromatic x-rays produced using an aluminum source running at a potential of 14 kV. A pass energy of 20 was used for all high-res element sweeps. The CPE-K samples were spun-cast onto cleaned conductive indium tin oxide/glass substrates. The films were mounted onto a sample bar using double-sided tape, and electrically grounded to the sample bar using nickel impregnated tape. Peak fitting was performed using the software WINSPEC.

*UV-vis-nIR and Spectroelectrochemistry:* All UV-vis-nIR spectra were obtained using a Perkin-Elmer Lambda 750 UV-vis-nIR spectrometer using a tungsten lamp for the visible to near-IR region and a deuterium lamp for the UV region. A 100% transmission blank was obtained using a clean indium tin oxide/glass substrate for all spectra. CPE-K films for spectroelectrochemistry were prepared by drop-casting a CPE-K and GOPS cross-linker solution on to a cleaned ITO-coated glass substrate. A wire was soldered to the edge of the ITO substrate and the contact point was covered with epoxy to limit leakage current. The CPE-K film and a Ag/AgCl electrode were placed in a cuvette filled with a 0.1 M NaCl solution. A constant bias was applied using a DC power source.

*Temperature Dependent Electrical Characterization:* Transfer curves were measured in a temperature and humidity controlled environmental chamber. Humidity was kept at a maximum level to keep the electrolyte from evaporating while measuring from 10 °C to 80 °C in 5 °C intervals.

### 3.10 References

1. J. Rivnay, R. M. Owens, G. G. Malliaras, *Chem. Mater.* **2014**, *26*, 679.
2. T. Someya, Z. Bao, G. G. Malliaras, *Nature* **2016**, *540*, 379.
3. D. Khodagholy, V. F. Curto, K. J. Fraser, M. Gurfinkel, R. Byrne, D. Diamond, G. G. Malliaras, F. Benito-Lopez, R. M. Owens, *J. Mater. Chem.* **2012**, *22*, 4440.
4. M. Braendlein, A.-M. Pappa, M. Ferro, A. Lopresti, C. Acquaviva, E. Mamessier, G. G. Malliaras, R. M. Owens, *Adv. Mater.* **2017**, *29*, 1605744.
5. E. Macchia, P. Romele, K. Manoli, M. Ghittorelli, M. Magliulo, Z. M. Kovács-Vajna, F. Torricelli, L. Torsi, *Flex. Print. Electron.* **2018**, *3*, 034002.
6. A. M. Pappa, D. Ohayon, A. Giovannitti, I. P. Maria, A. Savva, I. Uguz, J. Rivnay, I. McCulloch, R. M. Owens, S. Inal, *Sci. Adv.* **2018**, *4*, eaat0911.

7. O. Parlak, S. T. Keene, A. Marais, V. F. Curto, A. Salleo, *Sci. Adv.* **2018**, *4*, eaar2904.
8. J. Borges-González, C. J. Kousseff, C. B. Nielsen, *J. Mater. Chem. C* **2019**, *7*, 1111.
9. C. Diacci, J. W. Lee, P. Janson, G. Dufil, G. Méhes, M. Berggren, D. T. Simon, E. Stavrinidou, *Adv. Mater. Technol.* **2019**, *0*, 1900262.
10. N. Wang, A. Yang, Y. Fu, Y. Li, F. Yan, *Acc. Chem. Res.* **2019**, *52*, 277.
11. S. Wustoni, C. Combe, D. Ohayon, M. H. Akhtar, I. McCulloch, S. Inal, *Adv. Funct. Mater.* **2019**, *0*, 1904403.
12. G. Scheiblin, R. Coppard, R. M. Owens, P. Mailley, G. G. Malliaras, *Adv. Mater. Technol.* **2017**, *2*, 1600141.
13. Y. J. Jo, K. Y. Kwon, Z. U. Khan, X. Crispin, T. Kim, *ACS Appl. Mater. Interfaces* **2018**, *10*, 39083.
14. D. Khodagholy, T. Doublet, P. Quilichini, M. Gurfinkel, P. Leleux, A. Ghestem, E. Ismailova, T. Hervé, S. Sanaur, C. Bernard, G. G. Malliaras, *Nat. Commun.* **2013**, *4*, 1575.
15. D. Khodagholy, J. N. Gelinas, T. Thesen, W. Doyle, O. Devinsky, G. G. Malliaras, G. Buzsáki, *Nat. Neurosci.* **2015**, *18*, 310.
16. D. Khodagholy, J. N. Gelinas, Z. Zhao, M. Yeh, M. Long, J. D. Greenlee, W. Doyle, O. Devinsky, G. Buzsáki, *Sci. Adv.* **2016**, *2*, e1601027.
17. J. Rivnay, H. Wang, L. Fenno, K. Deisseroth, G. G. Malliaras, *Sci. Adv.* **2017**, *3*, e1601649.
18. H. S. White, G. P. Kittlesen, M. S. Wrighton, *J. Am. Chem. Soc.* **1984**, *106*, 5375.
19. J. Rivnay, S. Inal, A. Salleo, R. M. Owens, M. Berggren, G. G. Malliaras, *Nat. Rev. Mater.* **2018**, *3*, 17086.
20. C. Duc, G. G. Malliaras, V. Senez, A. Vlandas, *Synth. Met.* **2018**, *238*, 14.
21. S. Inal, J. Rivnay, P. Leleux, M. Ferro, M. Ramuz, J. C. Brendel, M. M. Schmidt, M. Thelakkat, G. G. Malliaras, *Adv. Mater.* **2014**, *26*, 7450.
22. D. G. Harman, R. Gorkin, L. Stevens, B. Thompson, K. Wagner, B. Weng, J. H. Y. Chung, M. in het Panhuis, G. G. Wallace, *Acta Biomater.* **2015**, *14*, 33.
23. E. Zeglio, M. Vagin, C. Musumeci, F. N. Ajjan, R. Gabrielsson, X. T. Trinh, N. T. Son, A. Maziz, N. Solin, O. Inganäs, *Chem. Mater.* **2015**, *27*, 6385.

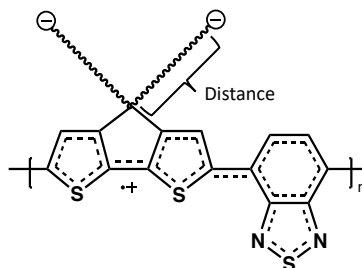
24. A. Giovannitti, D.-T. Sbircea, S. Inal, C. B. Nielsen, E. Bandiello, D. A. Hanifi, M. Sessolo, G. G. Malliaras, I. McCulloch, J. Rivnay, *Proc. Natl. Acad. Sci.* **2016**, *113*, 12017.
25. A. Giovannitti, C. B. Nielsen, D.-T. Sbircea, S. Inal, M. Donahue, M. R. Niazi, D. A. Hanifi, A. Amassian, G. G. Malliaras, J. Rivnay, I. McCulloch, *Nat. Commun.* **2016**, *7*, 13066.
26. S. Inal, J. Rivnay, A. I. Hofmann, I. Uguz, M. Mumtaz, D. Katsigiannopoulos, C. Brochon, E. Cloutet, G. Hadziioannou, G. G. Malliaras, *J. Polym. Sci. Part B Polym. Phys.* **2016**, *54*, 147.
27. C. B. Nielsen, A. Giovannitti, D.-T. Sbircea, E. Bandiello, M. R. Niazi, D. A. Hanifi, M. Sessolo, A. Amassian, G. G. Malliaras, J. Rivnay, I. McCulloch, *J. Am. Chem. Soc.* **2016**, *138*, 10252.
28. S. Inal, G. G. Malliaras, J. Rivnay, *Nat. Commun.* **2017**, *8*, 1767.
29. A. Giovannitti, I. P. Maria, D. Hanifi, M. J. Donahue, D. Bryant, K. J. Barth, B. E. Makdah, A. Savva, D. Moia, M. Zetek, P. R. F. Barnes, O. G. Reid, S. Inal, G. Rumbles, G. G. Malliaras, J. Nelson, J. Rivnay, I. McCulloch, *Chem. Mater.* **2018**, *30*, 2945.
30. S. Inal, J. Rivnay, A.-O. Suiu, G. G. Malliaras, I. McCulloch, *Acc. Chem. Res.* **2018**, *51*, 1368.
31. M. M. Schmidt, M. ElMahmoudy, G. G. Malliaras, S. Inal, M. Thelakktat, *Macromol. Chem. Phys.* **2018**, *219*, 1700374.
32. E. Zeglio, O. Inganäs, *Adv. Mater.* **2018**, *30*, 1800941.
33. M. Moser, J. F. Ponder, A. Wadsworth, A. Giovannitti, I. McCulloch, *Adv. Funct. Mater.* **2019**, *29*, 1807033.
34. E. Zeglio, A. L. Rutz, T. E. Winkler, G. G. Malliaras, A. Herland, *Adv. Mater.* **2019**, *31*, 1806712.
35. B. D. Paulsen, K. Tybrandt, E. Stavrinidou, J. Rivnay, *Nat. Mater.* **2019**, *1*.
36. B. Liu, G. C. Bazan, *Chem. Mater.* **2004**, *16*, 4467.
37. C.-K. Mai, B. Russ, S. L. Fronk, N. Hu, M. B. Chan-Park, J. J. Urban, R. A. Segalman, M. L. Chabinye, G. C. Bazan, *Energy Environ. Sci.* **2015**, *8*, 2341.

38. V. V. Brus, M. A. Gluba, C.-K. Mai, S. L. Fronk, J. Rappich, N. H. Nickel, G. C. Bazan, *Adv. Electron. Mater.* **2017**, *3*, 1600515.
39. P. Taranekar, Q. Qiao, H. Jiang, I. Ghiviriga, K. S. Schanze, J. R. Reynolds, *J. Am. Chem. Soc.* **2007**, *129*, 8958.
40. J. H. Seo, E. B. Namdas, A. Gutacker, A. J. Heeger, G. C. Bazan, *Adv. Funct. Mater.* **2011**, *21*, 3794.
41. J. H. Seo, A. Gutacker, B. Walker, S. Cho, A. Garcia, R. Yang, T.-Q. Nguyen, A. J. Heeger, G. C. Bazan, *J. Am. Chem. Soc.* **2009**, *131*, 18220.
42. S.-I. Na, T.-S. Kim, S.-H. Oh, J. Kim, S.-S. Kim, D.-Y. Kim, *Appl. Phys. Lett.* **2010**, *97*, 223305.
43. P. Schmode, D. Ohayon, P. M. Reichstein, A. Savva, S. Inal, M. Thelakkat, *Chem. Mater.* **2019**, *31*, 5286.
44. H. N. Tsao, D. M. Cho, I. Park, M. R. Hansen, A. Mavrinskiy, D. Y. Yoon, R. Graf, W. Pisula, H. W. Spiess, K. Müllen, *J. Am. Chem. Soc.* **2011**, *133*, 2605.
45. L. Ying, B. B. Y. Hsu, H. Zhan, G. C. Welch, P. Zalar, L. A. Perez, E. J. Kramer, T.-Q. Nguyen, A. J. Heeger, W.-Y. Wong, G. C. Bazan, *J. Am. Chem. Soc.* **2011**, *133*, 18538.
46. M. Wang, M. J. Ford, A. T. Lill, H. Phan, T.-Q. Nguyen, G. C. Bazan, *Adv. Mater.* **2017**, *29*, 1603830.
47. H. Zhou, Y. Zhang, C.-K. Mai, S. D. Collins, T.-Q. Nguyen, G. C. Bazan, A. J. Heeger, *Adv. Mater.* **2014**, *26*, 780.
48. C.-K. Mai, T. Arai, X. Liu, S. L. Fronk, G. M. Su, R. A. Segalman, M. L. Chabiny, G. C. Bazan, *Chem. Commun.* **2015**, *51*, 17607.
49. C.-K. Mai, H. Zhou, Y. Zhang, Z. B. Henson, T.-Q. Nguyen, A. J. Heeger, G. C. Bazan, *Angew. Chem. Int. Ed.* **2013**, *52*, 12874.
50. R. Niepelt, U. C. Schröder, J. Sommerfeld, I. Slowik, B. Rudolph, R. Möller, B. Seise, A. Csaki, W. Fritzsche, C. Ronning, *Nanoscale Res. Lett.* **2011**, *6*, 511.
51. A. Håkansson, S. Han, S. Wang, J. Lu, S. Braun, M. Fahlman, M. Berggren, X. Crispin, S. Fabiano, *J. Polym. Sci. Part B Polym. Phys.* **2017**, *55*, 814.
52. G. Zotti, S. Zecchin, G. Schiavon, F. Louwet, L. Groenendaal, X. Crispin, W. Osikowicz, W. Salaneck, M. Fahlman, *Macromolecules* **2003**, *36*, 3337.

53. O. Bubnova, Z. U. Khan, A. Malti, S. Braun, M. Fahlman, M. Berggren, X. Crispin, *Nat. Mater.* **2011**, *10*, 429.
54. U. Aygül, H. Peisert, J. Frisch, A. Vollmer, N. Koch, T. Chassé, *ChemPhysChem* **2011**, *12*, 2345.
55. Y. Liang, F. Brings, V. Maybeck, S. Ingebrandt, B. Wolfrum, A. Pich, A. Offenhäusser, D. Mayer, *Adv. Funct. Mater.* **2019**, *29*, 1902085.
56. D. A. Bernards, G. G. Malliaras, *Adv. Funct. Mater.* **2007**, *17*, 3538.
57. J. T. Friedlein, R. R. McLeod, J. Rivnay, *Org. Electron.* **2018**, *63*, 398.
58. D. Khodagholy, J. Rivnay, M. Sessolo, M. Gurfinkel, P. Leleux, L. H. Jimison, E. Stavrinidou, T. Herve, S. Sanaur, R. M. Owens, G. G. Malliaras, *Nat. Commun.* **2013**, *4*, ncomms3133.
59. I. I. Geneva, B. Cuzzo, T. Fazili, W. Javaid, *Open Forum Infect. Dis.* **2019**, *6*, ofz032.
60. J. Rivnay, P. Leleux, M. Ferro, M. Sessolo, A. Williamson, D. A. Koutsouras, D. Khodagholy, M. Ramuz, X. Strakosas, R. M. Owens, C. Benar, J.-M. Badier, C. Bernard, G. G. Malliaras, *Sci. Adv.* **2015**, *1*, e1400251.
61. H. Sun, M. Vagin, S. Wang, X. Crispin, R. Forchheimer, M. Berggren, S. Fabiano, *Adv. Mater.* **2018**, *30*, 1704916.
62. C. Enengl, S. Enengl, S. Pluczyk, M. Havlicek, M. Lapkowski, H. Neugebauer, E. Ehrenfreund, *ChemPhysChem* **2016**, *17*, 3836.
63. L. Q. Flagg, C. G. Bischak, J. W. Onorato, R. B. Rashid, C. K. Luscombe, D. S. Ginger, *J. Am. Chem. Soc.* **2019**, *141*, 4345.
64. A. Savva, C. Cendra, A. Giugni, B. Torre, J. Surgailis, D. Ohayon, A. Giovannitti, I. McCulloch, E. Di Fabrizio, A. Salleo, J. Rivnay, S. Inal, *Chem. Mater.* **2019**, *31*, 927.
65. C.-K. Mai, R. A. Schlitz, G. M. Su, D. Spitzer, X. Wang, S. L. Fronk, D. G. Cahill, M. L. Chabynyc, G. C. Bazan, *J. Am. Chem. Soc.* **2014**, *136*, 13478.

## Chapter 4:

### Side-chain Engineering of Self-doped Conjugated Polyelectrolytes for OECT Fabrication



#### 4.1 Introduction and Motivation

Bioelectronics is a field that emerged in the last decades devoted to transducing signals across biotic/abiotic interfaces. While biological systems rely mainly on ions and molecules as a signaling path, electronics around us use almost exclusively electrons as the dominant charge carriers.<sup>31</sup> Conjugated polymers can become conductors via the doping process<sup>32</sup>, and due to the prevalence of weak intermolecular van der Waals interactions, they are considered “soft” materials.<sup>33</sup> These properties become advantageous to transduce signals across biological interfaces.

Conjugated polyelectrolytes (CPEs) are a versatile class of conjugated polymers. CPEs are defined by a molecular framework that contains an electronically delocalized backbone and pendant ionic groups. This chemical moiety gives CPEs the optical and charge transport properties of organic semiconductors, while the ionic functionalities render CPEs soluble in water. The charged side groups allow for the incorporation of water molecules and mobile ions into the polymer matrix, enabling both electronic and ionic transport. CPEs, therefore can

bridge the gap between electronics and biology, allowing the development of intimate bioelectronic interfaces.<sup>34</sup> In addition, the charges on the polymer chains generated by electrochemical doping can be stabilized by their ionic groups in the side chains, yielding the so-called “self-doped” CPEs.<sup>35</sup> CPEs are functional for a variety of applications, including as interfacial layers in optoelectronic devices, bioimaging, bioelectric current generation enhancement,<sup>36</sup> bioelectric current storage (capacitive properties),<sup>37</sup> photothermal killing of bacteria,<sup>38</sup> antibiotic properties, and most recently, in organic electrochemical transistors (OECTs).<sup>39,40,41,42</sup>

Organic electrochemical transistors have been actively researched for bioelectronic applications. Reports demonstrate use for *in vivo* neural recording and modulation,<sup>43,44,45,46</sup> pH-sensing,<sup>47,48</sup> miniaturized biosensors for analyte detection.<sup>49,50,51,52,53,54,55,56,57</sup> The low operational voltage of OECTs and compatibility with aqueous environment make them useful for biological applications.<sup>58</sup> An OECT consists of an organic semiconductor film (active layer) between two metal electrodes (the source and the drain). On top of the active layer is the electrolyte, where an electrode (gate) is immersed.<sup>59</sup> The electrolyte is on top and in direct contact with the active layer. An electrochemical potential (i.e., Ag/AgCl gate electrode, nerve impulse) can drive ions from the electrolyte into or out of the conductive layer. The injected ions will change the doping state and, therefore, the conductivity of the active layer. Thereby, ionic signals are transduced into electronic signals.<sup>60</sup>

Few studies have introduced a structure-property relationship analysis on the design of conjugated polymers for OECTs applications.<sup>61</sup> In this work, a structure-property relationship study on derivatives of a self-doped conjugated polyelectrolyte composed of cyclopentadithiophene-alt-benzothiadiazole backbone containing a pendant negatively

charged sulfonate group is presented. A series of copolymers with increasing alkyl chain distances (2-5 methylene units) were synthesized by Luana Llanes of the lab of Professor Guillermo Bazan (**Figure 4.1**). Organic electrochemical transistors were built with each CPE as the active layer, and electrochemical impedance spectroscopy (EIS) was utilized to understand the differences in performance. Optical, electrochemical, and morphological properties were characterized and used to understand how the alkyl chain length variation modulates the properties of OECTs. Finally, a theoretical approach was used to further understand each CPE's different properties. This work is a first step in the comprehensive analysis of D–A copolymer CPE materials for next-generation high-performance OECTs. We aim to help establish molecular design criteria and elucidate important structure-property relations to synthesize high-performing semiconducting conjugated polyelectrolytes for OECT applications.

The synthesis of CPE-C4-Na and CPE-C3-Na has been previously reported.<sup>62,63</sup> The synthesis of all four CPE materials, shown in **Figure 4.1**, was performed by Luana Llanes in the lab of Professor Guillermo Bazan. The synthetic pathway begins with alkylation of commercially available cyclopentadithiophene (CPDT) with 1,4-butanedisulfone or 1,3-propanedisulfone under basic conditions, followed by bromination using N-bromosuccinimide (NBS). CPE-C2-Na and CPE-C5-Na are novel conjugated polyelectrolytes.

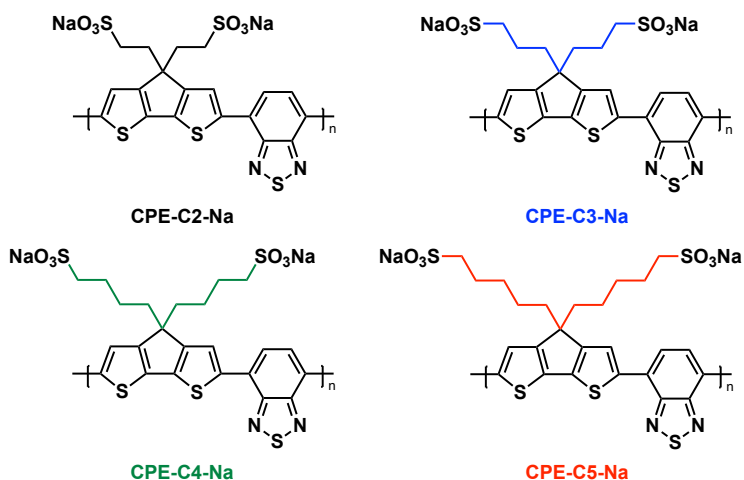


**Figure 4.1.** Chemical structures of CPE materials with varying side-chain lengths used in this study

## 4.2 Organic Electrochemical Transistors (OECT) Characterization

OECTs devices were fabricated using the four conjugated polyelectrolytes as the active layer. **Figure 4.2a** contains the general device architecture for OECTs fabricated for this study. A 0.1 M solution of NaCl was used as the gate electrolyte and an Ag/AgCl pellet as the gate electrode. To test the derivatives of CPEs as active layers, the films were first stabilized with a cross-linker. The operation of OECTs generally involves an electrolytic solution over the device channel, and the CPEs derivatives in this study dissolve quickly if the film is not previously stabilized. CPE solutions were prepared with (3-glycidyloxypropyl)trimethoxysilane (GOPS), a molecule used in a recently published paper in our group to stabilize CPE-K.<sup>39</sup> GOPS has also been used to stabilize PEDOT:PSS films in OECTs and to immobilize DNA on metal oxide surfaces.<sup>66,67</sup> X-ray photoelectron spectroscopy has been used to probe the stabilization mechanism of CPE-C4-K (CPE-K). It is hypothesized that the stabilization occurs via a nucleophilic attack of the sulfonate group in the side-chain to the electrophilic carbon center at epoxide, making the CPE insoluble in

water.<sup>39</sup> Considering that the anionic sulfonate group can stabilize the polaron (radical positive charge) on the backbone, a reduction in conductivity is expected as the sulfonate group reacts with the GOPS cross-linker. The simultaneous decrease in conductivity with increasing cross-linker added to the CPE-K solution has been observed.<sup>39</sup> Each CPE in our study indeed was tested with varying amounts of GOPS to achieve a balance between film stability and conductivity. The optimal percentage of GOPs in terms of film stability and conductivity is displayed in **Table 4.1**.

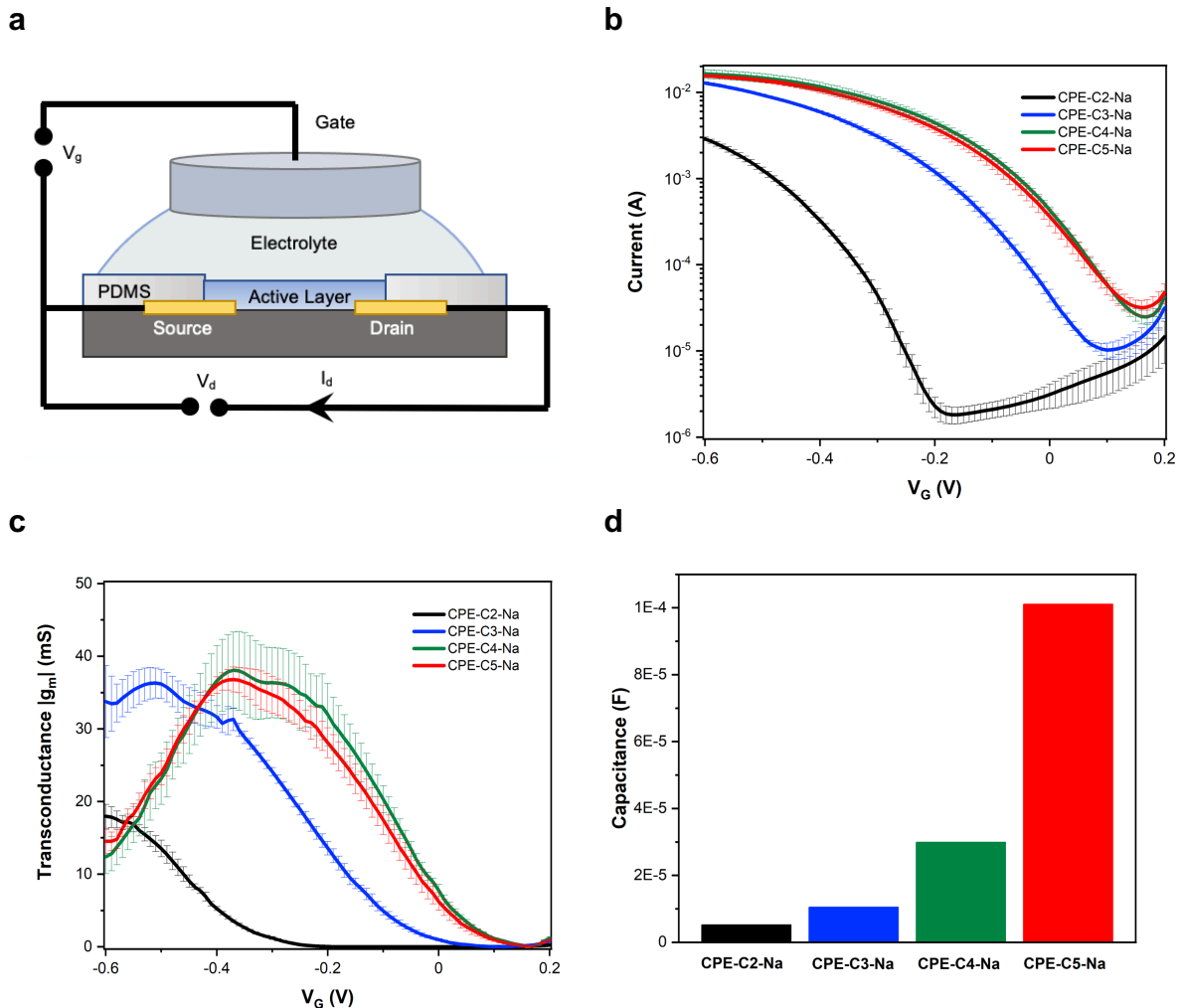


**Figure 4.2.** a) Device architecture of CPE-based OEETs; b) Transfer characteristics at  $V_D = -0.6$  V of OEETs made using interdigitated contacts ( $W = 27$   $\mu\text{m}$ ,  $L = 8$   $\mu\text{m}$ ,  $d = 3$   $\mu\text{m}$ ); c) Transconductance values at  $V_D = -0.6$  V of OEETs made using regular contacts. d) Volumetric capacitance.

CPE	GOPS (%weight)
CPE-C2-Na	32
CPE-C3-Na	32
CPE-C4-Na	32
CPE-C5-Na	16

**Table 4.1.** Weight percent of GOPS crosslinker used in the active layer for OECT device fabrication.

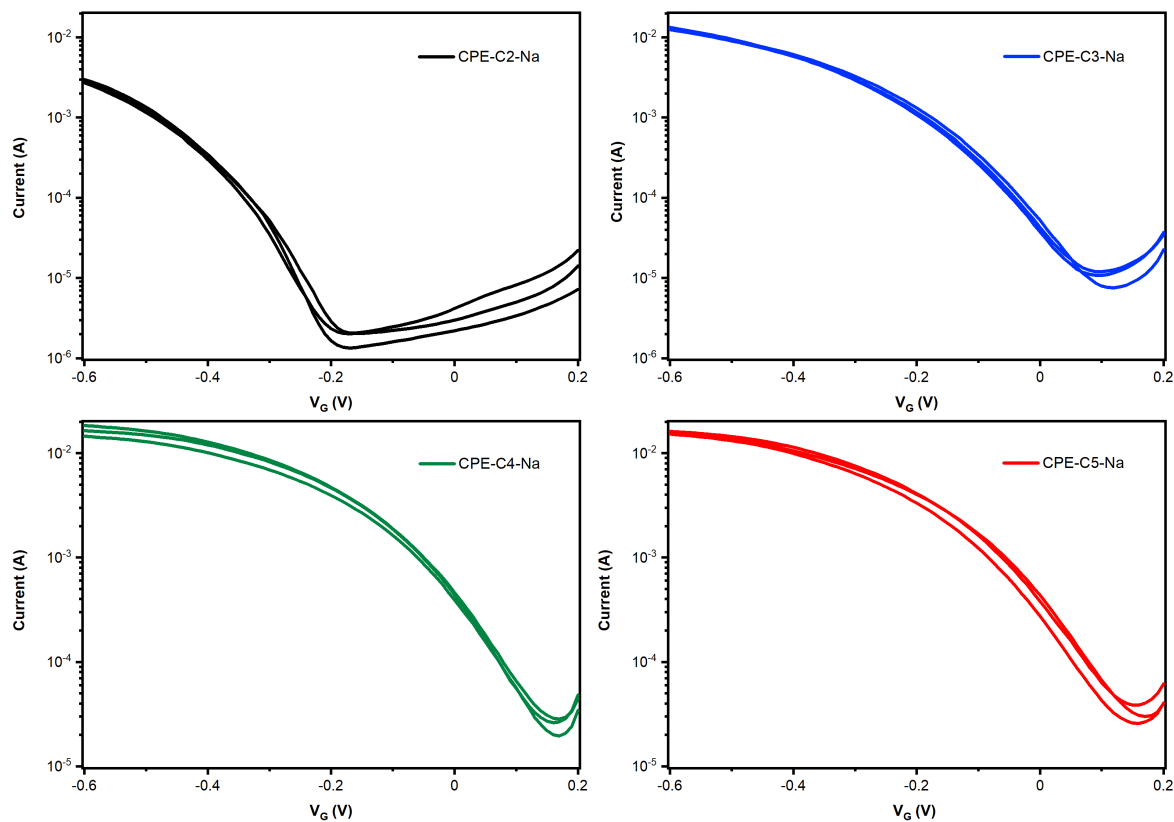


**Figure 4.3.** a) Transfer characteristics of all CPE-CX-Na Organic Electrochemical Transistors (OECTs) with optimized amounts of GOPS cross-linker. Each plot contains the transfer curve of three devices. CPE-2-Na, CPE-3-Na and CPE-4-Na OECTs are prepared with 32% GOPS by weight. CPE-5-Na OECTs are prepared with 16% GOPS by weight.

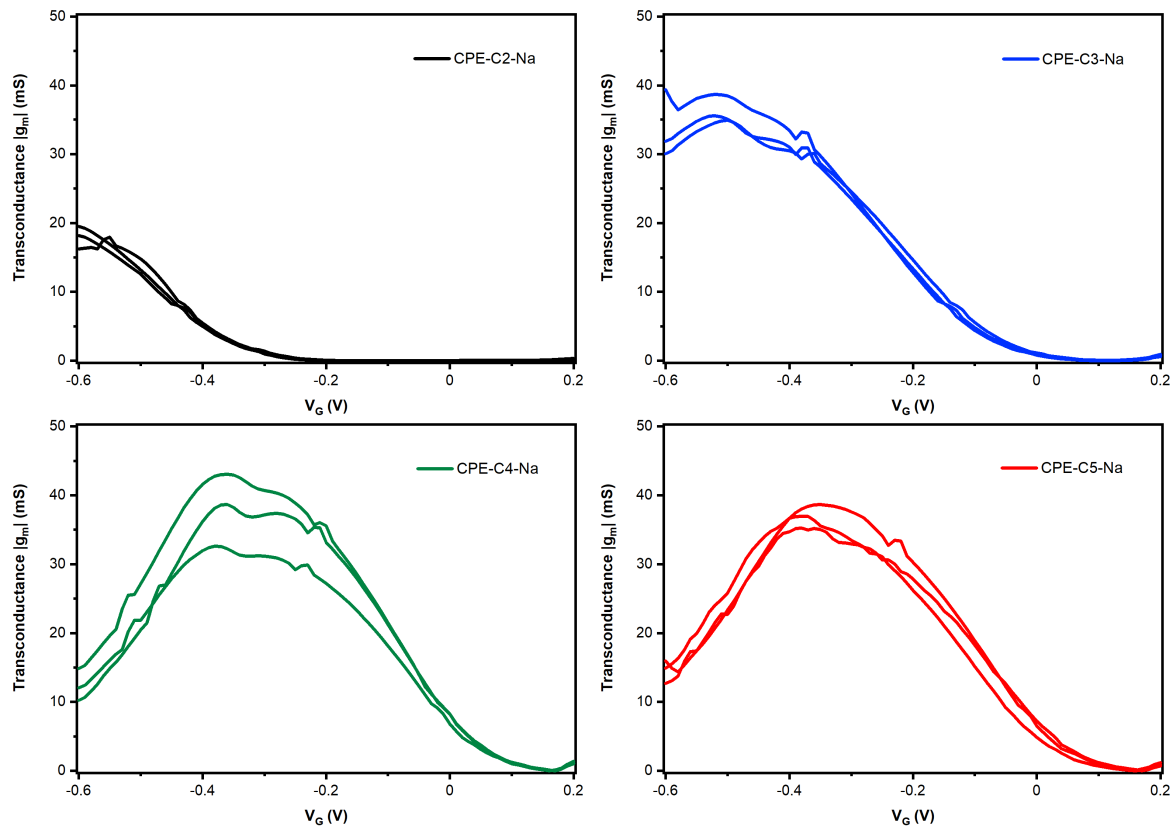


**Figure 4.4.** Transconductance versus applied gate voltage for each CPE material. The transconductance is calculated from the transfer curves from Figure 3.3.

The OECT in this study operates in the p-type accumulation mode; therefore, the current is lowest when there is no voltage applied to the gate and gradually increases as a negative voltage is applied to the gate. Accumulation mode OECTs consume relatively little power compared to depletion mode OECTs because they are generally in the OFF state. Depletion mode devices, such as OECTs made from PEDOT:PSS, are usually in the ON state, hence in the absence of a gate voltage, a hole current flows in the channel.<sup>59</sup>

OECTs operate mainly as transducers by transducing small voltage signals applied to the gate into significant changes in the drain current. Therefore, the transfer characteristics of CPE-based OECTs were evaluated by monitoring the current between the source and drain

contacts ( $I_D$ ) while applying a constant drain voltage ( $V_D$ ) under a series of gate voltages ( $V_G$ ). **Figure 4.2b** exhibits the average transfer curve for each CPE while **Figure 4.3** contains all transfer curves for each CPE. The steeper the transfer curve, the larger the change in drain current for a given gate voltage. The slope of the transfer curve, therefore, defines the sensitivity of the OEECT. This is termed transconductance, a figure of merit for OEECTs. A larger magnitude in transconductance corresponds to a more sensitive OEECT. In order to compare the performance of various OEECT materials, the transconductance must be normalized to the thickness of the active layer. Since OEECTs exhibit volumetric capacitance, transconductance scales with the thickness of the film, including all other channel dimensions.<sup>68</sup> **Figure 4.2c** exhibits the average transconductance of each CPE, while **Figure 4.4** contains the triplicate of transconductance for each material. A clear trend is observed of higher transconductance for a higher number of methylene units. Peak transconductance of 36.8 mS (CPE-C5-Na), 38.1 mS (CPE-C4-Na), 36.3 mS (CPE-C3-Na), and 18.0 mS (CPE-C2-Na) were observed at  $-0.55$  V with channel width, length, and thickness of 1000, 40, and  $1.2 \mu\text{m}$ , respectively. Under a saturation regime, the transconductance ( $g_m$ ) of an OEECT is given by

$$g_m = \left( W \cdot \frac{d}{L} \right) \cdot \mu \cdot C^* \cdot (V_T - V_G) \quad (4.2)$$

where  $W$  is the channel width,  $d$  is the film thickness of the active layer,  $L$  is the channel length,  $\mu$  is the hole mobility in the CPE channel,  $C^*$  is the volumetric capacitance of the CPE channel,  $V_T$  is a geometry-independent threshold voltage, and  $V_G$  is the applied gate voltage. The equation is identical to the equation used to describe OFET transconductance, except that

capacitance in OECTs scales with film thickness. Equation (2) shows that increasing  $C^*$  increases the transconductance of the OECT.

### 4.3 Electrochemical Impedance Spectroscopy Measurements

CPE is expected to exhibit volumetric capacitance due to their water solubility. Sulfonate moieties of the sidechains of CPE allow for water and ions to penetrate and drift within the bulk of the film, allowing for bulk doping and de-doping of the film. Impedance spectroscopy was then used to measure the capacitance for the CPEs (**Figure 4.2d**). The plots for frequency versus capacitance are in the supporting information (Figure S11). The ratio of capacitance obtained at 1 Hz by the volume of the active layer were used to obtain **Figure 4.2d**. A clear effect of the increase in the number of alkyl chains and volumetric capacitance is observed.

Electrochemical impedance spectroscopy (EIS) was also used to measure the relative ionic transport of each CPE (**Figure 4.5**). EIS is a technique that has been used to measure the ionic conductivity of mixed conductors.<sup>28-30</sup> Measuring the ionic transport of a conjugated polyelectrolyte is challenging because electronic transport dominates the signal from ionic transport. Being a highly conductive polymer, CPE-CX-Na had to be de-doped to suppress electron current that would otherwise have made it impossible to measure the ionic transport. Annealing CPE-Na films at 300°C drives water out of the film and reversibly de-dopes the film without decomposing the polymer.<sup>69</sup> CPE films were deposited on top of interdigitated gold electrodes to increase the signal-to-noise ratio. An AC voltage of 20mV was applied at a frequency from 10 Hz to 10 MHz between each electrode. Shown in **Figure 4.5** are exemplary

Nyquist plots of each CPE material. The Nyquist plot data were fitted using the circuit in the **Figure 4.5** inset. A decrease in ion conductivity is observed as the sidechain length is increased. This may be due to the increase in carbon resulting in a decrease in water solubility.

#### 4.4 Exploring Polaron Formation

In order to further understand how a higher number of alkyl chain units lead to higher values for transconductance and volumetric capacitance, a deeper analysis on the system is required. Both these properties will be affected by the doping of the CPE. As discussed in the introduction section, the sulfonate group play a role in stabilizing the radical cation formed upon doping. Therefore, UV-Vis spectroscopy was carried out to investigate the dependence of the stabilization of polaronic states by the distance between the anionic group and the conjugated backbone. CPEs were freeze-dried straight out from dialysis and made into a solution of 10mg/mL. This was used to drop cast onto a glass substrate, and the spectra measured between 300 nm to 1300 nm. The absorption profiles for this series of CPEs exhibit similar features (**Figure 4.6a-b**). Since they have a similar CPDT donor and the same BT acceptor unit, they exhibit the characteristic absorption peaks around 400 nm and 680 nm, previously observed for donor-acceptor copolymers containing CPDT-alt-BT backbone.<sup>70,71</sup> The broad, low-energy transition starting around 900 nm has been observed previously for this class of conjugated polyelectrolytes and was attributed to polaron-type electronic states.<sup>62</sup> The radical cations are stabilized by the pendant sulfonate groups due to Coulombic stabilization.<sup>62,69</sup> Comparison of the relative intensity ratios between  $\lambda_{\text{polaron}}/\lambda_{\text{max}}$  can indicate the influence of alkyl chain lengths on the doping levels. CPE-C2-Na exhibits a ratio of 0.36,

CPE-C3-Na of 0.59, CPE-C4-Na of 0.75 and CPE-C5-Na of 0.81. UV-Vis spectroscopy measurements taken in solution revealed the same trend (**Figure 4.6b**). The ratio  $\lambda_{\text{polaron}}/\lambda_{\text{max}}$  is higher for CPE-C5-Na (1.0), followed by CPE-C4-Na (0.78), CPE-C3-Na (0.48), and CPE-C2-Na (0.07). Considering that anionic groups ( $\text{SO}_3^-$ ) play a role in stabilizing the cationic polaronic states due to Coulombic stabilization, it was expected that shorter alkyl chains would lead to a higher degree of doping. UV-Vis spectra demonstrated an opposite effect than what was initially expected. Although the results agree with what has been observed for the OECTs performance.

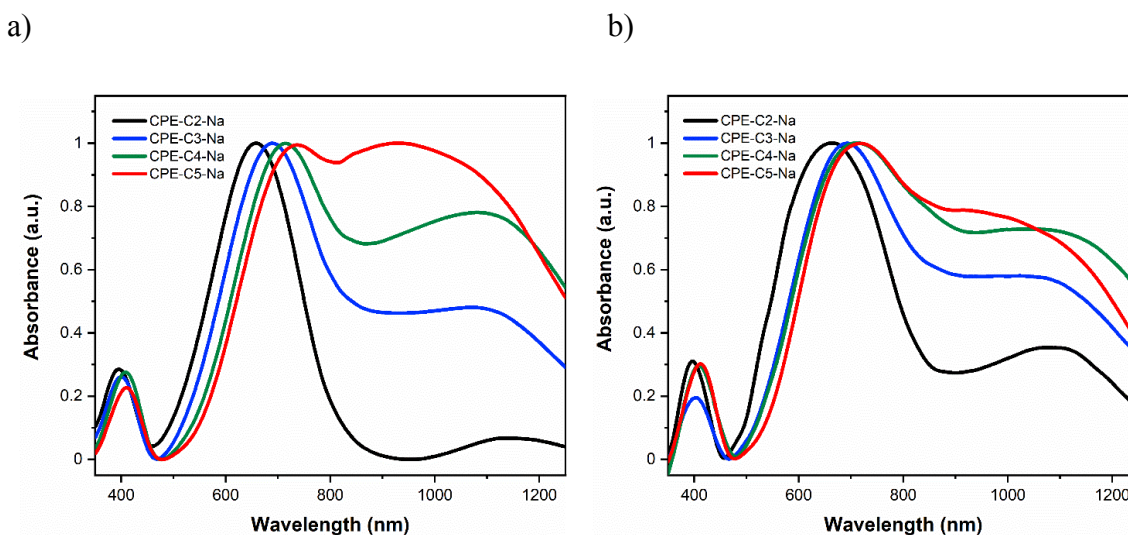


**Figure 4.6.** a) Ultraviolet-visible-near-infrared spectroscopy (UV-Vis-NIR) of aqueous CPE solutions; b) UV-Vis-NIR of CPE films deposited ITO/glass substrates

The proposed doping mechanism for the CPEs under study consists of two steps: 1) protonation of the cyclopentadithiophene unit of the polymer and formation of a cation; 2) a single electron transfer from a neutral polymer chain to the protonated polymer (comproportionation), resulting in one polymer chain with a positive polaron and another polymer chain with an unpaired electron.<sup>69,72</sup> The electron transfer during the doping process

can be related to the driving force of the chain to be oxidized. Therefore, electrochemical characterization can help understand the impact of the alkyl chain length on the doping of the CPE.

The trend observed for doping in UV-VIS can be explained by the electron-withdrawing effect of the sulfonate group on the conjugated backbone, decreasing the electron density in the ring and making difficult the electron transfer during the comproportionation step for polaron formation, leading to a lower degree of doping, as indicated by the voltammetry analysis on these CPEs. Another aspect to consider is the increase in flexibility of the alkyl chain as the number of carbons increased. A higher number of methylene units in the alkyl chain translates to a larger conformational space, and therefore, to an easier approximation of the sulfonate group to the conjugated backbone. This can also lead to a higher degree of polaron stabilization and a higher degree of doping.

Ultraviolet-photoelectron spectroscopy (UPS) was carried out (**Figure 4.7c**) on films of CPE-C2-Na, CPE-C3-Na, CPE-C4-Na, and CPE-C5-Na spin-coated atop ITO/glass substrates to investigate the energy levels of the synthesized CPEs. The abscissa is the binding energy relative to the Fermi level of Au ( $E_F$ ), which is defined by the energy of the electron before excitation relative to the vacuum level. The highest occupied molecular orbital onsets ( $E_{HOMO}$ ) were obtained in the low energy region. The values for ionization potential (IP) obtained by this technique were -5.24 (CPE-C2-Na), -5.23 (CPE-C3-Na), -5.17 (CPE-C4-Na), and -5.19 (CPE-C5-Na). A trend of lower IP for longer alkyl chains is observed from CPE-C2-Na to CPE-C4-Na. For CPE-C5-Na, the IP is similar to that of CPE-C4-Na. Differences in the values determined by UPS can be attributed to the technique. UPS is sensitive to the very near-surface region, probing only the top few nm of the sample.

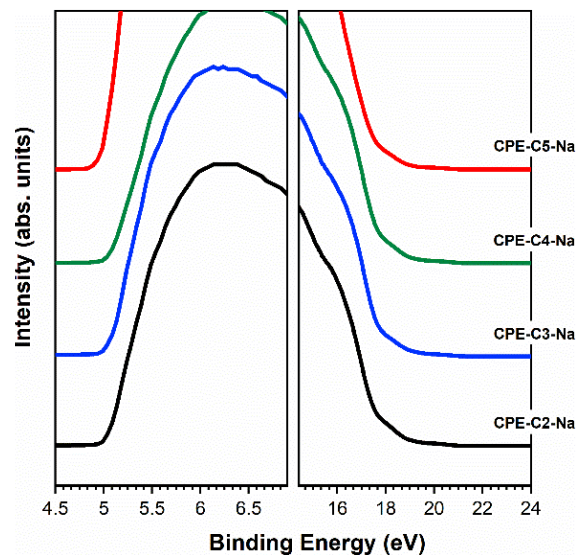


**Figure 4.7.** UPS spectra of CPE-CX-Na polymers. Films were deposited on conducting ITO substrates.

#### 4.5 Grazing Incidence Wide Angle X-Ray Spectroscopy of CPE's

Grazing incidence wide-angle X-ray scattering (GIWAXS) was employed to study the structural organization of thin spin-cast films of the CPEs on Si substrates. Both neat (**Figure 4.11**) and GOPS cross-linked CPE films (**Figure 4.12**) were prepared and measured by GIWAXS. An increase in scattering intensity is observed in both the  $q_{xy}$  and  $q_z$  plane with an increase of the sidechain length, suggesting an increase in crystallinity. The signal around  $1.7 \text{ \AA}^{-1}$  along the  $q_{xy}$  plane is often observed in organic semiconducting molecules and corresponds to the  $\pi$ - $\pi$  stacking distance. The  $\pi$ - $\pi$  stacking distance is the distance between the aromatic rings in the backbone of neighboring CPE molecules. No big change in the  $\pi$ - $\pi$  stacking

distance is observed for these materials. We do not observe this peak in CPE-C2-Na, which suggests that the material is amorphous. Scattering along the  $q_z$  plane around  $0.5 \text{ \AA}^{-1}$  is observed to increase in intensity as the sidechain length is increased. The signal also shifts to smaller  $\text{\AA}^{-1}$ , which corresponds to longer distances of the ordered packing in physical space. The identity of the packing cannot be identified, because of the lack of single crystal information. However, the increase in the packing distance with increasing sidechain length suggests that the signal in the  $q_z$  direction is due to alkyl chain packing. Very sharp and defined scattering peaks are observed in the crosslinked CPE films, which is indicative of GOPS aggregated crystallites that are large enough to scatter the X-ray from the GIWAXS. From the GIWAXs data, the increase in crystallinity observed for higher number of methylene units could be correlated to an increase in hole conduction, resulting in OECT devices with better performance. **Figure 4.13** of the supporting information shows the height images measured by atomic force microscopy (AFM) of CPE-CX-Na. The surface morphology of the CPE-CX-Na films does not change significantly with increasing side-chain length. All films look amorphous and smooth with and root mean square roughness between 0.3 and 0.4 nm.

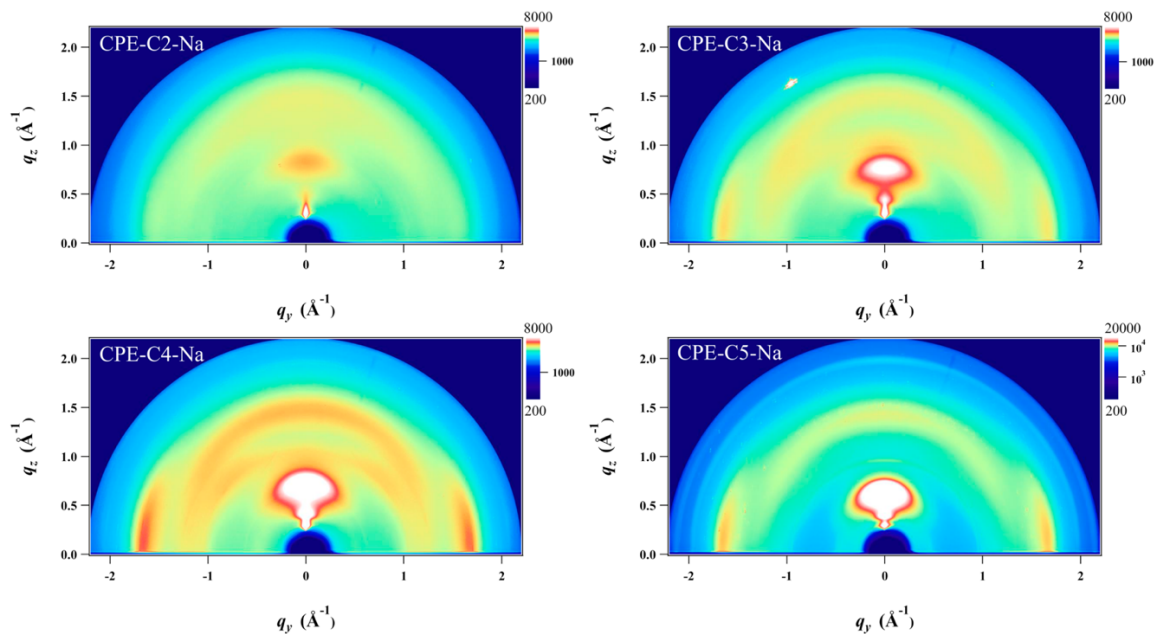


**Figure 4.11.** Grazing-incidence wide-angle X-ray scattering (GIWAXS) images of neat CPE derivative thin films on silicon substrates.

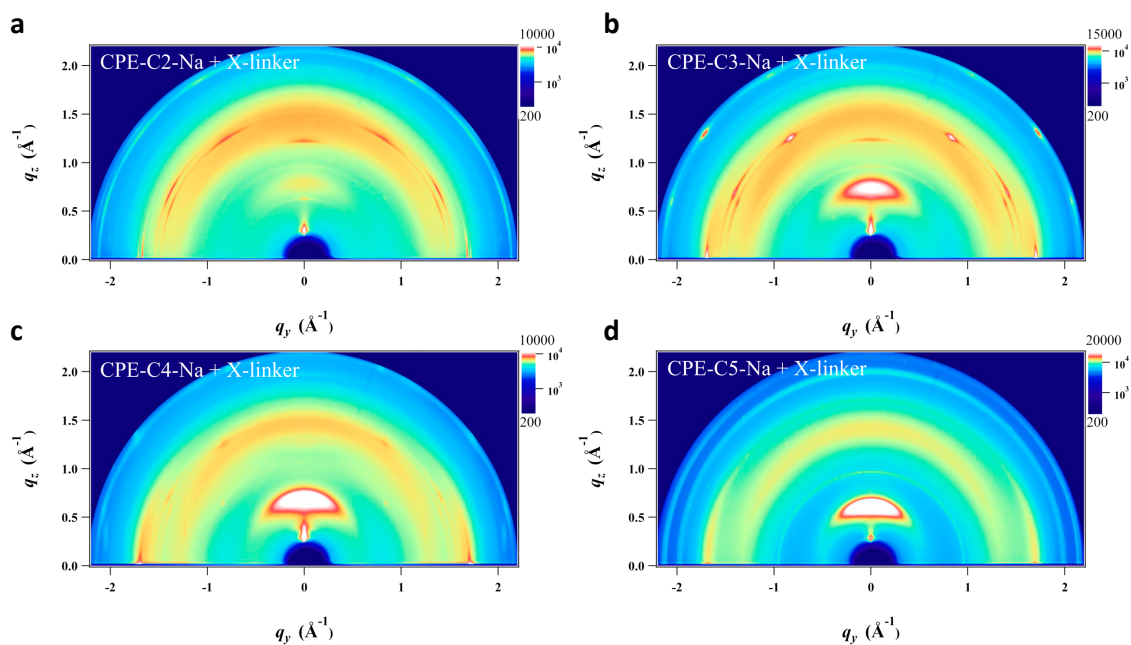


**Figure 4.12.** Grazing-incidence wide-angle X-ray scattering (GIWAXS) images of cross-linked CPE derivative thin films on silicon substrates. The CPE derivative films contain (a) 32% (b) 32% (c) 32% (d) and 16% GOPS cross-linker by weight.

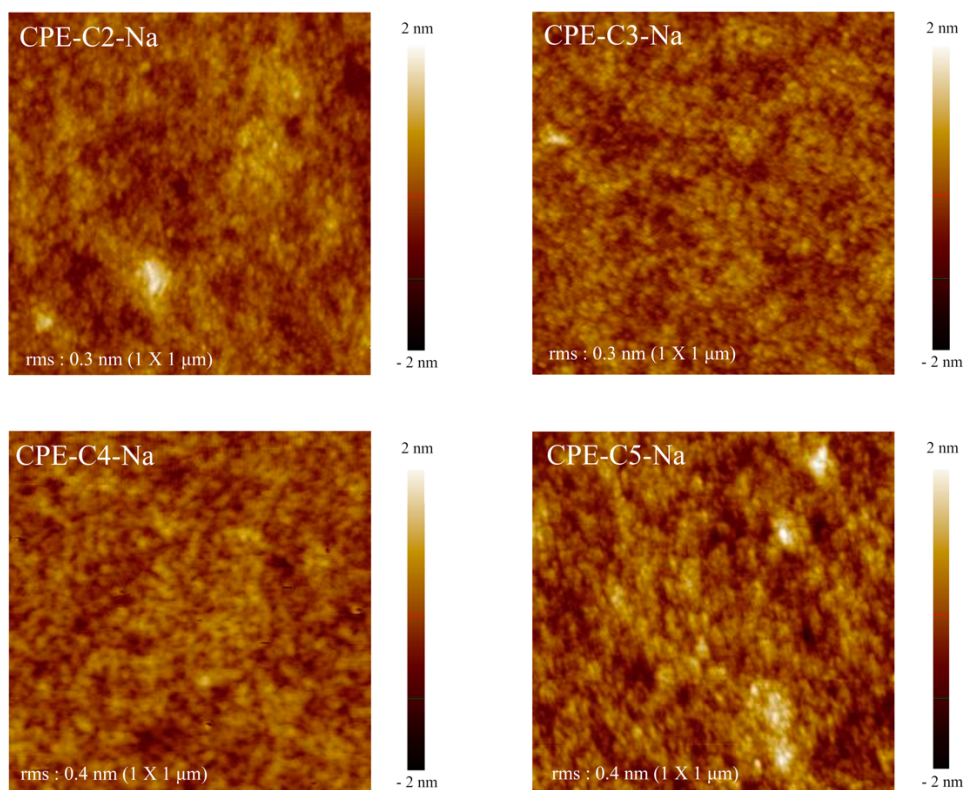


**Figure 4.13.** Morphology measured by Atomic Force Microscopy (AFM) of neat CPE-CX-Na films prepared from solution.

## 4.6 Experimental Section

*OEET Fabrication:* Gold electrodes were patterned on glass wafers using standard clean-room lithography protocols. Polydimethylsiloxane (PDMS) wells were used to contain the electrolyte and insulate the gold contacts from the electrolyte. PDMS was prepared from Sylgard<sup>®</sup> 184 from Dow-Corning using a mixing ratio of 10:1 between the base and the curing agent with a curing time of 4 hours at 80 °C. Wells were cut from a sheet of PDMS and fused to the patterned glass substrates using an oxygen plasma. For the device fabrication,

polydimethylsiloxane (PDMS) wells were bonded to cleaned glass substrates by exposing both surfaces to an oxygen plasma before placing the well. The purpose of incorporating the PDMS well was to confine the electrolyte above the channel area and to reduce the leakage current between the source and drain contacts and the gate electrode. CPE films were deposited by drop-casting 14  $\mu\text{L}$  of 10 mg/mL solutions of CPE in Milli-Q® into the PDMS well. 2  $\mu\text{L}$  of 32 %wt GOPS in 1:1 methanol:Milli-Q® water solution was added to CPE-C2-Na, CPE-C3-Na and CPE-C4-Na for cross-linking. 2  $\mu\text{L}$  of 16 %wt GOPS in 1:1 methanol:Milli-Q® water solution was added to CPE-C5-Na. After dispensing the solutions into the well, the devices were heated to 80°C for 15 minutes to drive off the solvent, followed by 110°C for 1 hour to cross-link the film.

*Thickness Measurements:* The thickness of the CPE films was determined using an Ambios XP-100 profilometer. A line of CPE material was removed using the backside of a razor blade and the profilometer was scanned across multiple points along the scratch.

*Electrical Characterization:* Electrical characterization was performed using a Keithley® semiconductor parametric analyzer (model 4200-SCS). Transfer curves were measured with a 1 second hold time as each data point.

*Dielectric Characterization:* The capacitance of CPE films were measured using a Solartron SI 1260A impedance analyzer. An AC voltage of 40 mV was applied between a Ag/AgCl electrode and the CPE film at a frequency from 0.1 Hz to 10 MHz.

*Ionic Transport via Electrochemical Impedance Spectroscopy:* The ionic conductivity of each CPE material was compared using electrochemical impedance spectroscopy on a Solartron SI 1260A impedance analyzer running ZPlot® software. CPE films were prepared by drop casting 14  $\mu\text{L}$  of a 10 mg/mL solution on interdigitated gold electrodes. Films were de-doped by annealing at 300°C to drive off moisture in the film. With one interdigitated electrode as the working electrode and the other as the counter electrode, we applied an AC voltage of 20 mV at a frequency of 10 Hz to 10 MHz. The measured Nyquist plot was fit to a circuit shown in the Figure S12 inset using ZView® software.

*UV-vis-nIR:* All UV-vis-nIR spectra were obtained using a Perkin-Elmer Lambda 750 UV-vis-nIR spectrometer using a tungsten lamp for the visible to near-IR region and a deuterium lamp for the UV region. CPE films for spectroelectrochemistry were prepared by drop-casting 30  $\mu\text{L}$  of a solution of 10 mg/mL CPE onto a cleaned ITO-coated glass substrate. For solution measurement, 10  $\mu\text{L}$  of 1mg/mL solution was dissolved in 3mL of water.

*Synchrotron-based GIWAXS measurements:* Two-dimensional (2D)-GIWAXS measurements were performed at the PLS-II 5A beamline of the Pohang Accelerator Laboratory (PAL) in Korea. 2D-GIWAXS images were collected at a 0.12 incidence angle with 11.57 keV ( $\lambda = 1.07156 \text{ \AA}$ ) and a MAR345 image plate detector (sample-to-detector distance: 414.6045 mm).

*Atomic Force Microscopy (AFM):* All topographic images were obtained using an Asylum MFP-3D mounted atop an Olympus inverted optical microscope under and inert atmosphere. Silicon tips with a resonant frequency of 300 kHz and a force constant of 40 N/m were used

(Budget Sensors). First order image flattening was performed on the morphology images on Asylum Research AFM software version 14, programmed using IGOR Pro.

*Ultraviolet-Photoelectron Spectroscopy (UPS):* UPS was carried out with a Kratos Axis Ultra X-ray Photoelectron Spectroscopy (XPS) system on drop casted films prepared from 30  $\mu\text{L}$  of a solution of 10 mg/mL CPE materials on top of ITO coated glass substrates. A clean piece of silver was argon etched to get the exact zero position of the system for an accurate calibration of the energy scale. The ionization potential of each CPE material was determined by subtracting the width of the high-binding cutoff and the highest occupied state (HOS) from the 21.22 eV of the incident photon. The data was processed using CasaXPS<sup>©</sup> software.

#### **4.7 Conclusions**

In conclusion, we have presented a systematic structure-property-relationship study on conjugated polyelectrolytes with varying side-chain lengths. Before studying this series of CPE's, it was hypothesized that the proximity of the polaron-stabilizing negative charge would increase the ease of doping as the side-chain length is decreased. The opposite trend was observed when once we began characterizing the CPE materials. Ultraviolet-visible-near-infrared spectroscopy and Ultraviolet-photoelectron spectroscopy also demonstrated the general trend of increasing ease of doping as the side-chain length is increased. Organic electrochemical transistor performance (OECT) shows a general trend of increasing performance as the side-chain length is increased. CPE-2-Na shows the lowest

transconductance, followed by CPE-3-Na. CPE-4-Na and CPE-5-Na show similar levels of transconductance to each other and higher transconductance than the two other materials. This study demonstrates one of the few structure-property-relationship studies to develop high-performance CPE's for OECT applications.

#### 4.8 References

1. Simon, D. T.; Gabrielsson, E. O.; Tybrandt, K.; Berggren, M. Organic Bioelectronics: Bridging the Signaling Gap between Biology and Technology. *Chemical Reviews* **2016**, *116* (21), 13009–13041.
2. Shirakawa, H.; Louis, E. J.; MacDiarmid, A. G.; Chiang, C. K.; Heeger, A. J. Synthesis of Electrically Conducting Organic Polymers: Halogen Derivatives of Polyacetylene, (CH)<sub>x</sub>. *Journal of the Chemical Society, Chemical Communications* **1977**, No. 16, 578–580.
3. Rivnay, J.; Owens, R. M.; Malliaras, G. G. The Rise of Organic Bioelectronics. *Chemistry of Materials* **2014**, *26* (1), 679–685.
4. Musumeci, C.; Vagin, M.; Zeglio, E.; Ouyang, L.; Gabrielsson, R.; Ingnäs, O. Organic Electrochemical Transistors from Supramolecular Complexes of Conjugated Polyelectrolyte PEDOTS. *Journal of Materials Chemistry C* **2019**, *7* (10), 2987–2993.
5. Jiang, H.; Taranekekar, P.; Reynolds, J. R.; Schanze, K. S. Conjugated Polyelectrolytes: Synthesis, Photophysics, and Applications. *Angewandte Chemie - International Edition* **2009**, *48* (24), 4300–4316.
6. Mccuskey, S. R.; Su, Y.; Leifert, D.; Moreland, A. S.; Bazan, G. C. Living Bioelectrochemical Composites. *Advanced Materials* **2020**, *1908178*, 1–6.
7. Su, Y.; Mccuskey, S. R.; Leifert, D.; Moreland, A. S.; Zhou, L.; Llanes, L. C.; Vazquez, R. J.; Sepunaru, L.; Bazan, G. C.; Barbara, S.; Barbara, S.; Solids, O.; Barbara, S. Biological-Synthetic Composites That Switch Operation between Current Generation and Electrochemical Energy Storage. 1–19.

8. Feng, G.; Mai, C. K.; Zhan, R.; Bazan, G. C.; Liu, B. Narrow Band Gap Conjugated Polyelectrolytes for Photothermal Killing of Bacteria. *Journal of Materials Chemistry B* **2015**, *3* (37), 7340–7346.
9. Lill, A. T.; Cao, D. X.; Schrock, M.; Vollbrecht, J.; Huang, J.; Nguyen-Dang, T.; Brus, V. V.; Yurash, B.; Leifert, D.; Bazan, G. C.; Nguyen, T. Q. Organic Electrochemical Transistors Based on the Conjugated Polyelectrolyte PCPDTBT-SO<sub>3</sub>K (CPE-K). *Advanced Materials* **2020**, *32* (33), 1–9.
10. Schmidt, M. M.; ElMahmoudy, M.; Malliaras, G. G.; Inal, S.; Thelakkat, M. Smaller Counter Cation for Higher Transconductance in Anionic Conjugated Polyelectrolytes. *Macromolecular Chemistry and Physics* **2018**, *219* (2), 1–10.
11. Zeglio, E.; Schmidt, M. M.; Thelakkat, M.; Gabrielsson, R.; Solin, N.; Inganäs, O. Conjugated Polyelectrolyte Blends for Highly Stable Accumulation-Mode Electrochemical Transistors. *Chemistry of Materials* **2017**, *29* (10), 4293–4300.
12. Inal, S.; Rivnay, J.; Leleux, P.; Ferro, M.; Ramuz, M.; Brendel, J. C.; Schmidt, M. M.; Thelakkat, M.; Malliaras, G. G. A High Transconductance Accumulation Mode Electrochemical Transistor. *Advanced Materials* **2014**, *26* (44), 7450–7455.
13. Khodagholy, D.; Doublet, T.; Quilichini, P.; Gurfinkel, M.; Leleux, P.; Ghestem, A.; Ismailova, E.; Hervé, T.; Sanaur, S.; Bernard, C.; Malliaras, G. G. In Vivo Recordings of Brain Activity Using Organic Transistors. *Nature Communications* **2013**, *4*.
14. Khodagholy, D.; Gelinias, J. N.; Thesen, T.; Doyle, W.; Devinsky, O.; Malliaras, G. G.; Buzsáki, G. NeuroGrid: Recording Action Potentials from the Surface of the Brain. *Nat Neurosci* **2015**, *18* (2), 310–315.
15. Rivnay, J.; Wang, H.; Fenno, L.; Deisseroth, K.; Malliaras, G. G. Next-Generation Probes, Particles, and Proteins for Neural Interfacing. *Science Advances* **2017**, *3* (6).
16. Khodagholy, D.; Gelinias, J. N.; Zhao, Z.; Yeh, M.; Long, M.; Greenlee, J. D.; Doyle, W.; Devinsky, O.; Buzsáki, G. Organic Electronics for High-Resolution Electroencephalography of the Human Brain. *Science Advances* **2016**, *2* (11).
17. Jo, Y. J.; Kwon, K. Y.; Khan, Z. U.; Crispin, X.; Kim, T. II. Gelatin Hydrogel-Based Organic Electrochemical Transistors and Their Integrated Logic Circuits. *ACS Applied Materials and Interfaces* **2018**, *10* (45), 39083–39090.

18. Scheiblin, G.; Coppard, R.; Owens, R. M.; Mailley, P.; Malliaras, G. G. Referenceless PH Sensor Using Organic Electrochemical Transistors. *Advanced Materials Technologies* **2017**, *2* (2), 1–5.
19. Khodagholy, D.; Curto, V. F.; Fraser, K. J.; Gurfinkel, M.; Byrne, R.; Diamond, D.; Malliaras, G. G.; Benito-Lopez, F.; Owens, R. M. Organic Electrochemical Transistor Incorporating an Ionogel as a Solid State Electrolyte for Lactate Sensing. *Journal of Materials Chemistry* **2012**, *22* (10), 4440–4443.
20. Braendlein, M.; Pappa, A. M.; Ferro, M.; Lopresti, A.; Acquaviva, C.; Mamessier, E.; Malliaras, G. G.; Owens, R. M. Lactate Detection in Tumor Cell Cultures Using Organic Transistor Circuits. *Advanced Materials* **2017**, *29* (13).
21. Macchia, E.; Romele, P.; Manoli, K.; Ghittorelli, M.; Magliulo, M.; Kovács-Vajna, Z. M.; Torricelli, F.; Torsi, L. Ultra-Sensitive Protein Detection with Organic Electrochemical Transistors Printed on Plastic Substrates. *Flexible and Printed Electronics* **2018**, *3* (3).
22. Pappa, A. M.; Ohayon, D.; Giovannitti, A.; Maria, I. P.; Savva, A.; Uguz, I.; Rivnay, J.; McCulloch, I.; Owens, R. M.; Inal, S. Direct Metabolite Detection with an N-Type Accumulation Mode Organic Electrochemical Transistor. *Science Advances* **2018**, *4* (6), 1–8.
23. Parlak, O.; Keene, S. T.; Marais, A.; Curto, V. F.; Salleo, A. Molecularly Selective Nanoporous Membrane-Based Wearable Organic Electrochemical Device for Noninvasive Cortisol Sensing. *Science Advances* **2018**, *4* (7).
24. Borges-González, J.; Kousseff, C. J.; Nielsen, C. B. Organic Semiconductors for Biological Sensing. *Journal of Materials Chemistry C* **2019**, *7* (5), 1111–1130.
25. Wang, N.; Yang, A.; Fu, Y.; Li, Y.; Yan, F. Functionalized Organic Thin Film Transistors for Biosensing. *Accounts of Chemical Research* **2019**.
26. Diacci, C.; Lee, J. W.; Janson, P.; Dufil, G.; Méhes, G.; Berggren, M.; Simon, D. T.; Stavriniidou, E. Real-Time Monitoring of Glucose Export from Isolated Chloroplasts Using an Organic Electrochemical Transistor. *Advanced Materials Technologies* **2020**, *5* (3).

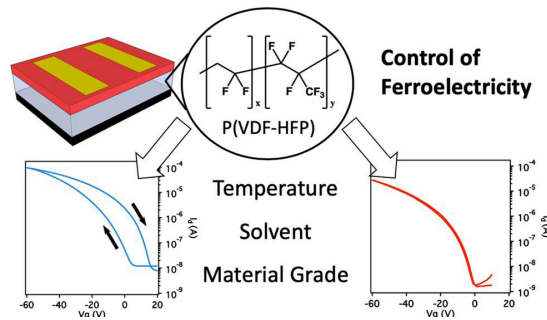
27. Wustoni, S.; Combe, C.; Ohayon, D.; Akhtar, M. H.; McCulloch, I.; Inal, S. Membrane-Free Detection of Metal Cations with an Organic Electrochemical Transistor. *Advanced Functional Materials* **2019**, *29* (44), 1–10.
28. Someya, T.; Bao, Z.; Malliaras, G. G. The Rise of Plastic Bioelectronics. *Nature* **2016**, *540* (7633), 379–385.
29. Rivnay, J.; Inal, S.; Salleo, A.; Owens, R. M.; Berggren, M.; Malliaras, G. G. Organic Electrochemical Transistors. *Nature Reviews Materials* **2018**, *3*.
30. Bernards, D. A.; Malliaras, G. G. Steady-State and Transient Behavior of Organic Electrochemical Transistors. *Advanced Functional Materials* **2007**, *17* (17), 3538–3544.
31. Nielsen, C. B.; Giovannitti, A.; Sbircea, D. T.; Bandiello, E.; Niazi, M. R.; Hanifi, D. A.; Sessolo, M.; Amassian, A.; Malliaras, G. G.; Rivnay, J.; McCulloch, I. Molecular Design of Semiconducting Polymers for High-Performance Organic Electrochemical Transistors. *Journal of the American Chemical Society* **2016**, *138* (32), 10252–10259.
32. Mai, C. K.; Zhou, H.; Zhang, Y.; Henson, Z. B.; Nguyen, T. Q.; Heeger, A. J.; Bazan, G. C. Facile Doping of Anionic Narrow-Band-Gap Conjugated Polyelectrolytes during Dialysis. *Angewandte Chemie - International Edition* **2013**, *52* (49), 12874–12878.
33. Mai, C. K.; Russ, B.; Fronk, S. L.; Hu, N.; Chan-Park, M. B.; Urban, J. J.; Segalman, R. A.; Chabinye, M. L.; Bazan, G. C. Varying the Ionic Functionalities of Conjugated Polyelectrolytes Leads to Both P- and n-Type Carbon Nanotube Composites for Flexible Thermoelectrics. *Energy and Environmental Science* **2015**, *8* (8), 2341–2346.
34. Liu, B.; Gaylord, B. S.; Wang, S.; Bazan, G. C. Effect of Chromophore-Charge Distance on the Energy Transfer Properties of Water-Soluble Conjugated Oligomers. *Journal of the American Chemical Society* **2003**, *125* (22), 6705–6714.
35. Lee, W.; Seo, J. H.; Woo, H. Y. Conjugated Polyelectrolytes: A New Class of Semiconducting Material for Organic Electronic Devices. *Polymer* **2013**, *54* (19), 5104–5121.
36. Duc, C.; Malliaras, G. G.; Senez, V.; Vlandas, A. Long-Term Ageing of PEDOT:PSS: Wettability Study. *Synthetic Metals* **2018**, *238* (October 2017), 14–21.

37. Niepelt, R.; Schröder, U. C.; Sommerfeld, J.; Slowik, I.; Rudolph, B.; Möller, R.; Seise, B.; Csaki, A.; Fritzsche, W.; Ronning, C. Biofunctionalization of Zinc Oxide Nanowires for DNA Sensory Applications. *Nanoscale Research Letters* **2011**, *6*, 1–7.
38. Rivnay, J.; Leleux, P.; Ferro, M.; Sessolo, M.; Williamson, A.; Koutsouras, D. A.; Khodagholy, D.; Ramuz, M.; Strakosas, X.; Owens, R. M.; Benar, C.; Badier, J.-M.; Bernard, C.; Malliaras, G. G. High-Performance Transistors for Bioelectronics through Tuning of Channel Thickness. *Science Advances* **2015**, *1* (4), e1400251.
39. Dong, B. X.; Nowak, C.; Onorato, J. W.; Strzalka, J.; Escobedo, F. A.; Luscombe, C. K.; Nealey, P. F.; Patel, S. N. Influence of Side-Chain Chemistry on Structure and Ionic Conduction Characteristics of Polythiophene Derivatives: A Computational and Experimental Study. *Chem. Mater.* **2019**, *31* (4), 1418–1429.
40. Dong, B. X.; Liu, Z.; Misra, M.; Strzalka, J.; Niklas, J.; Poluektov, O. G.; Escobedo, F. A.; Ober, C. K.; Nealey, P. F.; Patel, S. N. Structure Control of a  $\pi$ -Conjugated Oligothiophene-Based Liquid Crystal for Enhanced Mixed Ion/Electron Transport Characteristics. *ACS Nano* **2019**, *13* (7), 7665–7675.
41. Dong, B. X.; Bennington, P.; Kambe, Y.; Sharon, D.; Dolejsi, M.; Strzalka, J.; Burnett, V. F.; Nealey, P. F.; Patel, S. N. Nanothin Film Conductivity Measurements Reveal Interfacial Influence on Ion Transport in Polymer Electrolytes. *Mol. Syst. Des. Eng.* **2019**, *4* (3), 597–608.
42. Cao, D. X.; Leifert, D.; Brus, V. V.; Wong, M. S.; Phan, H.; Yurash, B.; Koch, N.; Bazan, G. C.; Nguyen, T.-Q. The Importance of Sulfonate to the Self-Doping Mechanism of the Water-Soluble Conjugated Polyelectrolyte PCPDTBT-SO<sub>3</sub>K. *Materials Chemistry Frontiers* **2020**.
43. Soci, C.; Hwang, I. W.; Moses, D.; Zhu, Z.; Waller, D.; Gaudiana, R.; Brabec, C. J.; Heeger, A. J. Photoconductivity of a Low-Bandgap Conjugated Polymer. *Advanced Functional Materials* **2007**, *17* (4), 632–636.
44. Mühlbacher, D.; Scharber, M.; Morana, M.; Zhu, Z.; Waller, D.; Gaudiana, R.; Brabec, C. High Photovoltaic Performance of a Low-Bandgap Polymer. *Advanced Materials* **2006**, *18* (21), 2884–2889.

45. Han, C. C.; Elsenbaumer, R. L. Protonic Acids: Generally Applicable Dopants for Conducting Polymers. *Synthetic Metals* **1989**, *30* (1), 123–131.  
[https://doi.org/10.1016/0379-6779\(89\)90648-6](https://doi.org/10.1016/0379-6779(89)90648-6).
46. Meerholz, K.; Gregorius, H.; Miillen, K.; Heinze, J. Voltammetric Studies of Solution and Solid-State Properties of Monodisperse Oligo(p-Phenylenevin Ylene)s. *Advanced Materials* **1994**, *9* (6), 671–674.
47. Heinze, J.; Frontana-Urbe, B. A.; Ludwigs, S. Electrochemistry of Conducting Polymers-Persistent Models and New Concepts. *Chemical Reviews* **2010**, *110* (8), 4724–4771.
48. Sweetnam, S.; Graham, K. R.; Ngongang Ndjawa, G. O.; Heumüller, T.; Bartelt, J. A.; Burke, T. M.; Li, W.; You, W.; Amassian, A.; McGehee, M. D. Characterization of the Polymer Energy Landscape in Polymer:Fullerene Bulk Heterojunctions with Pure and Mixed Phases. *Journal of the American Chemical Society* **2014**, *136* (40), 14078–14088.

## Chapter 5:

### High-K Fluoropolymer Gate Dielectric in Electrically Stable Organic Field-Effect Transistors



#### 5.1 Introduction and Motivation

In this chapter, a detailed study of a high-k fluoropolymer gate dielectric material, P(VDF-HFP), is presented as a guide to achieve low operational voltage and electrically stable device performance. The large dipole moment of C-F dipoles in P(VDF-HFP) is responsible for its high dielectric constant as well as its potentially ferroelectric behavior that must be minimized to avoid hysteretic current-voltage characteristics. A range of material grades and processing conditions are explored and are shown to have a significant effect on the degree of hysteresis observed in device transfer characteristics. The percent of HFP monomer in the P(VDF-HFP) dielectric has an effect on gate-dependent mobility induced by disorder at the semiconductor-dielectric interface. Most importantly, we present the considerations that must be made to achieve optimal performance in multiple device architectures of organic field-effect transistors when using P(VDF-HFP) as a dielectric layer.

Among the ongoing goals of the organic field-effect transistor (OFET) community is the fabrication of electrically stable transistors. SiO<sub>2</sub> is a commonly used gate insulator layer in OFETs research due to its low cost, small leakage current and commercial availability. However, the detrimental charge trapping at the SiO<sub>2</sub>-semiconductor interface can result in double-slope nonideality characteristics, as well as a threshold voltage shift and concomitant reduction in current when the device is continuously biased.<sup>1-6</sup> To solve these issues, research groups have turned to the functionalization of the SiO<sub>2</sub> surface with a self-assembled monolayer (SAM); however, procedures must be carefully controlled to get consistently high quality results.<sup>7</sup> Others have substituted SiO<sub>2</sub> with polymer gate dielectric materials free of functional groups that interfere with electrical stability, such as fluoropolymers (Cytop™) and siloxane-based materials (divinyltertramethyldisiloxane-bis(benzocyclobutene) (BCB)).<sup>8-11</sup> The low dielectric constant ( $\epsilon$ ) of these polymeric materials (2.1 and 2.7 for Cytop™ and BCB, respectively) makes it necessary to employ thin dielectric layers if one seeks to achieve low operational voltage, which increases the risk of leakage current and shorting. Cytop™ is an expensive material (~1000\$/50mL) that can only be acquired as a proprietary solution, and can only be used in top-gate OFET device architectures. Ideally, polymer gate dielectrics used in research laboratories are of low cost and widely commercially available. Poly(vinylidene fluoride) (PVDF) and its copolymers are a strong candidate gate dielectric material for low voltage and electrically stable OFET operation due to their remarkably high dielectric constant ( $\epsilon = 10 - 40$ ), extremely low cost (~10\$/50mL), and lack of functional groups which are known to trap charges.<sup>3</sup> VDF-based polymers are widely used for industrial applications due to their ease of processability and high chemical stability, and are available in a wide range of copolymer structures and ratios with unique properties. PVDF and their copolymers are known

to exhibit ferroelectric behavior due to the reorientation of carbon-fluorine (C-F) dipoles under a high electric field. A ferroelectric material will retain its polarization when the electric field is removed. The reader is referred to a number of excellent review articles on the ferroelectric behavior of PVDF.<sup>12,13</sup> It is important to be aware that the large dipole moment of C-F dipoles in PVDF is both responsible for its high dielectric constant and potentially ferroelectric behavior. PVDF and VDF-containing copolymers are used in nonvolatile memory applications by taking advantage of its ferroelectric properties.<sup>14,15</sup> By polarizing the dielectric layer, the current level at 0 V gate bias can be tuned to represent a ‘zero’ or ‘one’ memory state. In OFETs used in logic applications, ferroelectric behavior must be minimized to avoid hysteretic current-voltage characteristics.<sup>16-23</sup> Among the reported OFET devices that use PVDF and its copolymers as a gate dielectric, little is understood about how to control ferroelectricity. We report a study of the polymer gate-dielectric material poly(vinylidene fluoride-co-hexafluoropropylene) (P(VDF-HFP)) (**Figure 5.1a**) and offer guidelines for the fabrication of electrically stable high-k OFETs. We find that the degree of ferroelectricity and device transfer characteristics are heavily dependent on the processing conditions and choosing the proper grade of P(VDF-HFP). Incorrect choice of processing conditions and material grade results in non-ideal transfer characteristics such as low on-off ratio, large threshold voltage and large hysteresis. The electrical stability as well as the low voltage operation of P(VDF-HFP) devices will be demonstrated to convince the reader that VDF-based polymer dielectric materials are worth further investigation by the OFET community. Focus is placed on how to choose the correct grade of material as well as the processing conditions to control the ferroelectric behavior of P(VDF-HFP). Moreover, we explore the effect of the percent of HFP monomer on device performance.

## 5.2 P(VDF-HFP) As a Passivation Layer for Organic Field-Effect Transistors

P(VDF-HFP) can reproducibly and effectively be used as a passivation layer to improve electrical stability by spin coating a thin layer on top of SiO<sub>2</sub>. Bottom-gate/top-contact devices were fabricated with a dielectric layer of P(VDF-HFP) (Kynar Superflex®) on top of SiO<sub>2</sub>. Devices were compared with OFETs fabricated with SiO<sub>2</sub> treated with decyltrichlorosilane (DTS), which forms a self-assembled monolayer (SAM). Silane-based SAM surface treatment is a common surface passivation technique and has been used to tune the surface energy of SiO<sub>2</sub> to improve the mobility and electrical stability of OFETs using SiO<sub>2</sub> as a gate dielectric.<sup>7,24-28</sup> PhF<sub>2,6</sub>, a high-mobility, p-type, donor-acceptor (D-A) semiconducting polymer based on 4,4-dihexadecyl-4H-cyclopenta[1,2-b:5,4-b']dithiophene (CDT) and 2,6-difluorophenylene (2,6-DFPh) (**Figure 5.1a**), was used as the active layer for all devices in this study.<sup>29,30</sup> DTS was used in previous publications to passivate the SiO<sub>2</sub> gate dielectric layer in OFETs containing a PhF<sub>2,6</sub> active layer. Current-voltage characteristics show that P(VDF-HFP) acts as a successful passivation layer, and electrical stability is greatly improved relative to SiO<sub>2</sub> treated with DTS. **Figure 5.1b** shows the transfer characteristics in the saturation regime ( $V_d = -80$  V) of devices made of DTS-treated SiO<sub>2</sub> (red circle trace) and SiO<sub>2</sub>/P(VDF-HFP) (blue triangle trace) as the gate dielectric layer (200 nm SiO<sub>2</sub> and 150 nm P(VDF-HFP)). The forward and backward scans between 5 V and -60 V of DTS-treated SiO<sub>2</sub> devices show large hysteresis (7.7 V, **Figure 5.1b**) due to a reduction in current in the backward scan as charges are trapped at the dielectric-semiconductor interface. Hysteresis is substantially reduced (0.4 V, **Figure 5.1b**) in devices that contain P(VDF-HFP) as a passivation layer. The maximum current collected from the latter is reduced as a result of

increasing the dielectric layer thickness. To further test electrical stability, a constant gate bias of -60 V together with source-drain bias of -10 V were applied to both sets of devices over the course of 12 hours while monitoring source-drain current (**Figure 5.1c**). Due to a threshold voltage shift caused by hole trapping effects at the interface between the active layer and SiO<sub>2</sub>, a dramatic decrease of 95.4% from the original current is observed in OFETs made using DTS-treated SiO<sub>2</sub> as the gate dielectric.<sup>1</sup> We notice relatively stable current level in SiO<sub>2</sub>/P(VDF-HFP) devices, with currents drop of 36.4% from the original current over 12 hours. The procedure used to passivate SiO<sub>2</sub> using P(VDF-HFP) gives highly reproducible results. **Figure 5.2** and **Table 5.1** demonstrate the transfer curves and device characteristics using different grades of P(VDF-HFP) containing 4, 16 and 32% of HFP monomer cast from solutions of N,N-dimethyl acetamide (DMAc) or methyl ethyl ketone (MEK). (%HFP was determined using <sup>19</sup>F NMR, **Figure 5.3**).

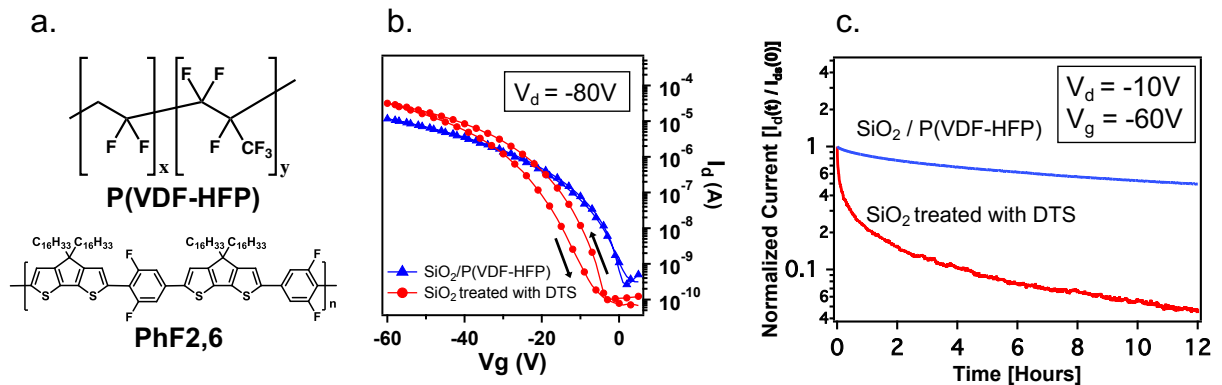


**Figure 5.1.** (a) Chemical structure of P(VDF-HFP) and PhF2,6. (b) Transfer curves of bottom-gate/top-contact devices made using DTS-treated SiO<sub>2</sub> (red circle trace) and SiO<sub>2</sub>/P(VDF-HFP) (blue triangle trace) dielectric layer. The transfer curves were tested in the saturation regime ( $V_d = -80$  V) by sweeping gate voltage ( $V_g$ ) between 5 V and -60 V. (c) Current decay over 12 hours of OFETs made using DTS-treated SiO<sub>2</sub> (red trace) and SiO<sub>2</sub>/P(VDF-HFP) (blue trace) dielectric layers.

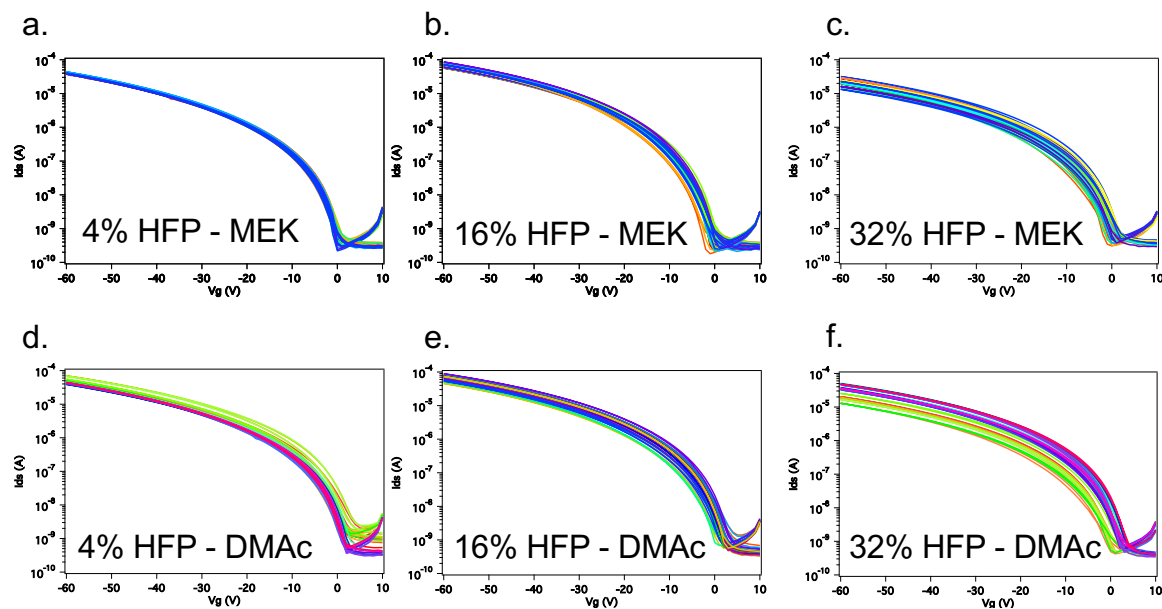


**Figure 5.2.** Transfer curves of bottom-gate/top-contact OFETs made using P(VDF-HFP)/SiO<sub>2</sub> gate dielectric with an applied V<sub>d</sub> = -80V. Devices were fabricated with P(VDF-HFP) cast from 30 mg/mL MEK solutions and contained (a) 4 (b) 16 and (c) 32% HFP monomer or 60mg/mL DMAC solutions and contained (d) 4 (e) 16 and (f) 32% HFP. Each graph contains transfer curves from 20 devices.

**Table 5.1.** Transfer Characteristics of P(VDF-HFP) – SiO<sub>2</sub> OFETs

% HFP monomer	Solvent	Linear Mobility (cm <sup>2</sup> V <sup>-1</sup> s <sup>-1</sup> )	Saturation Mobility (cm <sup>2</sup> V <sup>-1</sup> s <sup>-1</sup> )	Threshold Voltage (V)	Hysteresis (V)	On/Off Current Ratio	Current/Leakage Current Ratio	Reliability Factor (%)
4	DMAc	0.24 ± 0.01	0.28 ± 0.03	-18.2 ± 1.6	0.2 ± 0.5	4.8E4	5.6E5	48
4	MEK	0.21 ± 0.01	0.25 ± 0.01	-20.4 ± 0.3	0.1 ± 0.2	7.8E4	2.7E4	44
16	DMAc	0.30 ± 0.07	0.35 ± 0.07	-17.7 ± 2.0	0.3 ± 0.9	8.0E4	2.6E5	49
16	MEK	0.33 ± 0.04	0.42 ± 0.06	-19.9 ± 1.1	0.4 ± 0.5	1.5E5	1.8E6	45
32	DMAc	0.11 ± 0.05	0.14 ± 0.06	-15.4 ± 1.2	1.0 ± 0.6	4.1E4	1.6E4	54
32	MEK	0.08 ± 0.02	0.11 ± 0.02	-16.1 ± 1.3	1.8 ± 0.6	3.3E4	4.5E4	53

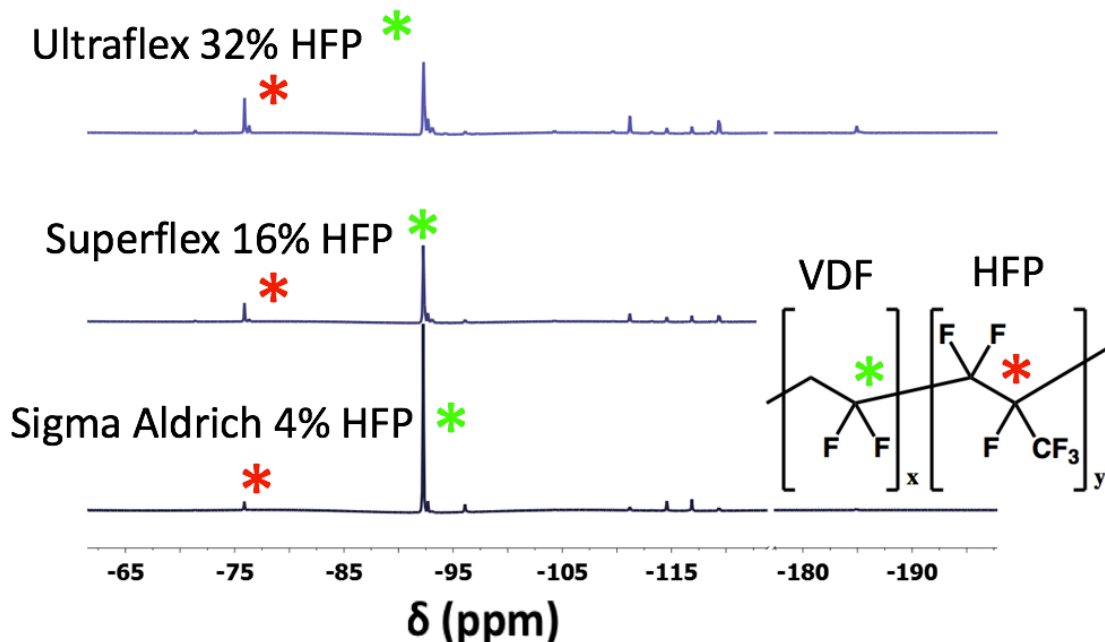


**Figure 5.3.** Fluorine-19 nuclear magnetic resonance ( $^{19}\text{F}$  NMR) spectra used to determine % HFP monomer of P(VDF-HFP) according to the technique described in Wang et al.<sup>17</sup>

### 5.3 Conditions that Dictate Performance in P(VDF-HFP) OFETs

P(VDF-HFP) can effectively and reproducibly be used as a passivation layer, however, the  $\text{SiO}_2$  layer must be removed to take advantage of the high dielectric constant of P(VDF-HFP) ( $\epsilon_r$  of  $\text{SiO}_2 = 3.9$  and  $\epsilon_r$  of P(VDF-HFP) = 10 - 14). A lower voltage is required to operate the device as the dielectric constant of the dielectric layer is increased. Commercially available P(VDF-HFP) materials are not designed for use as a dielectric layer in FETs and are generally used in coating and tubing applications. In this study, five different grades of P(VDF-HFP) with varying ratios of copolymerized VDF and HFP monomer units were used. P(VDF-HFP) containing 4% HFP monomer was purchased from Sigma-Aldrich Corporation (product number 427179), and P(VDF-HFP) containing 16% and 32% HFP were obtained from Arkema (Kynar Superflex® and Kynar Ultraflex®). Dyneon™ FC 2176 and FC 2230, which both

contained 45% HFP, were obtained from 3M™. The surface morphology of films prepared from various grades of P(VDF-HFP) were probed using atomic force microscopy (AFM) in order to determine which film displays the smoothest surface. It has been reported in the literature that surface roughness should be minimized to avoid possible detrimental effects to charge transport in OFETs.<sup>31</sup> Films made from Dyneon™ FC 2176 and FC 2230 P(VDF-HFP) showed the lowest root mean square (RMS) roughness below 0.5 nm (**Figure 5.4**). However, transfer characteristics of bottom-gate/top-contact OFETs made with Dyneon™ FC 2176 and FC 2230 P(VDF-HFP) exhibited non-ideal current-voltage behavior; most notably a large degree of hysteresis between the forward and backward scan (**Figure 5.5**). Dyneon™ FC 2176 and FC 2230 were no longer used for the rest of the study due to the poor transfer characteristics. Bottom-gate/top-contact devices were fabricated using just P(VDF-HFP) (Ultraflex®, 32% HFP) as the gate dielectric layer. Upon examining the transfer characteristics of those devices, certain processing conditions exhibited an increase in current in the backward scan relative to the forward scan (hysteresis). This type of hysteresis is a possible sign of double-layer capacitance or ferroelectricity in the dielectric layer and should be avoided in FETs.<sup>32</sup> The ferroelectric behavior of PVDF copolymers are heavily dependent on the building block co-polymerized with VDF. In this context, poly(vinylidene fluoride-trifluoroethylene) (P(VDF-TrFe)) crystallizes into a highly ferroelectric film that has been used to fabricate organic memory devices.<sup>15,33,34</sup> In contrast, the crystalline structure of P(VDF-HFP) films spun from solution has relatively minimal ferroelectric properties, and the degree of ferroelectricity heavily depends on processing conditions.<sup>35</sup> The ferroelectric behavior of P(VDF-HFP) was confirmed using a modified Sawyer-Tower circuit (**Figure 5.6**).<sup>36,37</sup> Ferroelectricity is quantified by plotting the polarization ( $\text{mC/m}^2$ ) versus the electric field ( $\text{MV/m}$ ) to determine

the remnant polarization ( $P_r$ ) (the polarization at zero electric field). P(VDF-HFP) shows the s-shaped curve attributed to ferroelectric behavior, compared to the linear behavior of an ideal capacitor. The Sawyer-Tower circuit consists of a capacitor made of the material of interest and a high capacitance “sense” capacitor hooked up in series. The difference in the voltage on either side of the measured capacitor was measured over time using an oscilloscope set to XY mode. Ferroelectricity is quantified by plotting the polarization ( $\text{mC/m}^2$ ) versus the electric field ( $\text{MV/m}$ ). There are two main figures of merit when analyzing polarization vs. electric field plots. Remnant polarization ( $P_r$ ) refers to the polarization at zero electric field, and coercive field ( $E_c$ ) is the minimum field required to fully reverse ferroelectric polarization.

P(VDF-HFP) bottom-gate/top-contact device performance was dependent on the solvent used to cast the dielectric layer, where those casted from N,N-dimethyl acetamide (DMAc) showed the most ideal transfer characteristics relative to devices processed using methyl ethyl ketone (MEK). Devices were also fabricated using acetone, however the film thickness was not uniform, so the solvent was abandoned. **Figure 5.7** reveals the effect of solvent choice on the transfer characteristics of devices fabricated with a P(VDF-HFP) dielectric layer spun from solutions of either MEK (blue triangles) or DMAc (red circles) after the whole device was annealed at 160 °C. The results show the importance of solvent choice when fabricating OFETs containing P(VDF-HFP) as the gate dielectric layer. The device containing P(VDF-HFP) cast from MEK shows hysteresis between the forward and backward scan in the form of an increase in the current in the backward scan. The device shows behavior that is more similar to organic memory devices.<sup>15,33,34</sup> Devices containing P(VDF-HFP) cast from DMAc solutions, on the other hand, show virtually no hysteresis between the forward and backward scans. This behavior may be related to the higher boiling point of DMAc (165

°C) relative to MEK (80 °C). DMAc remains in the film for a longer time after casting and annealing the film, affecting the crystallinity of the dielectric layer.<sup>35</sup> The difference in the crystalline phase of P(VDF-HFP) cast from a MEK or DMAc solution is observed by FTIR (**Figure 5.8**). In films cast from a solution of MEK and annealed at 180°C for 1 hour, a prominent peak at 760 cm<sup>-1</sup> corresponding to  $\alpha$ -phase P(VDF-HFP) is present. This peak does not appear in annealed films cast from solutions of DMAc. Although a difference in hysteresis is observed between films cast from either solvent, we did not observe a difference in the dielectric constant. The dielectric constant of P(VDF-HFP) (32% HFP) films cast from DMAc and MEK were measured by impedance spectroscopy to be  $11.0 \pm 0.1$  and  $11.0 \pm 0.8$ , respectively (**Table 5.2**). When annealing the as cast device at 80 °C, mobility ( $\mu$ ) is immediately increased from 0.0052 to 0.38 cm<sup>2</sup> V<sup>-1</sup> s<sup>-1</sup> and increases further to 0.44 cm<sup>2</sup> V<sup>-1</sup> s<sup>-1</sup> when annealing at 160 °C. There is a dramatic change in the on/off ratio of the device from  $7.4 \times 10^2$  to  $4.3 \times 10^5$  when the device is annealed from 80 °C to 160 °C as well as a reduction in hysteresis from 12.2 V to 3.4 V (**Figure 5.7b**). These results are consistent with previous reports in the literature. A change in mobility is commonly observed in organic electronic materials upon thermal annealing due to a change in film morphology of the active layer. A change in the surface topography of PhF2,6 on top of P(VDF-HFP) (32% HFP) before and after annealing at 160°C is observed by AFM (**Figure 5.9**). This suggests a change in the film morphology of PhF2,6 after annealing. An increase in the hole mobility of OFETs made with PhF2,6 upon annealing has been reported in previous work.<sup>29,30</sup> GIWAXS diffraction peaks sharpened after annealing at 200 °C, which suggests an improvement in molecular packing.

An advantage of P(VDF-HFP) is its solubility in polar solvents, which can be utilized to fabricate top-gate and bottom-gate architectures using orthogonal solvents. In addition, the

surface energy of P(VDF-HFP) (16.5 to 27.1 mN m<sup>-1</sup>) is high enough to wet the surface in many cases to form a film. This is not the case for Cytop™, which is limited to top-gate architectures due to its low surface energy (14.4 mN m<sup>-1</sup>). **Figure 5.7c** shows the transfer characteristics of top-gate/bottom-contact devices using a 300 nm thick P(VDF-HFP) (32% HFP) dielectric layer. Results indicate an on/off ratio of  $1.6 \times 10^3$  between 0 and -10 V<sub>g</sub> and an applied V<sub>d</sub> = -5 V and a mobility of 0.38 cm<sup>2</sup> V<sup>-1</sup> s<sup>-1</sup>. This transfer curve highlights the advantage of using a gate dielectric material with a relatively high dielectric constant. Top-gate/bottom-contact devices were fabricated using 300 nm Cytop, to show that the absolute current of devices made with P(VDF-HFP) is greatly increased relative to devices containing Cytop™ of similar thickness (**Figure 5.10**). The top-gate/bottom-contact devices were biased with a constant V<sub>g</sub> = -40 V and V<sub>d</sub> = -5 V over 12 hours while monitoring source-drain current (**Figure 5.7d**). We observed an increase in current due to polarization of C-F bonds in the P(VDF-HFP) layer when initially biasing the device, followed by a stable current level. There is an overall increase in current of 91% relative to the initial current. This is the same behavior observed in devices fabricated with a Cytop™ dielectric layer, where an initial increase is observed when biasing the device.<sup>38</sup> The authors associate the increase in current to the presence of dipoles that can be oriented in the gate dielectric.

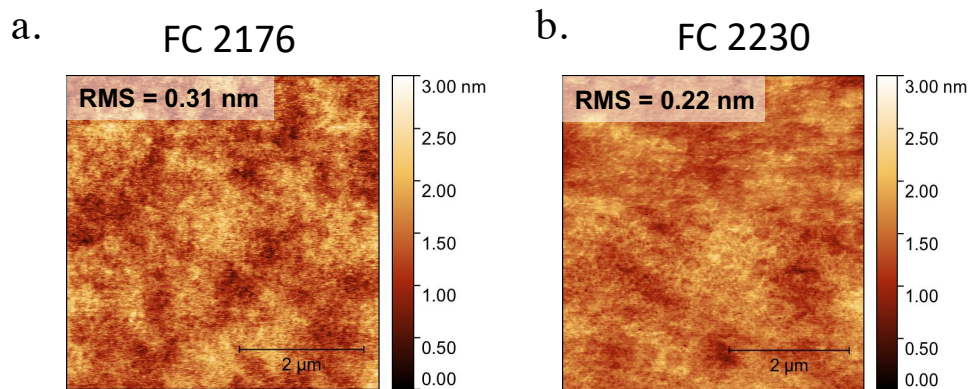


**Figure 5.4.** AFM morphology of 3M Dyneon™ FC 2176 and 3M Dyneon™ FC 2230 annealed at 120°C.

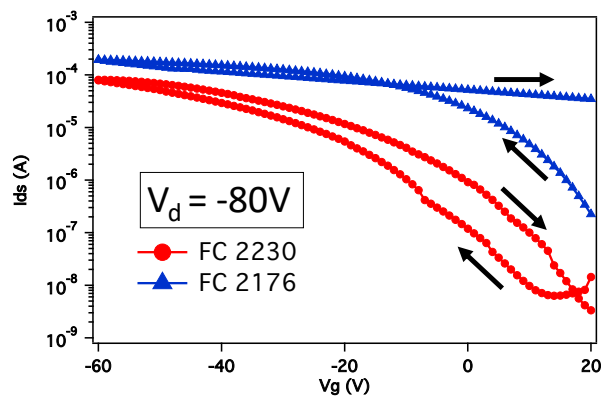


**Figure 5.5.** Transfer characteristics of bottom-gate/top-contact OFETs made using Dyneon™ FC 2176 and FC 2230 P(VDF-HFP) gate dielectric. Devices were annealed at 120°C for 1 hour.

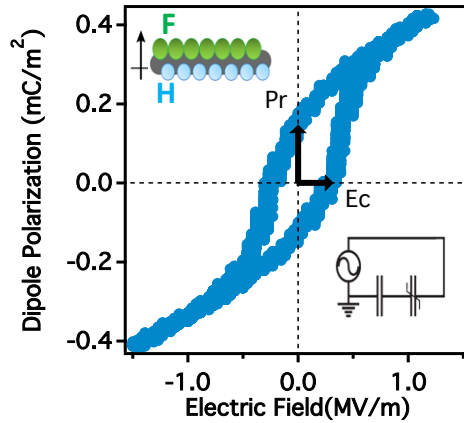


**Figure 5.6.** Polarization versus electric field of a capacitor fabricated with P(VDF-HFP) in between a highly-doped silicon electrode and an aluminum electrode. Inset shows PVDF structure and diagram of a Sawyer-Tower circuit.

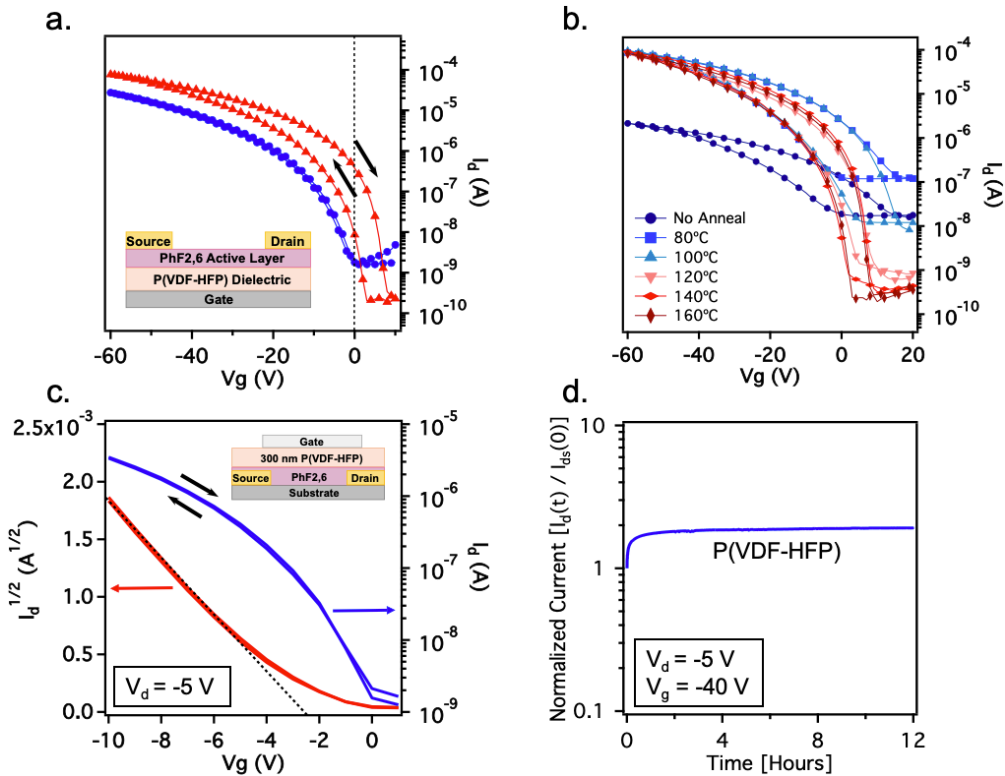


**Figure 5.7.** (a) Transfer characteristics of bottom-gate/top-contact devices comprised of a P(VDF-HFP) dielectric layer spun from either MEK (red triangles) or DMAc (blue circles) solutions. Transfer characteristics were tested in the saturation regime ( $V_d = -80$  V) by sweeping  $V_g$  between 10 V and -60 V. (b) Transfer curve of device as cast from MEK and annealed from 80°C to 160°C. (c) Transfer characteristics of a top-gate/bottom-contact device made using P(VDF-HFP) dielectric layer ( $V_d = -5$  V). (d) Current decay over 12 hours of top-gate/bottom-contact OFETs made using P(VDF-HFP) (blue trace).

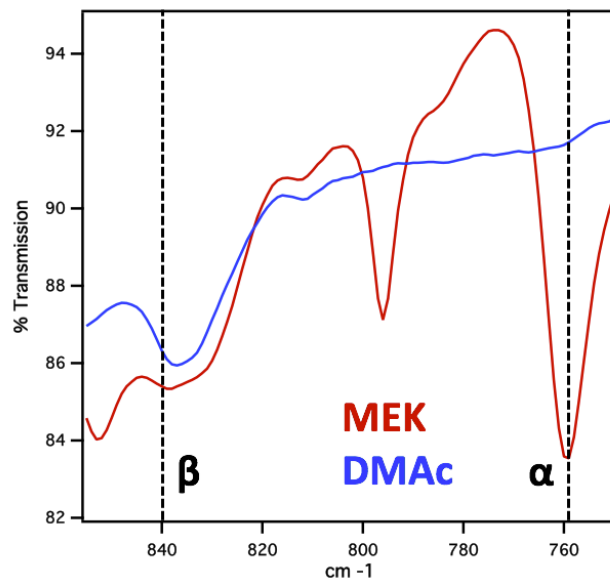


**Figure 5.8.** FTIR spectra of films cast from MEK (red trace) and DMAc (blue trace) and annealed at 180°C for 1 hour. The film cast from MEK shows a more pronounced peak at 760  $\text{cm}^{-1}$ , corresponding to  $\alpha$ -phase P(VDF-HFP). The peak at 840  $\text{cm}^{-1}$  corresponds to  $\beta$ -phase P(VDF-HFP).

**Table 5.2.** Dielectric Constant of Kynar Ultraflex P(VDF-HFP) Cast from Various Solvents

Solvent	Dielectric Constant
Acetone	11.3 $\pm$ 0.9
Methyl Ethyl Ketone	11.0 $\pm$ 0.8
N,N- Dimethylacetamide	11.0 $\pm$ 0.1

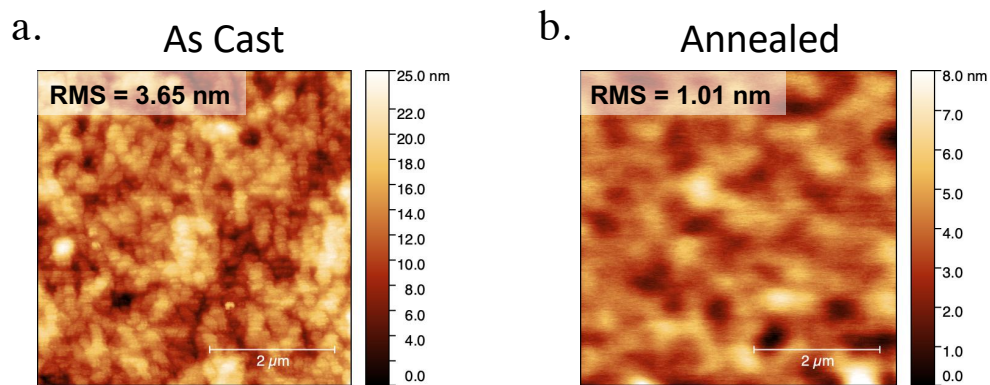


**Figure 5.9.** AFM topography of PhF<sub>2,6</sub> on top of P(VDF-HFP) (32% HFP) (a) as cast and (b) annealed at 160°C.

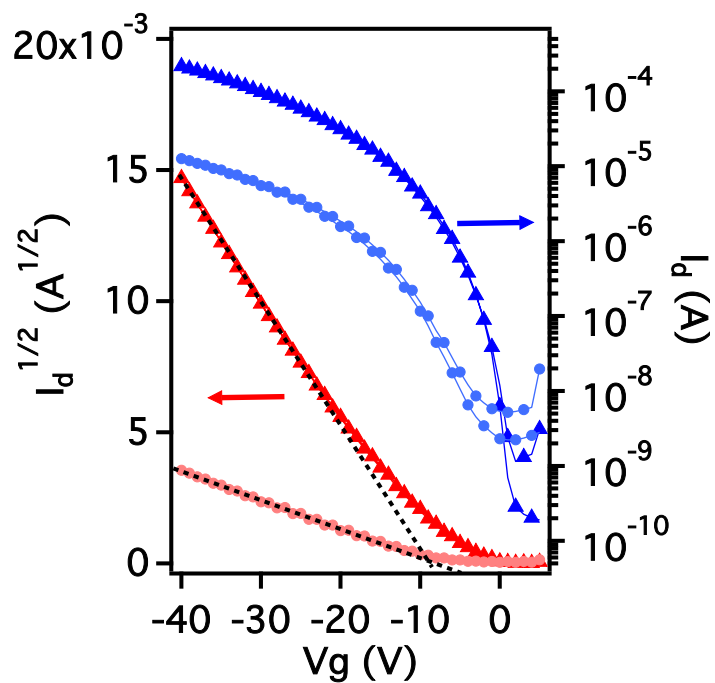


**Figure 5.10.** Transfer characteristics of top-gate/bottom-contact devices made using P(VDF-HFP) (blue triangle) or Cytop (light blue circle) dielectric layer ( $V_d = -30V$ ).

## 5.4 Exploring the Effect of HFP Monomer Content on Charge Transport

In addition to exploring the effects of solvent and annealing conditions on device performance, we were interested in understanding the impact of the percent of HFP monomer on the transfer characteristics of devices fabricated with P(VDF-HFP). The HFP building block is amorphous, which results in a decrease in crystallinity when it is copolymerized with VDF to form P(VDF-HFP).<sup>35,39</sup> P(VDF-HFP) is known to become rubbery and exhibit conformable and stretchable mechanical properties as the ratio of HFP monomer is increased, which makes it a candidate for flexible electronics and OFET driven pressure sensor applications.<sup>18</sup> **Table 5.3** of the supporting information lists the elongation break and flexural modulus of the P(VDF-HFP) materials used in this study. For this reason, it is important to closely examine the effect of % HFP on device performance. Commercially available P(VDF-HFP) comprised of 4%, 16% and 32% HFP were obtained for this study. Atomic force microscopy (AFM) images of P(VDF-HFP) (**Figure 5.11a-c**) indicated dramatic changes in film morphology with a change in the percentage of HFP building block, where increasing its content reduces the size of crystalline domains as well as the root mean square (RMS) roughness from 17.3 to 11.4 nm. Molecular weight, surface energy, melting point, dielectric constant and dielectric strength are reported in **Table 5.4**. It summarizes materials characterization data collected from 5 grades of P(VDF-HFP) that were obtained for this study to determine their ability to make a smooth and homogenous films that exhibits a low degree of ferroelectricity. With NMR analysis, we were able to determine the percentage of HFP monomer in the P(VDF-HFP) copolymers.<sup>5</sup> The average molecular weight (g/mol) was determined by gel permeation chromatography (GPC) and the melting point was determined by differential scanning calorimetry (DSC). Surface

energy was calculated with contact angle measurements using the Owens, Wendt, Rabel and Kaeble (OWRK) method.<sup>6,7</sup> The dielectric constants of P(VDF-HFP) capacitors were measured using a Solartron SI 1260 impedance analyzer. The dielectric strength of P(VDF-HFP) was determined by preparing thin film capacitors of P(VDF-HFP) between thermally evaporated metal crossbars. Measurements were made with a Keithley semiconductor parametric analyzer (model 4200-SCS) by applying increasing voltage levels until failure. **Table 5.5** summarizes the transfer characteristics of bottom-gate/top-contact devices that were fabricated using optimal processing conditions made with three commercially available grades of P(VDF-HFP) of 4, 16 and 32% HFP. Their transfer curves are presented in the **Figure 5.12**. An increase in linear mobility is observed from 0.27 to 1.02 cm<sup>2</sup> V<sup>-1</sup> s<sup>-1</sup> when % HFP is increased from 4 to 16%, followed by a slight drop in mobility to 0.61 cm<sup>2</sup> V<sup>-1</sup> s<sup>-1</sup> as % HFP is further increased to 32%. The saturation mobility is similar in magnitude to the linear mobility, and follows the same trend of increasing from 0.31 to 1.02 cm<sup>2</sup> V<sup>-1</sup> s<sup>-1</sup> followed by a drop to 0.79 cm<sup>2</sup> V<sup>-1</sup> s<sup>-1</sup> when increasing % HFP from 4 to 16 and 32%. By extrapolating the slope of square root of current ( $I_d^{1/2}$ ) versus  $V_g$  from -45 V to -60 V to the x-axis, we extract the threshold voltage ( $V_T$ ). Due to the gradual upward slope of  $I_d^{1/2}$  versus  $V_g$ , value  $V_T$  is negative and large in magnitude (-20.6 to -12.4 V). The reason for the upward slope of  $I_d^{1/2}$  versus  $V_g$  will be discussed below. Hysteresis is uniformly low between all three types of devices, with values ranging from 5 to 7 V. Devices fabricated with P(VDF-HFP) consisting of 4 and 16% HFP have an on/off ratio between 4 and almost 5 orders of magnitude, respectively. The on/off ratio drops to below 4 orders of magnitude when % HFP is increased to 32% due to the increased current level in the “off” state. The leakage current measured for all devices is two orders of magnitude lower than the source-drain current. The best transfer characteristics are observed

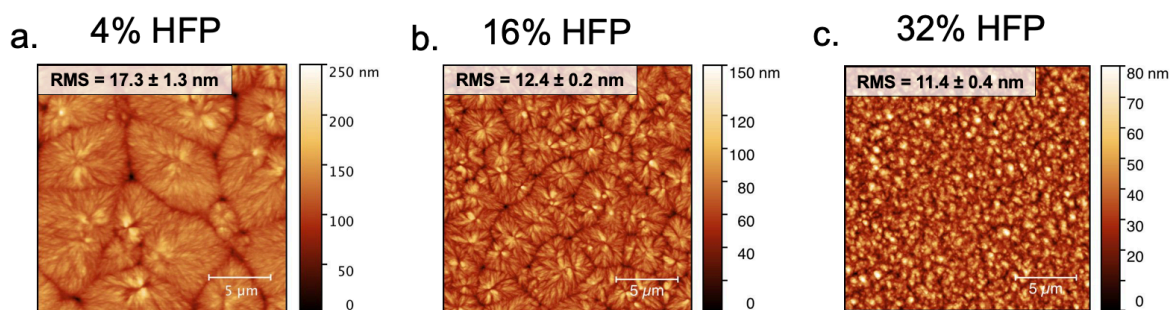
when utilizing P(VDF-HFP) that contains 16% HFP monomer, however the reason for this is unclear. The reliability factor, a value used to quantify how closely a device matches an ideal current-voltage relationship, will be discussed in the paragraph below.<sup>40</sup>

Plots of the square root of current as a function of gate voltage ( $V_g$ ) for the investigated polymers (**Figure 5.13a-c**) shows an increase in the slope as the  $V_g$  increases, and do not follow the transfer characteristics of the standard Shockley FET equations.<sup>41</sup> The dotted line represents the slope used to calculate the maximum value of mobility of these devices, and the solid line indicates the slope of an FET with mobility that is  $V_g$  independent and exhibits the same conductivity at the maximum  $V_g$ . By comparing the values of these two slopes, we have calculated the reliability factor, a term which has been used to quantify the deviation of the transfer characteristics from linear dependence of  $I_d^{1/2}$  and  $V_g$ .<sup>41</sup> Transfer characteristics that are closer to ideal linear dependence of  $I_d^{1/2}$  and  $V_g$  will have a larger reliability factor. As the percentage of HFP monomer is increased from 4 to 32%, a higher reliability factor (increasing from 43 to 59%) and a weaker dependence of the  $\mu$  on  $V_g$  is observed. By plotting the average  $\mu$  versus  $V_g$  of devices fabricated with 4, 16 and 32 % HFP in a semi-log scale, we can see a reduction in the  $V_g$  dependence of  $\mu$  with increasing % HFP (**Figure 5.13d-f**). This trend is also observed in devices fabricated on  $\text{SiO}_2/\text{P(VDF-HFP)}$  with another p-type semiconducting polymer active layer (**Figure 5.14, 5.15 and Table 5.6**) as well as devices containing P(VDF-HFP) cast on top of  $\text{SiO}_2$  dielectric layers (**Figure 5.2**). We believe that the observed nonlinear dependence of  $I_d^{1/2}$  and  $V_g$  is a convolution of energetic disorder at the semiconductor-dielectric interface and polarization of the dielectric layer.<sup>31,42</sup> In the former case, disorder may arise from kinks and bends in the semiconductor backbone caused by dielectric surface roughness and dipolar disorder at the interface.<sup>31</sup> Atomic force microscopy (AFM) images of P(VDF-

HFP) (**Figure 5.11a-c**) indicated a decrease in RMS roughness as the percentage of the HFP building block increased from 17.3 to 11.4 nm. Although there is a reduction in surface roughness, a RMS roughness value greater than 0.5 nm has shown significant morphological changes in the active layer in pBTTT based OFETs.<sup>31</sup> This effect of surface roughness is compounded with disorder caused by high-k dielectric materials. The dipolar disorder of strong dipoles, such as a C-F bond, is attributed to a larger  $V_g$  dependence of  $\mu$ .<sup>43,44</sup> Disorder in semiconducting polymer films caused by surface roughness and dipolar disorder at the dielectric-semiconductor interface may result in a broadening of the density of states (DOS).<sup>45,46</sup> At lower charge carrier concentrations, charges injected into the DOS relax to the tail states, where polarons are highly localized and mobility is relatively low. As  $V_g$  is increased, tail states are filled and charges can access more delocalized states, allowing for higher mobility transport. In the case of materials such as P(VDF-HFP) or Cytop™, the dependence of  $\mu$  on  $V_g$  is affected by polarization of the dielectric layer in an electric field. Applying a constant  $V_g$  and  $V_d$  reveals an initial increase in current in the first minutes of biasing the device (**Figure 5.7d**). This same behavior is observed in the literature with devices fabricated from Cytop™, which present an increase in current over time when the device is constantly biased as well as an increase in  $\mu$  with increasing  $V_g$ .<sup>37</sup> The  $V_g$  dependent  $\mu$  of these devices can make it challenging to extract a mobility value that represents the intrinsic value of the semiconducting material. However, in cases where low voltage operation and electrical stability is a priority, P(VDF-HFP) is an excellent choice for a dielectric layer. The flexible and stretchable properties of P(VDF-HFP) makes it ideal for technologies such as wearable electronics and pressure sensors, and further research into this class of materials is warranted.

**Table 5.3.** Mechanical Properties of P(VDF-HFP)

Vendor	Product	Elongation Break (%)	Flexural Modulus (psi)
3M™	FC 2176	240 <sup>2</sup>	2175 <sup>2</sup>
3M™	FC 2230	165 <sup>3</sup>	1995 <sup>3</sup>
Sigma Aldrich™	427179	-	-
Arkema	Kynar® Superflex 2500	500 – 800 <sup>4</sup>	28,000 – 40,000 <sup>4</sup>
Arkema	Kynar® Ultraflex B	500 – 1000 <sup>4</sup>	10,000 – 20,000 <sup>4</sup>

**Figure 5.11.** AFM morphology of P(VDF-HFP) consisting of (a) 4% (b) 16% and (c) 32% HFP monomer units exhibited a dramatic change in morphology.**Table 5.4** Material Characterization of P(VDF-HFP)

Vendor	Product	HFP Content (%)	MW (kDa)	Melting Point (°C)	Surface Energy (mN/m)	Dielectric Constant	Thickness (nm)	Capacitance (nF cm <sup>-2</sup> )	Dielectric Strength (MV m <sup>-1</sup> )
3M™	FC 2176	45	-	-	25.94	14.71	1285	10.1	-
3M™	FC 2230	45	-	-	22.74	11.92	1280	8.3	-
Sigma Aldrich™	427179	4	455	155-160	27.13	10.37	850	10.9	232.2
Arkema	Kynar® Superflex 2500	16	337	124.3	21.2	9.54	615	13.7	356.6
Arkema	Kynar® Ultraflex B	32	428	108.0	16.5	11.06	625	15.7	333.8

**Table 5.5.** Transfer Characteristics of P(VDF-HFP) OFETs

Percent HFP (%)	Linear Mobility ( $\text{cm}^2 \text{V}^{-1} \text{s}^{-1}$ ) <sup>a</sup>	Saturation Mobility ( $\text{cm}^2 \text{V}^{-1} \text{s}^{-1}$ ) <sup>b</sup>	Threshold Voltage (V)	Hysteresis (V)	$I_g/I_d$	On/Off Ratio	Reliability Factor (%)
4	$0.27 \pm 0.08$	$0.31 \pm 0.09$	$-20.6 \pm 0.7$	$5.1 \pm 0.8$	$4.7 \times 10^{-2}$	$2.6 \times 10^4$	43
16	$1.02 \pm 0.13$	$1.2 \pm 0.07$	$-16.6 \pm 1.6$	$6.7 \pm 0.9$	$1.7 \times 10^{-2}$	$8.8 \times 10^4$	53
32	$0.61 \pm 0.23$	$0.79 \pm 0.21$	$-12.4 \pm 2.5$	$5.5 \pm 1.7$	$5.8 \times 10^{-2}$	$7.6 \times 10^3$	59

<sup>a,b</sup> Mobility values were calculated with the slope from -45 to -60 V

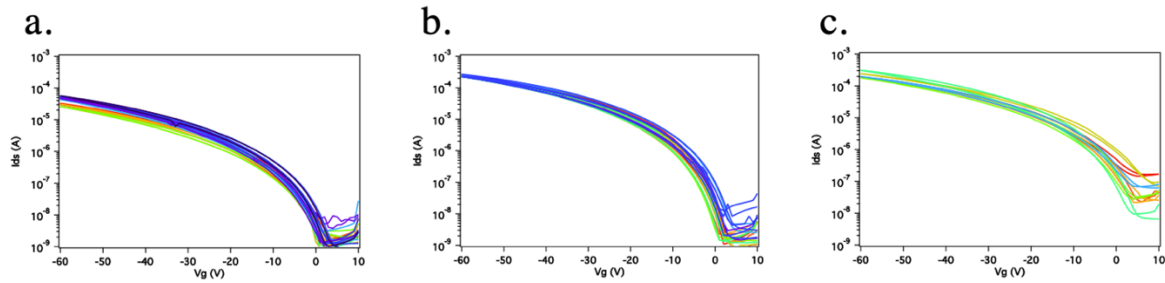


**Figure 5.12.** Transfer characteristics of bottom-gate/top-contact OFETs made using P(VDF-HFP) gate dielectric ( $V_d = -80\text{V}$ ). Devices were fabricated with P(VDF-HFP) cast from 120 mg/mL DMAc solutions and contained (a) 4 (b) 16 and (c) 32% HFP monomer.

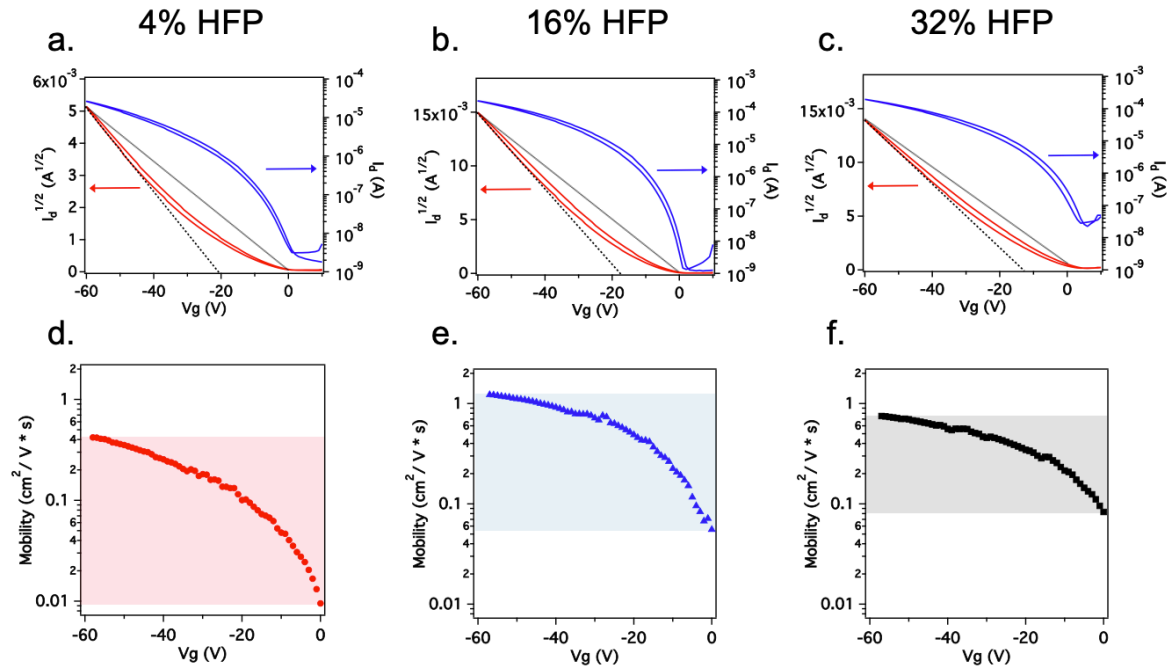


**Figure 5.13.** Transfer characteristics of bottom-gate/top-contact devices fabricated with (a) 4% (b) 16% and (c) 32% HFP revealed an increase in  $V_g$  dependence of mobility with an increase in % HFP. The dotted line represents the slope used to calculate mobility. The solid line indicates the slope of a FET with mobility that is  $V_g$  independent and exhibits the same conductivity at the maximum  $V_g$ . Transfer characteristics were tested in the saturation regime ( $V_d = -80$  V) by sweeping  $V_g$  from 10 V to -60 V to 10 V. Mobility versus  $V_g$  of devices made with (d) 4% (red circles) (e) 16% (blue triangles) and (f) 32% HFP (black squares) further highlight decrease in gate voltage dependence with increasing % HFP.

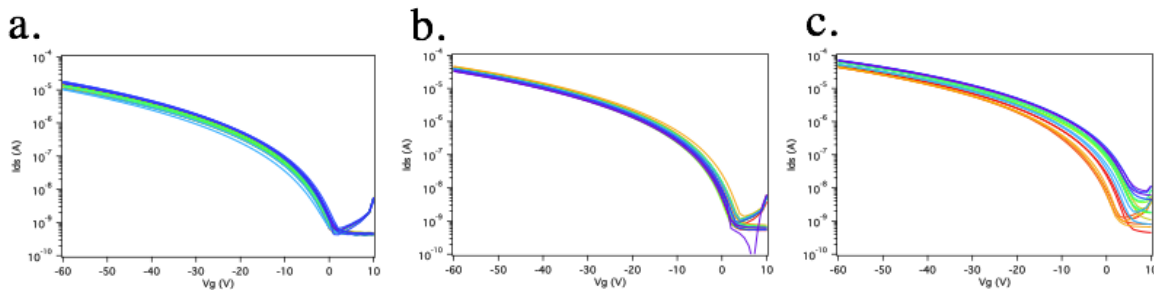


**Figure 5.14.** Transfer curves of bottom-gate/top-contact OFETs made using P(VDF-HFP) – SiO<sub>2</sub> bilayer gate dielectric with P(VDF-HFP) cast from 60 mg/mL DMAc solutions and contained (a) 4 (b) 16 and (c) 32% HFP monomer. PhF2,3, a p-type polymer, was used as the active layer. Each graph contains transfer curves from 10 devices ( $V_d = -80$  V).

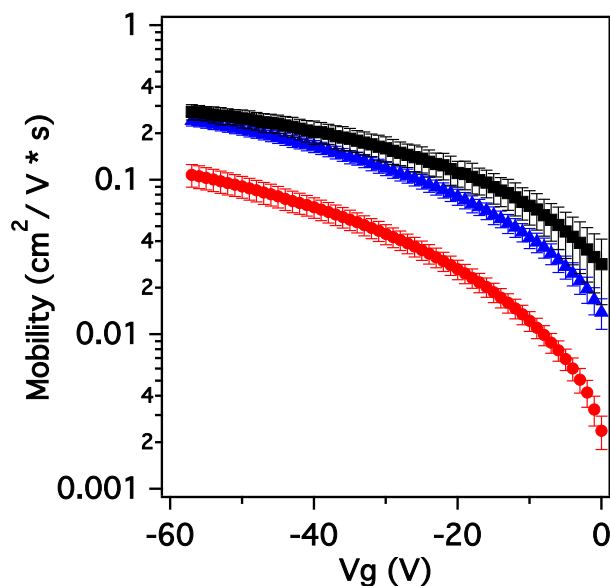


**Figure 5.15.** Average and standard deviation of mobility versus  $V_g$  of devices made with 4% (red circles) 16% (blue triangles) and 32% HFP (black squares) further highlight decrease in gate voltage dependence with increasing %HFP. Devices tested are bottom-gate/top-contact OFETs made using P(VDF-HFP) – SiO<sub>2</sub> bilayer gate dielectric with P(VDF-HFP) cast from 60 mg/mL DMAc solutions and PhF<sub>2,3</sub> as the active layer.

**Table 5.6** Device Characteristics of OFETs with PhF<sub>2,3</sub> Active Layer and P(VDF-HFP) Dielectric

Percent HFP (%)	Linear Mobility (cm <sup>2</sup> /V*s) <sup>a</sup>	Saturation Mobility (cm <sup>2</sup> /V*s) <sup>b</sup>	Threshold Voltage (V)	Hysteresis (V)	On/Off Ratio	I <sub>g</sub> /I <sub>d</sub>	Reliability Factor (%)
4	0.084 ± 0.013	0.096 ± 0.014	-20.5 ± 0.5	1.0 ± 0.9	1.8E4	3E-5	43
16	0.156 ± 0.049	0.220 ± 0.016	-17.4 ± 0.6	0.8 ± 0.2	4.4E4	3.4E-7	49
32	0.182 ± 0.046	0.260 ± 0.029	-13.8 ± 2.5	1.6 ± 1.5	1.8E4	6.5E-5	56

<sup>a,b</sup> Mobility values were calculated with the slope from -45 to -60 V

## 5.5 Conclusions

In conclusion, we have shown that P(VDF-HFP) can be used as a dielectric material to give electrically stable OFETs. A thin film of P(VDF-HFP) can be easily deposited by spin

coating on the surface of SiO<sub>2</sub> to fabricate devices that show no hysteresis and retain a high level of current when biased over extended periods of time. P(VDF-HFP) passivated devices show consistently positive results, making it a reliable alternative to more difficult passivation techniques, such as using SAMs. P(VDF-HFP) is soluble in polar solvents, meaning that the fabrication of top-gate architecture devices is possible due to their orthogonality to solvents used to dissolve many common semiconducting materials. We demonstrated that the exceptionally high dielectric constant of P(VDF-HFP) makes it possible to fabricate devices that operate at low bias voltages. Care must be taken to choose the correct material source and processing conditions to avoid unfavorable ferroelectric behavior that can lead to hysteresis between forward and backward transfer curve scans. The best performance and lowest degree of ferroelectricity was observed when DMAc was used as the solvent. In all cases, mobility and on/off ratio was increased and hysteresis was reduced when devices were annealed to at least 80°C and transfer characteristics continued to improve when annealing to 160°C. We demonstrated that devices made using P(VDF-HFP) as a gate dielectric layer exhibit an increase in gate voltage dependence of mobility with an increase in % HFP. This behavior is suggested to be caused by a combination of disorder at the semiconductor-dielectric interface and slight polarization of the dielectric layer. P(VDF-HFP), with the right processing conditions presented in this work, is shown to be a strong candidate for application in devices where low voltage operation, flexibility, low cost and electrical stability is called for.

## 5.6 Experimental Methods

*PhF2,6 Preparation:* PhF2,6, a high mobility p-type D-A semiconducting polymer based on 4,4-dihexadecyl-4H-cyclopenta[1,2-b:5,4-b']dithiophene (CDT) and 2,6-difluorophenylene (2,6-DFPh), was synthesized following the procedure previously reported.<sup>29</sup>

*Device Preparation:* Bottom-gate/top-contact devices were fabricated on 700  $\mu\text{m}$  thick highly antimony n-doped Si substrates with 200 nm thick  $\text{SiO}_2$ . The substrates were cleaned in a piranha solution (3:1  $\text{H}_2\text{SO}_4:\text{H}_2\text{O}_2$ ) and rinsed with deionized water. Gate electrodes were thermally evaporated using 30 nm Au on top of a 1 nm thick Cr adhesion layer. The patterned substrates were cleaned by sonication in acetone followed by isopropyl alcohol. Upon drying in an oven, the substrates were treated in a UV- $\text{O}_3$  cleaner. Cleaned substrates were then transferred into a nitrogen glovebox for spin coating the dielectric layer. 120  $\text{mg mL}^{-1}$  solutions of P(VDF-HFP) in DMAc or 80  $\text{mg mL}^{-1}$  solutions in MEK were prepared the day before and were left in a nitrogen atmosphere overnight at 80  $^\circ\text{C}$ . Solutions were spun at 1,500 rpm for 1 minute and annealed in the glove box at 85  $^\circ\text{C}$  for 15 minutes and 180  $^\circ\text{C}$  for 30 minutes to give a 600 to 800 nm thick film. PhF2,6 active layer was spun at 2,000 rpm and annealed at 85  $^\circ\text{C}$  for 15 minutes in the glove box. 50 nm thick Au contact were deposited via thermal evaporation. Devices were annealed at 160  $^\circ\text{C}$  for 20 minutes before testing.

Bottom-gate/top-contact devices containing a P(VDF-HFP)/ $\text{SiO}_2$  dielectric layer were fabricated on 700  $\mu\text{m}$  thick highly antimony n-doped Si substrates with 200 nm thick  $\text{SiO}_2$ . The substrates were cleaned by the previously described procedure. Cleaned substrates were then transferred into a nitrogen glovebox for spin coating the dielectric layer. P(VDF-HFP) solutions (30  $\text{mg mL}^{-1}$  in DMAc) were spun at 1,500 rpm for 1 minute and annealed in the

glove box to give a 60-80 nm thick film. PhF<sub>2,6</sub> active layer was spun at 2,000 rpm and annealed in the glove box at 85 °C for 15 minutes and 180 °C for 30 minutes. 50 nm thick Au contact were deposited via thermal evaporation. Contact to the gate electrode was made by scratching away to the underlying highly doped silicon substrate with a diamond scribe. Devices were annealed at 160 °C for 20 minutes before testing.

Top-gate/bottom-contact devices were fabricated on 500 μm thick Si substrates with 200 nm thick SiO<sub>2</sub>. The substrates were cleaned in a piranha solution (3:1 H<sub>2</sub>SO<sub>4</sub>:H<sub>2</sub>O<sub>2</sub>) and rinsed with deionized water. Source and drain electrodes were thermally evaporated using 30 nm Au on top of a 1 nm thick Cr adhesion layer. The patterned substrates were cleaned by the previously described procedure. The surface of the substrates was passivated by decyltrichlorosilane (DTS) in a 1 vol% toluene solution at 85 °C for 25 minutes in a nitrogen environment. Substrates were rinsed twice in toluene and transferred into glove box for spin coating. PhF 2,6 active layer were spun at 2,000 rpm and annealed in the glove box. In the cases where P(VDF-HFP) was used as the gate dielectric, films were blade coated at a blade angle of 30°, a temperature of 70 °C, a blade speed of 1 mm/s and a solution concentration of 40 mg mL<sup>-1</sup> in DMAc and gave a film thickness of 300 to 400 nm. In the cases where Cytop™ was used as the gate dielectric, solutions were deposited using the spin coating method at 2,000 rpm for 1 minute and annealed at 80 °C for 15 minutes.

*Electrical Characterization:* All electrical measurements were made using a Keithley semiconductor parametric analyzer (model 4200-SCS) and probe station in a nitrogen environment.

*Dielectric Characterization:* The dielectric constants of P(VDF-HFP) capacitors were measured using a Solartron SI 1260 impedance analyzer. The dielectric strength of P(VDF-

HFP) was determined by preparing thin film capacitors of P(VDF-HFP) between thermally evaporated metal crossbars. Measurements were made with a Keithley semiconductor parametric analyzer (model 4200-SCS) by applying increasing voltage levels until failure.

*Polarization Characterization:* Polarization versus electric field measurements were made using a modified Sawyer-Tower Circuit.<sup>35,36</sup> Capacitors of P(VDF-HFP) were tested using with a sinusoidal AC voltage at a frequency between 10-100 Hz. A 2.2 nF “sense” capacitor and a Teledyne Lecroy Waveace 2034 oscilloscope set to XY mode was used.

*Surface Energy Characterization:* The surface free energy of the solid of films made from P(VDF-HFP) were determined using the Owens, Wendt, Rabel and Kaeble Method.<sup>47,48</sup>

## 5.7 References

1. Matters, M.; de Leeuw, D. M.; Herwig, P. T.; Brown, A. R. Bias-Stress Induced Instability of Organic Thin Film Transistors. *Synth. Met.* **1999**, *102*, 998–999.
2. Mathijssen, S. G. J.; Cölle, M.; Gomes, H.; Smits, E. C. P.; de Boer, B.; McCulloch, I.; Bobbert, P. A.; de Leeuw, D. M. Dynamics of Threshold Voltage Shifts in Organic and Amorphous Silicon Field-Effect Transistors. *Adv. Mater.* **2007**, *19*, 2785–2789.
3. Sirringhaus, H. Reliability of Organic Field-Effect Transistors. *Adv. Mater.* **2009**, *21*, 3859–3873.
4. Lee, W. H.; Choi, H. H.; Kim, D. H.; Cho, K. 25th Anniversary Article: Microstructure Dependent Bias Stability of Organic Transistors. *Adv. Mater.* **2014**, *26*, 1660–1680.
5. Phan, H.; Wang, M.; Bazan, G. C.; Nguyen, T.-Q. Electrical Instability Induced by Electron Trapping in Low-Bandgap Donor–Acceptor Polymer Field-Effect Transistors. *Adv. Mater.* **2015**, *27*, 7004–7009.

6. Phan, H.; Ford, M. J.; Lill, A. T.; Wang, M.; Bazan, G. C.; Nguyen, T.-Q. Electrical Double-Slope Nonideality in Organic Field-Effect Transistors. *Adv. Funct. Mater.* **2018**, *28*, 1707221.
7. Don Park, Y.; Lim, J. A.; Lee, H. S.; Cho, K. Interface Engineering in Organic Transistors. *Mater. Today* **2007**, *10*, 46–54.
8. Kalb, W. L.; Mathis, T.; Haas, S.; Stassen, A. F.; Batlogg, B. Organic Small Molecule Field-Effect Transistors with Cytop™ Gate Dielectric: Eliminating Gate Bias Stress Effects. *Appl. Phys. Lett.* **2007**, *90*, 092104.
9. Cheng, X.; Caironi, M.; Noh, Y.-Y.; Wang, J.; Newman, C.; Yan, H.; Facchetti, A.; Sirringhaus, H. Air Stable Cross-Linked Cytop Ultrathin Gate Dielectric for High Yield Low-Voltage Top-Gate Organic Field-Effect Transistors. *Chem. Mater.* **2010**, *22*, 1559–1566.
10. Chua, L.-L.; Ho, P. K. H.; Sirringhaus, H.; Friend, R. H. High-Stability Ultrathin Spin-on Benzocyclobutene Gate Dielectric for Polymer Field-Effect Transistors. *Appl. Phys. Lett.* **2004**, *84*, 3400–3402.
11. Jia, X.; Fuentes-Hernandez, C.; Wang, C.-Y.; Park, Y.; Kippelen, B. Stable Organic Thin-Film Transistors. *Sci. Adv.* **2018**, *4*.
12. Furukawa, T. Ferroelectric Properties of Vinylidene Fluoride Copolymers. *Phase Transit.* **1989**, *18*, 143–211.
13. Kepler, R. G.; Anderson, R. A. Ferroelectric Polymers. *Adv. Phys.* **1992**, *41*, 1–57.
14. Naber, R. C. G.; Tanase, C.; Blom, P. W. M.; Gelinck, G. H.; Marsman, A. W.; Touwslager, F. J.; Setayesh, S.; Leeuw, D. M. de. High-Performance Solution-Processed Polymer Ferroelectric Field-Effect Transistors. *Nat. Mater.* **2005**, *4*, 243.
15. Naber, R. C. G.; Asadi, K.; Blom, P. W. M.; de Leeuw, D. M.; de Boer, B. Organic Nonvolatile Memory Devices Based on Ferroelectricity. *Adv. Mater.* **2010**, *22*, 933–945.
16. Li, J.; Sun, Z.; Yan, F. Solution Processable Low-Voltage Organic Thin Film Transistors with High-k Relaxor Ferroelectric Polymer as Gate Insulator. *Adv. Mater.* **2012**, *24*, 88–93.
17. Wang, C.; Lee, W.-Y.; Kong, D.; Pfattner, R.; Schweicher, G.; Nakajima, R.; Lu, C.; Mei, J.; Lee, T. H.; Wu, H.-C.; Lopez, J.; Diao, Y.; Gu, X.; Himmelberger, S.; Niu,

- W.; Matthews, J. R.; He, M.; Salleo, A.; Nishi, Y.; Bao, Z. Significance of the Double-Layer Capacitor Effect in Polar Rubbery Dielectrics and Exceptionally Stable Low-Voltage High Transconductance Organic Transistors. *Sci. Rep.* **2015**, *5*.
18. Kong, D.; Pfattner, R.; Chortos, A.; Lu, C.; Hinckley, A. C.; Wang, C.; Lee, W.-Y.; Chung, J. W.; Bao, Z. Capacitance Characterization of Elastomeric Dielectrics for Applications in Intrinsically Stretchable Thin Film Transistors. *Adv. Funct. Mater.* **2016**, *26*, 4680–4686.
19. Khim, D.; Xu, Y.; Baeg, K.-J.; Kang, M.; Park, W.-T.; Lee, S.-H.; Kim, I.-B.; Kim, J.; Kim, D.-Y.; Liu, C.; Noh, Y. Large Enhancement of Carrier Transport in Solution-Processed Field-Effect Transistors by Fluorinated Dielectric Engineering. *Adv. Mater.* **2016**, *28*, 518–526.
20. Lee, J.; Chung, J. W.; Yoon, G. B.; Lee, M. H.; Kim, D. H.; Park, J.; Lee, J.-K.; Kang, M. S. Influence of Dielectric Layers on Charge Transport through Diketopyrrolopyrrole-Containing Polymer Films: Dielectric Polarizability vs Capacitance. *ACS Appl. Mater. Interfaces* **2016**, *8*, 30344–30350.
21. Adhikari, J. M.; Gadinski, M. R.; Li, Q.; Sun, K. G.; Reyes-Martinez, M. A.; Iagodkine, E.; Briseno, A. L.; Jackson, T. N.; Wang, Q.; Gomez, E. D. Controlling Chain Conformations of High-k Fluoropolymer Dielectrics to Enhance Charge Mobilities in Rubrene Single-Crystal Field-Effect Transistors. *Adv. Mater.* **2016**, *28* (45), 10095–10102.
22. Chen, X.; Han, X.; Shen, Q.-D. PVDF-Based Ferroelectric Polymers in Modern Flexible Electronics. *Adv. Electron. Mater.* **2017**, *3*, 1600460.
23. Pfattner, R.; Foudeh, A. M.; Liong, C.; Bettinson, L.; Hinckley, A. C.; Kong, D.; Bao, Z. On the Working Mechanisms of Solid-State Double-Layer-Dielectric-Based Organic Field-Effect Transistors and Their Implication for Sensors. *Adv. Electron. Mater.* **2018**, *4*, 1700326.
24. Salleo, A.; Chabinyk, M. L.; Yang, M. S.; Street, R. A. Polymer Thin-Film Transistors with Chemically Modified Dielectric Interfaces. *Appl. Phys. Lett.* **2002**, *81* (23), 4383–4385.
25. Sun, X.; Di, C.; Liu, Y. Engineering of the Dielectric–Semiconductor Interface in Organic Field-Effect Transistors. *J. Mater. Chem.* **2010**, *20* (13), 2599–2611.

26. Shao, W.; Dong, H.; Jiang, L.; Hu, W. Morphology Control for High Performance Organic Thin Film Transistors. *Chem. Sci.* **2011**, *2* (4), 590–600.
27. Casalini, S.; Augusto Bortolotti, C.; Leonardi, F.; Biscarini, F. Self-Assembled Monolayers in Organic Electronics. *Chem. Soc. Rev.* **2017**, *46* (1), 40–71.
28. Lee, H. S.; Kim, D. H.; Cho, J. H.; Hwang, M.; Jang, Y.; Cho, K. Effect of the Phase States of Self-Assembled Monolayers on Pentacene Growth and Thin-Film Transistor Characteristics. *Journal of the American Chemical Society* **2008** *130* (32), 10556–10564
29. Wang, M.; Ford, M. J.; Zhou, C.; Seifrid, M.; Nguyen, T.-Q.; Bazan, G. C. Linear Conjugated Polymer Backbones Improve Alignment in Nanogroove-Assisted Organic Field-Effect Transistors. *J. Am. Chem. Soc.* **2017**, *139*, 17624–17631.
30. Wang, M.; Ford, M. J.; Lill, A. T.; Phan, H.; Nguyen, T.-Q.; Bazan, G. C. Hole Mobility and Electron Injection Properties of D-A Conjugated Copolymers with Fluorinated Phenylene Acceptor Units. *Adv. Mater.* **2017**, *29*, 1603830.
31. Jung, Y.; Kline, R. J.; Fischer, D. A.; Lin, E. K.; Heeney, M.; McCulloch, I.; DeLongchamp, D. M. The Effect of Interfacial Roughness on the Thin Film Morphology and Charge Transport of High-Performance Polythiophenes. *Adv. Funct. Mater.* **2008**, *18*, 742–750.
32. Egginger, M.; Bauer, S.; Schwödiauer, R.; Neugebauer, H.; Sariciftci, N. S. Current versus Gate Voltage Hysteresis in Organic Field Effect Transistors. *Monatshefte Für Chem. - Chem. Mon.* **2009**, *140*, 735–750.
33. Naber, R. C. G.; Tanase, C.; Blom, P. W. M.; Gelinck, G. H.; Marsman, A. W.; Touwslager, F. J.; Setayesh, S.; de Leeuw, D. M. High-Performance Solution-Processed Polymer Ferroelectric Field-Effect Transistors. *Nat. Mater.* **2005**, *4*, 243–248.
34. Brondijk, J. J.; Asadi, K.; Blom, P. W. M.; de Leeuw, D. M. Physics of Organic Ferroelectric Field-Effect Transistors. *J. Polym. Sci. Part B Polym. Phys.* **2012**, *50*, 47–54.
35. Martins, P.; Lopes, A. C.; Lanceros-Mendez, S. Electroactive Phases of Poly(Vinylidene Fluoride): Determination, Processing and Applications. *Prog. Polym. Sci.* **2014**, *39*, 683–706.

36. Sawyer, C. B.; Tower, C. H. Rochelle Salt as a Dielectric. *Phys. Rev.* **1930**, *35*, 269–273.
37. Sinha, J. K. Modified Sawyer and Tower Circuit for the Investigation of Ferroelectric Samples. *J. Sci. Instrum.* **1965**, *42*, 696.
38. Hwang, D. K.; Fuentes-Hernandez, C.; Kim, J.; Potscavage, W. J.; Kim, S.-J.; Kippelen, B. Top-Gate Organic Field-Effect Transistors with High Environmental and Operational Stability. *Adv. Mater.* **2011**, *23*, 1293–1298.
39. Neese, B.; Wang, Y.; Chu, B.; Ren, K.; Liu, S.; Zhang, Q. M.; Huang, C.; West, J. Piezoelectric Responses in Poly(Vinylidene Fluoride/Hexafluoropropylene) Copolymers. *Appl. Phys. Lett.* **2007**, *90*, 242917.
40. Choi, H. H.; Cho, K.; Frisbie, C. D.; Sirringhaus, H.; Podzorov, V. Critical Assessment of Charge Mobility Extraction in FETs. *Nat. Mater.* **2017**, *17*, 2.
41. Bao, Z.; Locklin, J. *Organic Field-Effect Transistors*; CRC Press, 2007.
42. Seng Chang, S.; B. Rodríguez, A.; M. Higgins, A.; Liu, C.; Geoghegan, M.; Sirringhaus, H.; Cousin, F.; M. Dalgleish, R.; Deng, Y. Control of Roughness at Interfaces and the Impact on Charge Mobility in All- Polymer Field-Effect Transistors. *Soft Matter* **2008**, *4*, 2220–2224.
43. Veres, J.; Ogier, S. d.; Leeming, S. w.; Cupertino, D. c.; Mohialdin Khaffaf, S. Low-k Insulators as the Choice of Dielectrics in Organic Field-Effect Transistors. *Adv. Funct. Mater.* **2003**, *13*, 199–204.
44. Richards, T.; Bird, M.; Sirringhaus, H. A Quantitative Analytical Model for Static Dipolar Disorder Broadening of the Density of States at Organic Heterointerfaces. *J. Chem. Phys.* **2008**, *128*, 234905.
45. Bäessler, H. Charge Transport in Disordered Organic Photoconductors a Monte Carlo Simulation Study. *Phys. Status Solidi B* **1993**, *175*, 15–56.
46. Hulea, I. N.; Fratini, S.; Xie, H.; Mulder, C. L.; Iossad, N. N.; Rastelli, G.; Ciuchi, S.; Morpurgo, A. F. Tunable Fröhlich Polarons in Organic Single-Crystal Transistors. *Nat. Mater.* **2006**, *5*, 982–986.
47. Owens, D. K.; Wendt, R. C. Estimation of the Surface Free Energy of Polymers. *J. Appl. Polym. Sci.* **1969**, *13*, 1741–1747.

48. Kaelble, D. H. Dispersion-Polar Surface Tension Properties of Organic Solids. *J. Adhes.* **1970**, *2*, 66–81.

## **Chapter 6:**

### **Charge Transport Studies of Non-Fullerene Acceptors and High-mobility Semi-conducting Polymers in Organic Field-Effect Transistors**

#### **6.1 Introduction and Motivation**

Non-fullerene acceptors (NFAs) have recently become an area of interest to researchers aiming to develop high performance organic solar cells due to their promising electronic properties and greater tunability relative to fullerene-based acceptors. Such tunability has allowed synthetic chemists to design non-fullerene acceptors with absorption in a desired wavelength region. Spectral regions that are complementary to those of the donor can increase the power conversion efficiency. Designing non-fullerene acceptors with a narrow band gap allows for sensitivity in the infrared region and enables the fabrication of highly sensitive photodetectors.<sup>1-3</sup> Despite the success of NFAs in organic solar cells, there have only been a few studies looking at the electron mobility of these materials.<sup>4-6</sup>

#### **6.2 Non-Fullerene Acceptor N-Type Organic Field-Effect Transistors**

A collection of 12 NFAs with a variety of core groups and sidechain configurations were tested as the active layer in an organic field-effect transistor (OFET) to measure the mobility of horizontal charge transport. Bottom-gate/top-contact OFETs were fabricated using heavily doped silicon as the gate electrode and thermally evaporated silver as the source and drain contacts. 200 nm thick silicon dioxide with a 15 nm thick spin-coated layer of benzocyclobutene (BCB). The purpose of the BCB layer is to reduce electron charge trapping

that is known to occur at the semiconductor – SiO<sub>2</sub> interface.<sup>7</sup> By measuring the transfer characteristics of each NFA material, we are able to perform a systematic structure-property relationship study.

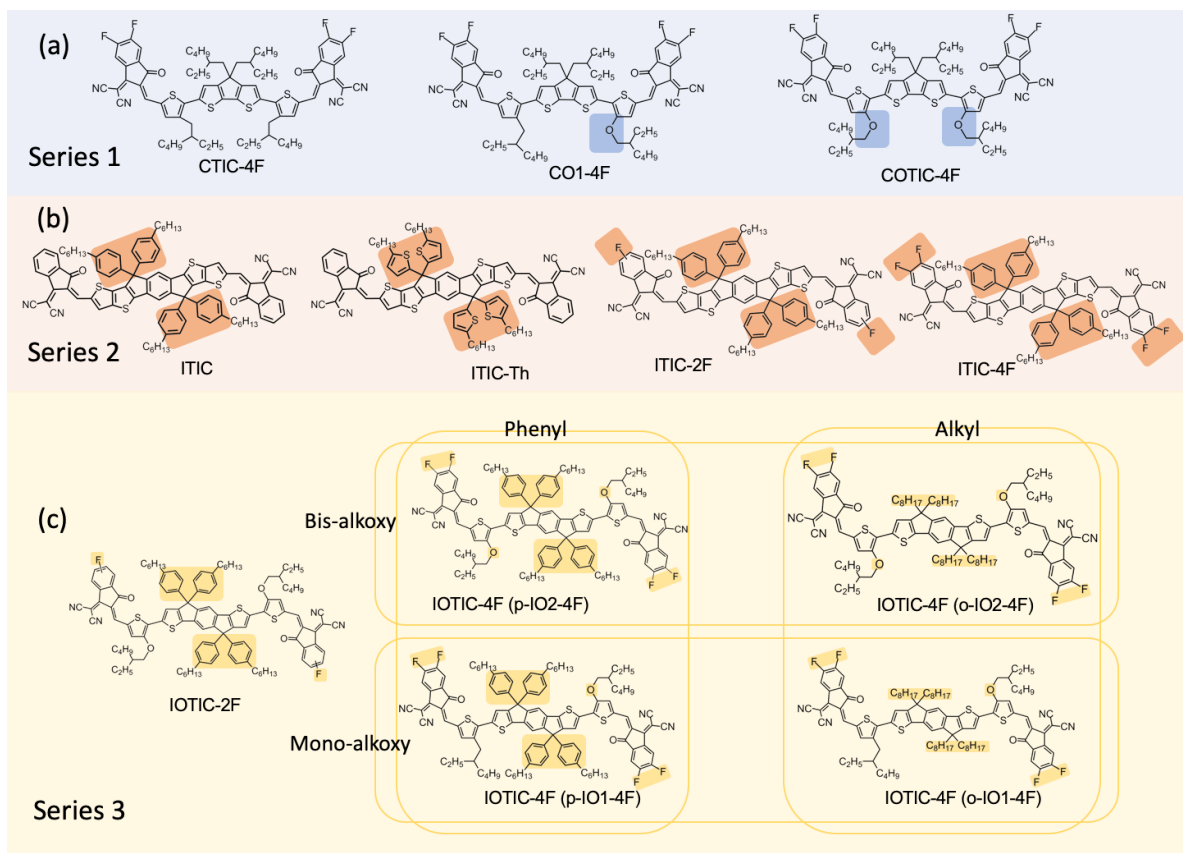


**Figure 6.1:** Summary of the chemical structures of each NFA that was used for this study.

The NFAs that were studied can be split up into 3 groups, based on their core structures (**Figure 6.1a**). The first series of NFAs consists of an electron-rich cyclopentadithiophene (CPDT) internal core flanked with alkoxythienyl units. CTIC-4F, CO1-4F and COTIC-4F differentiate from one another by the varying side chains, which are either alkylthiophene or alkoxythiophene groups. Lee *et al* report a narrowing of the optical band-gap as the number of

alkoxy side chains is increased due to the differences in the electron-donating strengths of the side-chains.<sup>7</sup> The second series consists of ITIC, ITIC-Th, ITIC-2F and ITIC-4F, which all contain a central indacenodithieno[3,2-b]thiophene (IDTT) unit (Figure 1b).<sup>8,9</sup> The structures vary by the sidechain attached to the central IDTT being either a 4-hexylphenyl or 4-hexylthiophene unit and by the number of fluorine atoms attached to the 2-(3-oxo-2,3-dihydroinden-1-ylidene)malononitrile (IC) end groups. A narrowing of the HOMO-LUMO gap is observed as the number of electron-withdrawing fluorine atoms are increased on the IC end groups. ITIC-Th has the largest HOMO-LUMO gap according to cyclic voltammetry (CV) measurements. The third and final series of NFA materials consists of IOTIC-2F, p-IO2-4F, p-IO1-4F, o-IO2-4F and o-IO1-4F. The core unit consists of indaceno[1,2-b:5,6-b']dithiophene (IDT) and 2-(3-oxo-2,3-dihydroinden-1-ylidene)malononitrile (IC) end groups (Figure 1c). The structures vary by the number of fluorine atoms on the IC end groups and the presence of either an alkylthiophene or an alkoxythiophene donor unit.

The mobility measured from OFETs made from each non-fullerene acceptor material is summarized in **Figure 6.2** and **Table 6.1**.

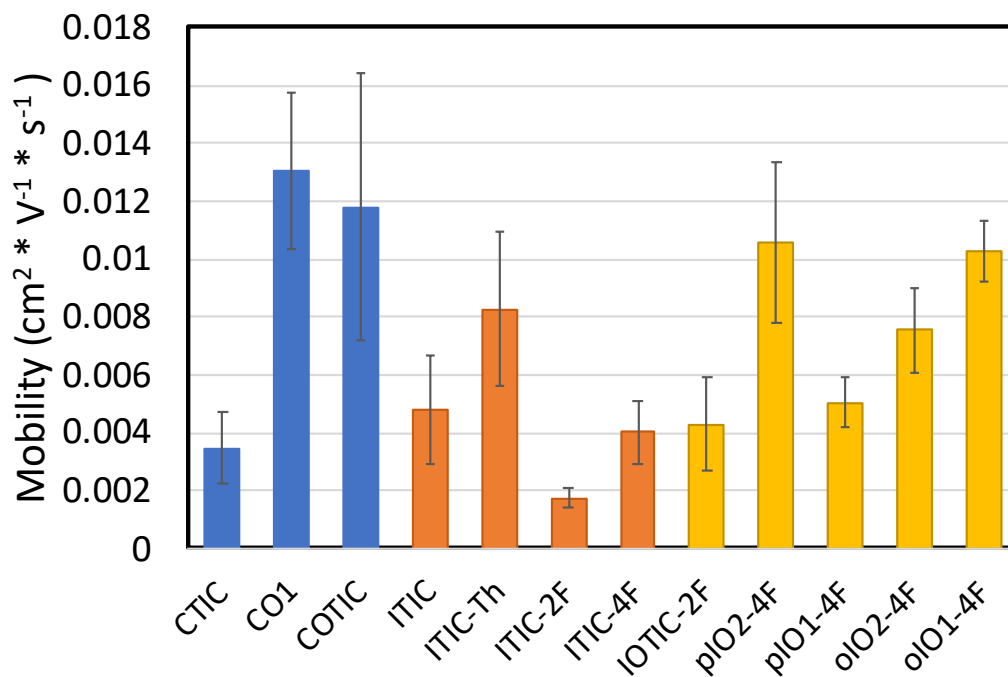


**Figure 6.2:** Summary of the mobility measured from OFETs made with each non-fullerene acceptor material.

**Table 6.1**

	Average (cm <sup>2</sup> * V <sup>-1</sup> * s <sup>-1</sup> )	Standard Deviation (cm <sup>2</sup> * V <sup>-1</sup> * s <sup>-1</sup> )
CTIC-4F	3.46 * 10 <sup>-3</sup>	1.23 * 10 <sup>-3</sup>
CO1-4F	1.30 * 10 <sup>-2</sup>	2.67 * 10 <sup>-3</sup>
COTIC-4F	1.18 * 10 <sup>-2</sup>	4.62 * 10 <sup>-3</sup>
ITIC	4.78 * 10 <sup>-3</sup>	1.86 * 10 <sup>-3</sup>
ITIC-Th	8.28 * 10 <sup>-3</sup>	2.68 * 10 <sup>-3</sup>
ITIC-2F	1.74 * 10 <sup>-3</sup>	3.23 * 10 <sup>-4</sup>
ITIC-4F	4.04 * 10 <sup>-3</sup>	1.08 * 10 <sup>-3</sup>
IOTIC-2F	4.30 * 10 <sup>-3</sup>	1.60 * 10 <sup>-3</sup>
pIO2-4F	1.06 * 10 <sup>-2</sup>	2.77 * 10 <sup>-3</sup>
pIO1-4F	5.05 * 10 <sup>-3</sup>	8.82 * 10 <sup>-4</sup>
oIO2-4F	7.56 * 10 <sup>-3</sup>	1.46 * 10 <sup>-3</sup>
oIO1-4F	1.03 * 10 <sup>-2</sup>	1.05 * 10 <sup>-3</sup>

The first thing that we would like to highlight is the narrow range of mobility between all 12 NFA materials. The range between the lowest material, ITIC-2F, and high mobility material, CO1, only ranges from  $1.74 * 10^{-3}$  and  $1.3 * 10^{-3} \text{ cm}^2\text{V}^{-1}\text{s}^{-1}$ . This is a range of only about 1 order of magnitude. Even though there is a wide range of structures that have been tested, there is a surprising amount of consistency in the mobility measured.

Not much can simply be seen by looking at the mobility of each material, since no clear trends emerge. For each OFET device, various annealing temperatures were tested to see if the device performance can be further optimized. In general, the best device performances were still observed under “as cast” or low temperatures. Annealing temperatures were increased in 20 °C increments from 60 to 180 °C. **Figure 6.3** shows the annealing temperature optimization of the first series of NFA materials, consisting of CTIC-4F, CO1-4F and COTIC-4F. Very minor increases in mobility, if any, are observed when annealing at lower temperatures and a decrease is observed for all materials beyond 100°C.

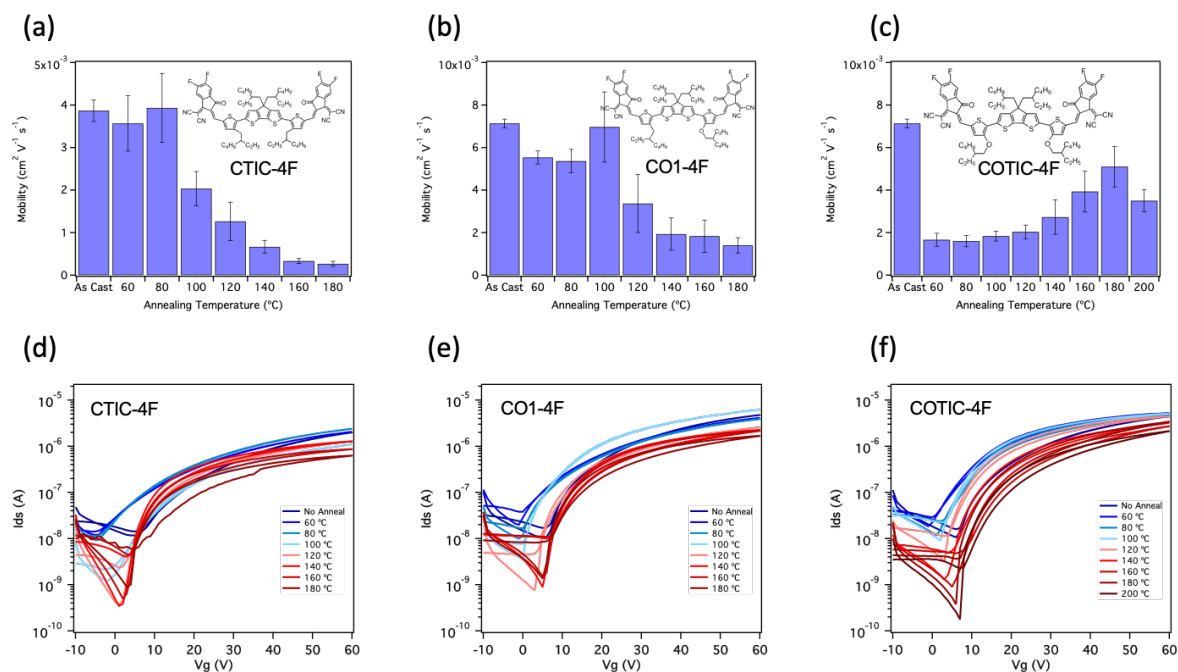


**Figure 6.3:** Mobility after various annealing temperatures of (a) CTIC-4F (b) CO1-4F (c) COTIC-4F and transfer curves of (d) CTIC-4F (e) CO1-4F (f) COTIC-4F and after annealing at various temperatures.

### 6.3 Temperature Dependent Charge Transport in Polymer Organic Field-Effect

#### Transistors

PhF-2,3, PhF-2,5, and PhF-2,6 were synthesized by Dr. Ming Wang of the Bazan group. The polymers were designed to have high mobility and unipolar transport (**Figure 6.4**). The charge hopping efficiency of the PhF polymer series was determined using temperature dependent mobility studies. Bottom gate – bottom contact devices were fabricated using highly doped n-type silicon, thermally grown  $\text{SiO}_2$  gate dielectric and gold contacts. Unless otherwise stated, substrates were surface treated in a solution of 0.2% decyltrichlorosilane in toluene at  $80^{\circ}\text{C}$  for 30 minutes in a nitrogen atmosphere. Polymers were spin coated at 1500 rpm for 1 minute and annealed at  $200^{\circ}\text{C}$  for 8 minutes. Devices are

loaded into a vacuum chamber with a temperature-controlled sample stage and heated for at least 12 hours at 400 kelvin to drive out moisture. Transfer curves were measured from 300K to 80K in 20K steps. **Figure 6.5a** shows the temperature dependence of transfer curves measured from a device prepared by blade coating PhF 2,6 onto a DTS treated SiO<sub>2</sub> substrate. By plotting mobility versus the inverse temperature, we can determine the activation energy of hopping by fitting the slope to an Arrhenius relationship (**Figure 6.5b**).<sup>10</sup> The dip between 300 and 200K is believed to be caused by residual moisture trapped in the active layer.<sup>10</sup>

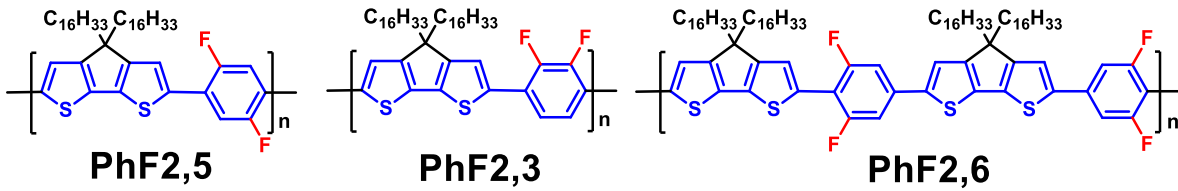


**Figure 6.4.** Chemical structures of PhF polymer series

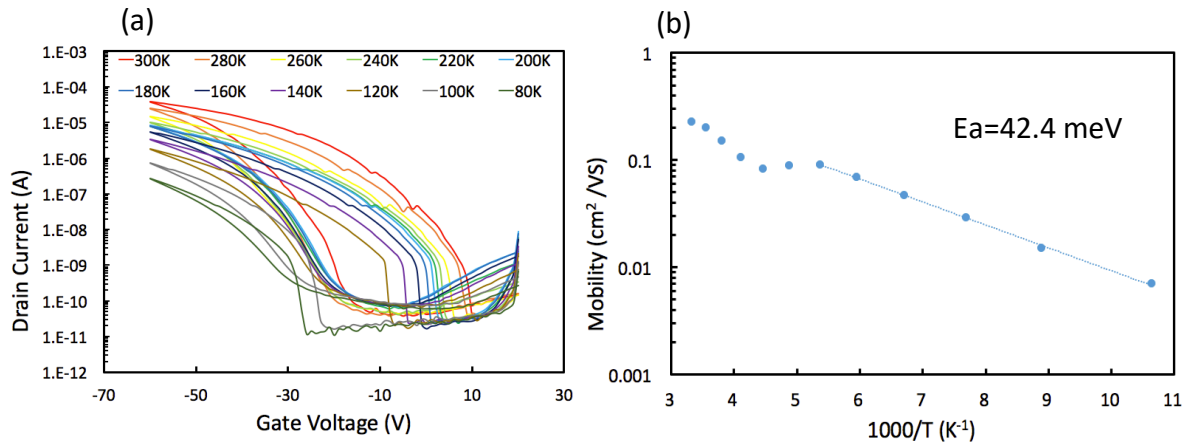


**Figure 6.5:** (a) Transfer curves of a PhF 2,6 device measured at various temperatures ranging from 300 to 80K. (b) By plotting mobility versus inverse temperature, the activation charge hopping in a device can be determined.

The PhF polymers show comparable activation energy values to one another. **Figure 6.6a** summarizes the average activation energy of each PhF polymer and compares them to PCDTPT. At least 15 devices were measured for each data point. There is not a significant difference in the activation energy between the three PhF polymers, however, the activation energy of the PhF polymers is higher than that of PCDTPT. This difference in activation energy could explain the lower mobility observed in PhF polymers when compared to PCDTPT. In **Figure 6.6b**, activation energy is plotted versus the distance of  $\pi$ - $\pi$  stacking. Larger  $\pi$ - $\pi$  stacking distance corresponds to less orbital overlap between neighboring polymers, resulting in a lower efficiency in inter-chain hopping. By reducing the intermolecular distance between polymers in future designs, we can hope to improve mobility, while retaining unipolar transport.

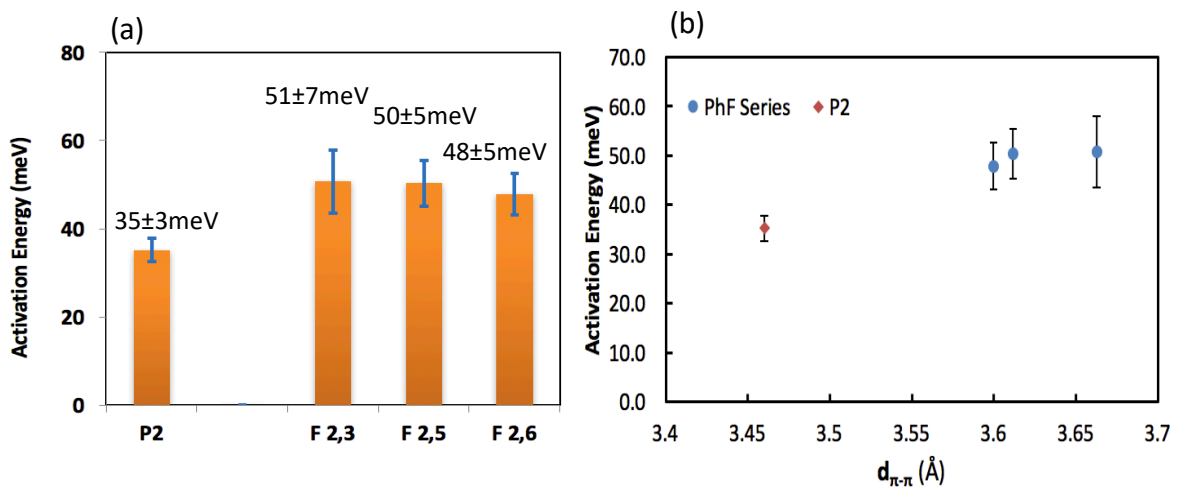


**Figure 6.6:** (a) Average activation energy of each PhF polymer compared to PCDTPT. (b) Activation energy of hopping compared to  $\pi$ - $\pi$  stacking distance determined by GIWAXS

Temperature dependent mobility studies were also performed on PhF polymer aligned on nano-grooved substrates. Devices were prepared by blade coating at 70°C. Results, summarized in **Table 6.2**, show that there is no significant difference in activation energy between devices parallel or perpendicular to the nanogrooves, even though parallel devices have more than an order of magnitude higher mobility. This result was expected, because activation energy relates the energetic barrier of hopping, not the frequency of hopping. An interesting result of plotting the temperature dependent mobility of PhF polymers on nano-grooved substrates, is that the mobility temporarily increases as temperature decreases from 300K to 260K, as shown in **Figure 6.7**. This increase in mobility may be due to the aging effect that occurs when scanning a device multiple times.<sup>9</sup> It should also be noted that there is no dip in the mobility due to moisture, like is often observed in temperature dependent mobility graphs.<sup>8</sup> The increase in mobility between 300K and 260K could also suggest a mixture of band transport and hopping transport in aligned PhF polymers. Electron paramagnetic resonance (EPR) can be used to test for the presence of band transport.<sup>10</sup>

**Table 6.2**

		Mobility (cm <sup>2</sup> /Vs)		Ea (meV)	
Non-grooved Substrate	<b>F2,3</b>	0.17±0.05		50.7±7.2	
	<b>F2,6</b>	0.18±0.05		50.3±5.1	
	<b>F2,5</b>	0.12±0.03		47.8±4.7	
		Parallel μ(cm <sup>2</sup> /Vs)	Perpendicular μ(cm <sup>2</sup> /Vs)	Parallel Ea (meV)	Perpendicular Ea (meV)
Grooved Substrate Cast 70°C	<b>F2,3</b>	0.8±0.1	0.09±0.01	47.9±0.3	50.5±0.4
	<b>F2,6</b>	1.0±0.1	0.09±0.01	43.7±0.8	44.2±0.8
	<b>F2,5</b>	0.4±0.1	0.08±0.01	45.0±1.5	43.7±0.4

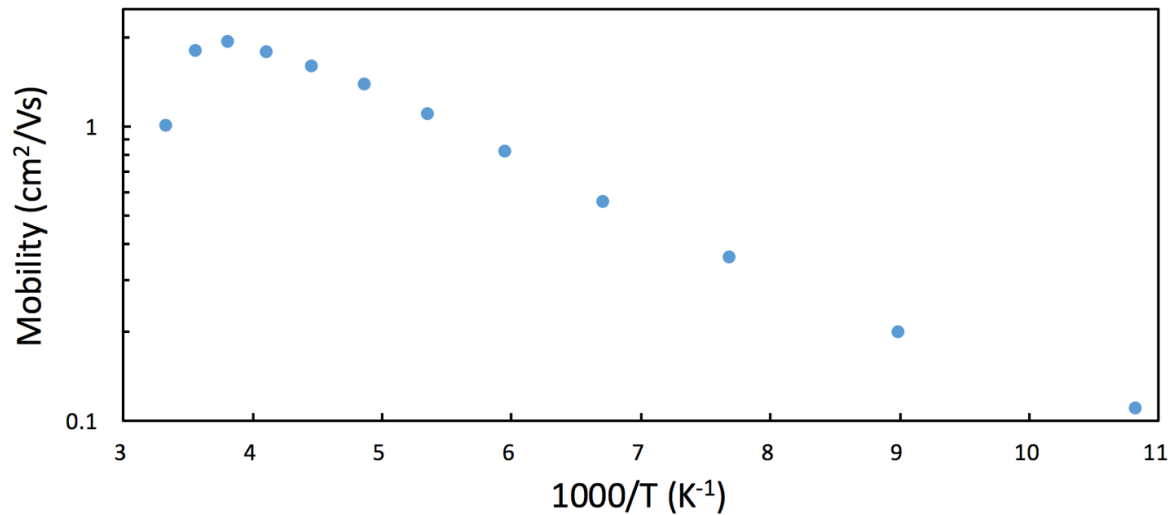


**Figure 6.7:** Mobility as a function of temperature of s PhF-2,6 device prepared on nano-grooved substrate by blade coating at 70°C.

Threshold voltage was plotted as a function of temperature, and it was found to increase in magnitude as temperature decreases (**Figure 6.8**). Threshold voltage varies greatly from device to device at higher temperatures. This result suggests that some of the variation in activation energy observed within the same PhF polymer could be due to the quality of the interface. It has been observed that activation energy can be affected by the density of trap sites at the interface.<sup>8,10</sup> The threshold voltages of all non-grooved PhF polymer devices converge to around -35 to -36 V when devices are cooled down to 80K. Threshold voltage of devices prepared on non-grooved and grooved substrates are summarized in **Table 6.3**.

**Table 6.3**

		$V_T$ (V) (at 300K)		$V_T$ (V) (at 80K)	
Non-grooved Substrate	<b>F2,3</b>	-4.5±8.9		-34.7±1.6	
	<b>F2,6</b>	-12.8±6.3		-35.9±1.4	
	<b>F2,5</b>	-5.0±4.0		-35.9±2.3	
		Parallel $V_T$ (V) (at 300K)	Perpendicular $V_T$ (V) (at 300K)	Parallel $V_T$ (V) (at 80K)	Perpendicular $V_T$ (V) (at 80K)
Grooved Substrate Cast 70°C	<b>F2,3</b>	13.6±4.3	14.2±1.5	-32.3±0.7	-28.5±0.6
	<b>F2,6</b>	11.8±3.7	8.5±3.3	-34.4±0.1	-31.1±0.6
	<b>F2,5</b>	17.1±12.9	5.5±2.9	-34.6±0.1	-30.4±0.5

Future work on temperature dependent mobility studies will focus on studying the effect of molecular weight of semiconducting polymers on activation energy. We also plan on studying the temperature dependence of the mobility of new materials synthesized by the Bazan group.

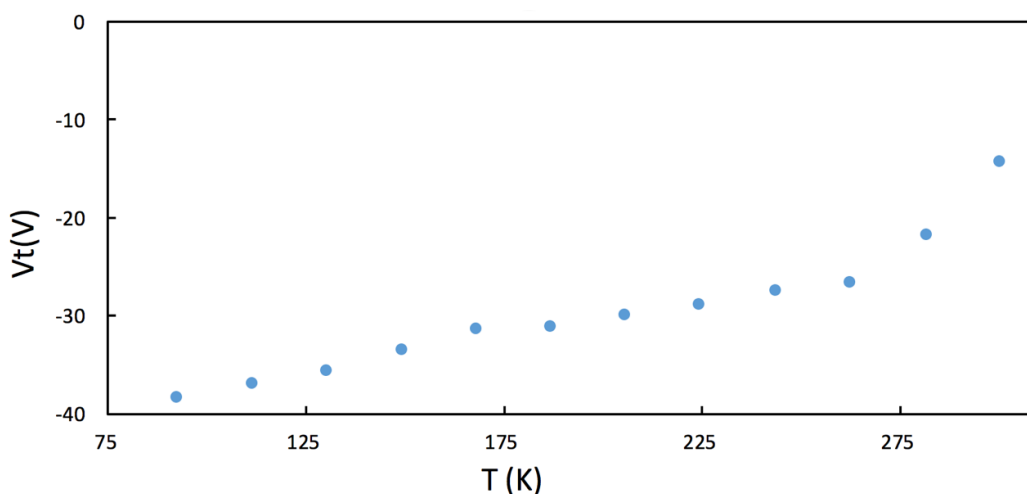


**Figure 6.8:** Threshold voltage as a function of temperature of a PhF-2,6 device blade coated on a non-grooved substrate.

## 6.4 References

1. Lee, J.; Ko, S.-J.; Seifrid, M.; Lee, H.; McDowell, C.; Luginbuhl, B. R.; Karki, A.; Cho, K.; Nguyen, T.-Q.; Bazan, G. C. Design of Nonfullerene Acceptors with Near-Infrared Light Absorption Capabilities. *Advanced Energy Materials* **2018**, *8* (26), 1801209.
2. Lee, J.; Ko, S.-J.; Lee, H.; Huang, J.; Zhu, Z.; Seifrid, M.; Vollbrecht, J.; Brus, V. V.; Karki, A.; Wang, H.; Cho, K.; Nguyen, T.-Q.; Bazan, G. C. Side-Chain Engineering of Nonfullerene Acceptors for Near-Infrared Organic Photodetectors and Photovoltaics. *ACS Energy Lett.* **2019**, *4* (6), 1401–1409.
3. Huang, J.; Lee, J.; Schrock, M.; Dixon, A. L.; Lill, A. T.; Cho, K.; Bazan, G. C.; Nguyen, T.-Q. Large-Gain Low-Voltage and Wideband Organic Photodetectors via Unbalanced Charge Transport. *Mater. Horiz.* **2020**.
4. Park, Y.; Fuentes-Hernandez, C.; Jia, X.; Larrain, F. A.; Zhang, J.; Marder, S. R.; Kippelen, B. Measurements of the Field-Effect Electron Mobility of the Acceptor ITIC. *Organic Electronics* **2018**, *58*, 290–293.
5. Song, X.; Gasparini, N.; Nahid, M. M.; Chen, H.; Macphée, S. M.; Zhang, W.; Norman, V.; Zhu, C.; Bryant, D.; Ade, H.; McCulloch, I.; Baran, D. A Highly Crystalline Fused-Ring n-Type Small Molecule for Non-Fullerene Acceptor Based Organic Solar Cells and Field-Effect Transistors. *Advanced Functional Materials* **2018**, *28* (35), 1802895.
6. Bristow, H.; Thorley, K. J.; White, A. J. P.; Wadsworth, A.; Babics, M.; Hamid, Z.; Zhang, W.; Paterson, A. F.; Kosco, J.; Panidi, J.; Anthopoulos, T. D.; McCulloch, I. Impact of Nonfullerene Acceptor Side Chain Variation on Transistor Mobility. *Advanced Electronic Materials* **2019**, *5* (10), 1900344.
7. Rosenthal, K. D.; Hughes, M. P.; Luginbuhl, B. R.; Ran, N. A.; Karki, A.; Ko, S.-J.; Hu, H.; Wang, M.; Ade, H.; Nguyen, T.-Q. Quantifying and Understanding Voltage Losses Due to Nonradiative Recombination in Bulk Heterojunction Organic Solar Cells with Low Energetic Offsets. *Advanced Energy Materials* **2019**, *9* (27), 1901077.

8. Letizia, J. A.; Rivnay, J.; Facchetti, A.; Ratner, M. A.; Marks, T. J. Variable Temperature Mobility Analysis of N-Channel, p-Channel, and Ambipolar Organic Field-Effect Transistors. *Adv. Funct. Mater.* **2010**, *20* (1), 50–58.
9. Matsui, H.; Mishchenko, A. S.; Hasegawa, T. Distribution of Localized States from Fine Analysis of Electron Spin Resonance Spectra in Organic Transistors. *Phys. Rev. Lett.* **2010**, *104* (5), 056602.
10. Nelson, S. F.; Lin, Y.-Y.; Gundlach, D. J.; Jackson, T. N. Temperature-Independent Transport in High-Mobility Pentacene Transistors. *Applied Physics Letters* **1998**, *72* (15), 1854–1856.

## Chapter 7:

### Summary and Outlook

This thesis discussed a project to explore the structure-property relationship of a group of 12 different n-type non-fullerene acceptor small molecules. Non-fullerene acceptors (NFAs) have recently become an area of interest to researchers aiming to develop high performance organic solar cells due to their promising electronic properties and greater tunability relative to fullerene-based acceptors. Despite the success of NFAs in organic solar cells, there have only been a few studies looking at the electron mobility of these materials. A collection of 12 NFAs with a variety of core groups and sidechain configurations were tested as the active layer in an organic field-effect transistor (OFET) to measure the mobility of horizontal charge transport.

The next topic of this thesis focused on organic field-effect transistors (OFETs). Due to convenience and low leakage current, many OFETs use silicon dioxide as the gate dielectric material. As demonstrated by Dr. Hung Phan, trap sites at the dielectric-semiconductor interface result charge trapping. This charge trapping results in unwanted artifacts such as hysteresis, double-slope nonideality characteristics, and reduction in current when the device is continuously biased. The fluoropolymer P(VDF-HFP) was used as a dielectric material. We found that the device transfer characteristics are heavily dependent on the processing conditions and choosing the proper grade of P(VDF-HFP). We presented the correct choice of processing conditions and material grade results in ideal transfer characteristics such as high on-off ratio, low threshold voltage, low hysteresis and high current stability.

In this thesis, the conjugated polyelectrolyte PCPDTBT-SO<sub>3</sub>-K (CPE-K) was fully characterized and developed to be used at the active layer in organic electrochemical

transistors. Using various spectroscopic and electric characterization techniques, CPE-K was fully characterized so that it could be accurately compared to other OECT materials reported in the literature. The techniques used in this work was used to shed light on the operational mechanism of CPE-based OECTs. In addition, the effective use of interdigitated contacts was used to increase the transconductance of OECT devices.

This thesis expanded on the work of CPE OECTs, by exploring their structure-property-relationship. A series of CPE-Na with increasing alkyl chain distances (2-5 methylene units) were synthesized. The purpose of synthesizing these materials was to explore the effect of varying the distance of the pendant charged sulfonate on the side-chain. CPE-Na is a self-doped polymer, due to the negative charge on the sulfonate stabilizing the positively charged polaron. It was hypothesized that reducing the side-chain length would result in easier doping of the CPE due to the proximity of the sulfonate. To our surprise, the opposite trend was observed. By using a wide range of characterization techniques, the structure-property-relationship between the sidechain length and ease of doping of the CPE backbone was explored.

The results highlight the potential of conjugated polyelectrolytes in OECTs and point towards future designs of CPEs for use in OECTs. A wide range of high mobility D-A conjugated backbones have been discovered by the OFET community, and can be adapted for use in OECTs by utilizing water soluble sidechains such as sulfonate functional groups. Water soluble sidechains are critical for allowing bulk doping of the film and allowing the device to operate as an OECT. CPE-K ranks among the highest performing materials for accumulation mode OECTs and represents a shift away from PEDOT:PSS towards a more widespread use of novel materials in organic electrochemical transistors.